Assessment of Geomechanical Properties along a Well in a SAGD Project

by

Boyang Du

A thesis submitted in partial fulfillment of the requirements for the degree of

Master of Science

in
Geotechnical Engineering

Department of Civil and Environmental Engineering
University of Alberta

Abstract

Geomechanical properties of caprock shale formations for SAGD operations play a critical role in its integrity and must be well characterized. As a component of the development of a SAGD project, numerical simulations are used extensively to understand the uncertainties and forecast the economics of the project. For caprock integrity related studies, it is extremely important to establish accurate geomechanical properties. One of the primary elements in carrying out a geomechanical and hydraulic analysis is establishing the in-situ stress state. The magnitude and potentially even orientation, of the in-situ stress can limit the maximum operating pressure, prevent surface heave and maintain caprock integrity.

This research focusses on the development of geomechanical properties and in situ stress estimates from data collected from a well drilled as part of a SAGD project in NE Alberta. Diagnostic formation injection tests or mini-frac tests were conducted at four different depths and pressure transient analysis techniques were used to determine the consistent closure pressure as estimation of the minimum in-situ principal stress. Additional interpretation techniques were adopted to estimate the maximum horizontal stress. In this research, a numerical modeling history match approach was adopted to estimate the maximum horizontal in situ stress. However, determining the magnitude of the maximum horizontal stress remains uncertain for this wellbore location. Geomechanical behavior of the caprock material from the Clearwater Formation and Wabiskaw Member were determined from limited experimental data through a numerical history matching procedure which provided the constitutive parameters for a strain softening model used in the numerical modeling components of this research. The research also integrated geophysical logs such as image log to estimate the stress orientation and calibrated the oriented caliper log to invert for stress magnitude. Integration of all these data types and analysis methods established a consistent stress gradient for this location in comparison to other regional studies and indicates primarily a strike-slip stress state.

Preface

It is gratefully acknowledged that CNOOC has provided an invaluable dataset to enable this research. The conclusions reached from this independent research, however, are solely those of the author and do not reflect any opinion or agreement by CNOOC regarding these conclusions.

Acknowledgement

I would like to thank my supervisor Dr. Rick Chalaturnyk for his patience guidance, beneficial and professional advices. Also, the support and encouragement from students and staffs from Reservoir Geomechanics Research Group. I am also thankful to all the course instructors for their enlightening instructions.

I would like to thank CNOOC Petroleum North America ULC for providing the extensive data set utilized for this research study. I would also like to acknowledge the financial support provided by the Energi Simulation Industrial Research Consortia in Reservoir Geomechanics.

Lastly, I would like to thank my parents for their financial and emotional support.

Table of Contents

List of Tables

List of figures

1 Introduction

Since the 1940's, oil and gas development has been a leading industry in Alberta. Over the past few decades, unconventional resources such as shale/tight oil and gas and oil sand have been vigorously developed. For oil sands development, approximately 80% of the reserves are buried so deep that they can only be extracted economically using in-situ recovery techniques. The two most common techniques are the steam assisted gravity drainage (SAGD) and cyclic steam stimulation (CSS) processes.

This research study is focused on SAGD, which has become the most common thermal recovery technology for producing heavy oil from oil sands and generally involves drilling a pair of horizontal wells in the reservoir; one to inject high pressure, high temperature steam to heat the bitumen and reduce its viscosity and a second well, typically placed some distance directly beneath the injection well, enable production of steam condensate and bitumen. Higher injection pressure can result in higher temperature and higher bitumen flowing rates. However, excessive injection pressure may over pressurize the steam chamber, causing heave on the ground surface and if sufficiently high such that it exceeds the minimum in-situ principal stress, may damage the caprock allowing injected fluids and bitumen to move out of the reservoir. Therefore, it is crucial to limit the maximum operating injection pressure which is a function of the material properties and in-situ stress state.

A good prediction of caprock integrity requires accurate estimation of the geomechanical properties of the caprock materials and formations. This research allows a combination of experimental tests, geophysical logs from the field and numerical simulation results which enables an insight to not only caprock integrity but also all kinds of well operation.

1.1 Background

The Athabasca oil sands is the largest crude bitumen reservoir in the world, located in the northeast of Alberta, Canada. Long Lake is one of the major Athabasca oil sands projects operated by CNOOC Petroleum North America ULC (Alberta oil sands industry update 2007). Long Lake is located 40 km (25 mile) southeast of Fort McMurray in the Athabasca oil sands region of Alberta (Figure 1). It is an integrated steam-assisted gravity drainage (SAGD) and upgrading operation that was one of the first to produce bitumen from the Wabiskaw-McMurray deposit. In order to estimate the material properties and the in-situ stress state, laboratory and field data of were provided from Well 8-29 located in Long Lake which belongs to the Athabasca oil sands region.

Figure 2 shows the geological stratigraphy of the Long Lake area. The Athabasca oil sands is the largest Cretaceous oil sands deposit in Alberta. The Cretaceous strata consists of the Clearwater Formation (Caprock) and the McMurray Formation (Reservoir). The McMurray Formation is up to 150 m thick, consists of a mixture of sandstones, clay and thin coal beds, lies on top of the Devonian deposits which are layers of shale and limestones (Glass 1997). The Clearwater Formation is an overconsolidated clay shale which can be subdivided into several stratigraphic layers. In a SAGD project, the low permeability nature of Clearwater clay shale makes it an excellent caprock.

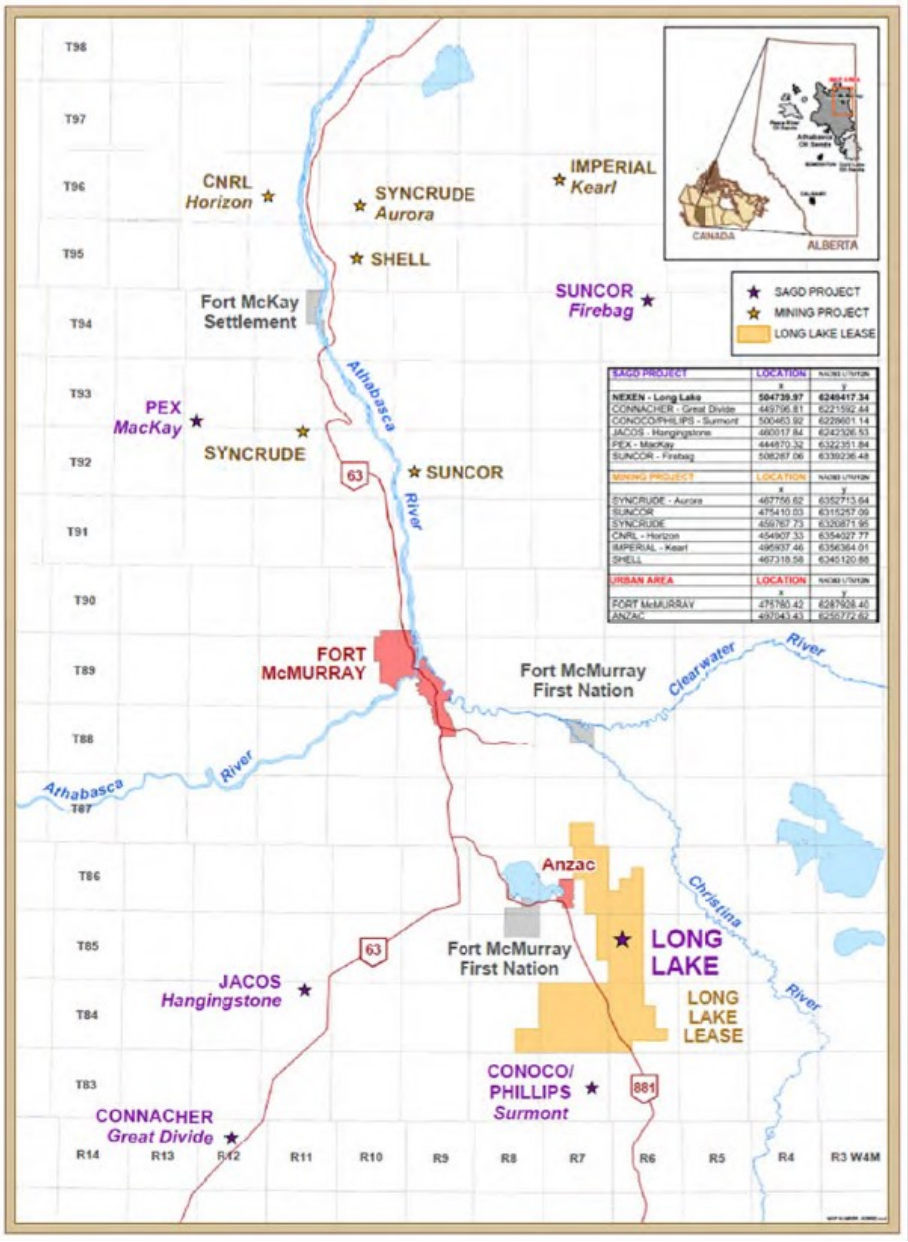

Figure 1. Regional map in Fort McMurray (Nexen 2013)

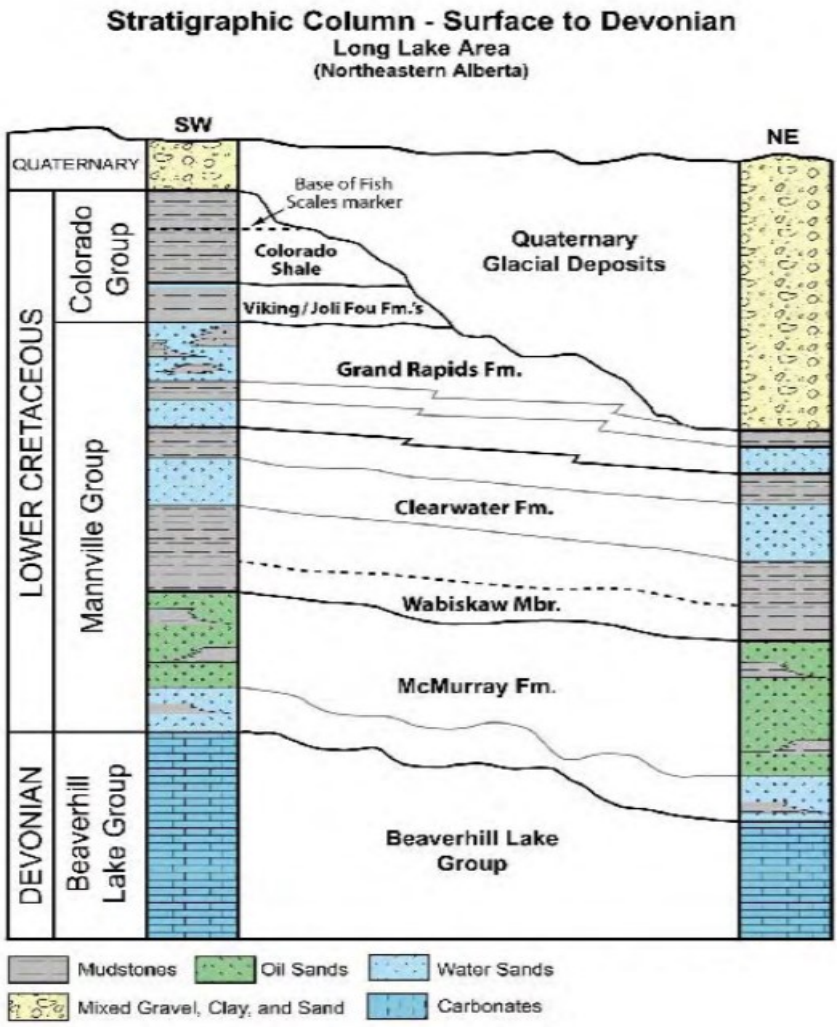

Figure 2. The vertical stratigraphic section of Long Lake (Nexen 2013)

1.2 Objective of Thesis

The objective of this research is to integrate multiple types of data collected in a single borehole within the Long Lake project area to assess the complex constitutive behavior of caprock clay shales and utilize this knowledge to constrain the initial in situ stress state. It is hypothesized that data integration can provide a more solid understanding of the initial stress state than relying solely on estimates generated from mini-frac tests.

1.3 Research Methodology

Caprock integrity for SAGD projects requires a solid understanding of in situ stress state and the constitutive behaviour of formations impacted by SAGD. The thesis will first assess constitutive models for the Clearwater and Wabiskaw Formations generated from laboratory triaxial test data. Then, field test data and geophysical log data were interpreted and calibrated for later simulation. At last, a numerical method was proposed to constrain the in-situ stress state by simulating wellbore deformation by history matching the oriented caliper data. Well AB/08-29 was an observation well drilled to a depth of 259 m in the Long Lake project area near SAGD well pads 14/15, as shown in Figure 3. The well fully penetrates the Clearwater Formation all the way down to the McMurray formation. Well log data are obtained between 40 m to 246 m. Soil samples have been extracted from both Clearwater shale and Wabiskaw member. Laboratory triaxial tests were conducted and the data will be re-analyzed and simulated to generate constitutive models. DFIT, or mini-frac tests were conducted at four depth (151, 171, 207 and 232 m) which cover the whole caprock depth interval and used to estimate the fracture closure pressure. Continuum modeling software FLAC3D were used and codes were generated for geomechanical simulations. General data of this research is summarized in Figure 4.

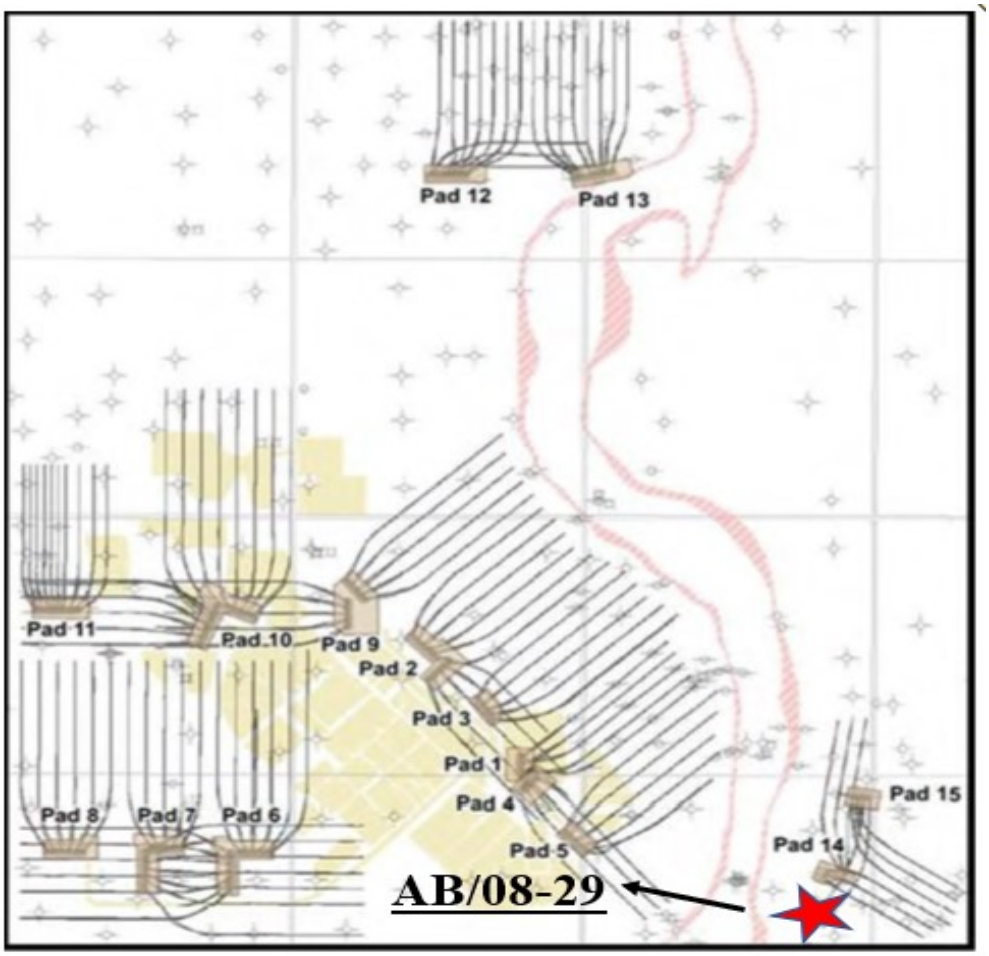

Figure 3. Long Lake well pads (Nexen 2014)

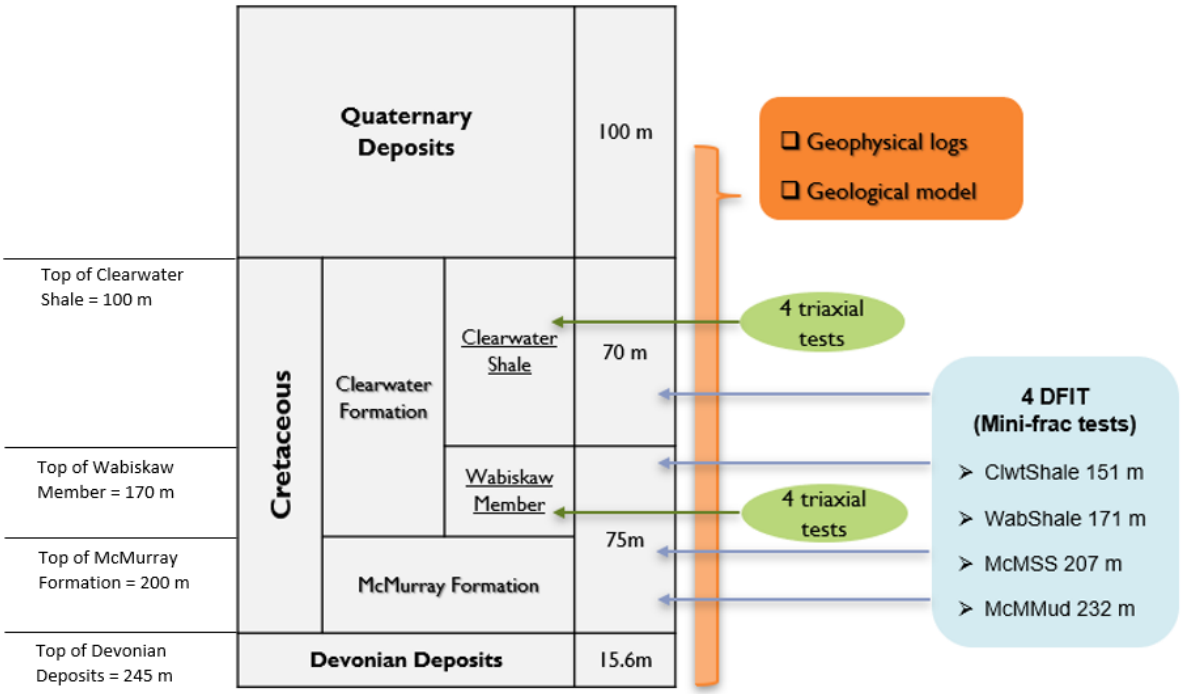

Figure 4. Data provided for this research and the corresponding formation

2 Literature Review

2.1 In-situ Stresses and Techniques of Determination

Stress is a second-rank tensor which has nine components where the elements of main diagonal σ_{11}, σ_{22} and σ_{33} are the normal stresses and the remainder are shear stresses. For convenience, tensor transformation will allow the in-situ stresses acting at a point to be decomposed into three principal stresses; maximum, intermediate and minimum principal stresses. In this way, it is also possible to derive the stress state of stability problems in any arbitrary directions such as around a wellbore, along a fault plane or slip surface.

$$\sigma = \begin{bmatrix} \sigma_{11} & \sigma_{12} & \sigma_{13} \\ \sigma_{21} & \sigma_{22} & \sigma_{23} \\ \sigma_{31} & \sigma_{32} & \sigma_{33} \end{bmatrix} \xrightarrow{\text{Tensor transformation}} \sigma' = \begin{bmatrix} \sigma_1 & 0 & 0 \\ 0 & \sigma_2 & 0 \\ 0 & 0 & \sigma_3 \end{bmatrix}$$

In most geological settings, the vertical stress is assumed to be one of the principal stresses (the overburden stress) and the other two principal stresses are oriented horizontally. The vertical principal stress is referred to as σ_v and the maximum and minimum horizontal principal stresses are referred to as σ_{Hmax} and σ_{hmin}, although they can be equal in magnitude. The vertical stress reflects the overburden weight of the upper materials and the two horizontal stresses are the result of both poroelastic deformations of rocks and tectonic forces, so they are usually anisotropically distributed.

The directions and magnitudes of the in-situ stress are generally related to tectonic activities. To solve reservoir geomechanics problems, understanding the current or initial stress state is critically important. From an engineering perspective, knowledge of the in-situ stress state can help to avoid lost circulation in drilling and identify the propagation azimuth of hydraulic fractures. According to E. M. Anderson's faulting scheme classifications (Anderson 1951), an area can be characterized

by normal, reverse (thrust) or strike-slip faulting depending on the relative magnitude of the principal stresses as shown in Table 1:

Table 1. Relative stress magnitude and faulting regimes

Fault Regime	σ_1	σ_2	σ_3
Normal	σ_v	σ_{Hmax}	σ_{hmin}
Strike-slip	σ_{Hmax}	σ_v	σ_{hmin}
Reverse (Thrust)	σ_{Hmax}	σ_{hmin}	σ_v

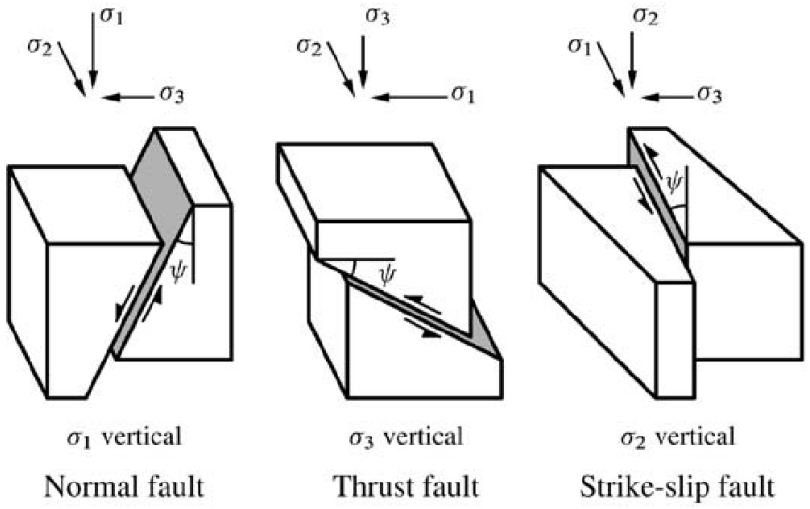

Figure 5. E. M. Anderson's classification scheme for relative stress magnitudes in normal, strike-slip and reverse faulting regions.

The overburden stress or σ_v reflects the overburden weight of the formations above a certain depth and is primarily determined by integrating the density log from ground surface to the depth of interest (Gronseth 1990). Various stress measurement techniques have been developed and summarized by Wang (1997) and Ljunggren et al. (2003):

(1) Anelastic strain relaxation (core expansion upon release from the ground);

(2) Overcoring (based on stress relief around the borehole);

(3) Borehole breakouts (image log and caliper log);

(4) Hydraulic fracturing (Mini-frac and Leak-off test);

(5) Pressuremeter (Cavity expansion);

(6) Acoustic method (Kaiser effect); and

(7) Earthquake focal mechanisms.

This research study utilizes the data from borehole breakouts as an indicator of in-situ stress orientation and diagnostic formation injection tests (DFITs) or mini-frac tests to estimate the magnitude of the minimum component of the in-situ stress tensor.

2.2 Stress Distribution around the Borehole and Wellbore Failures

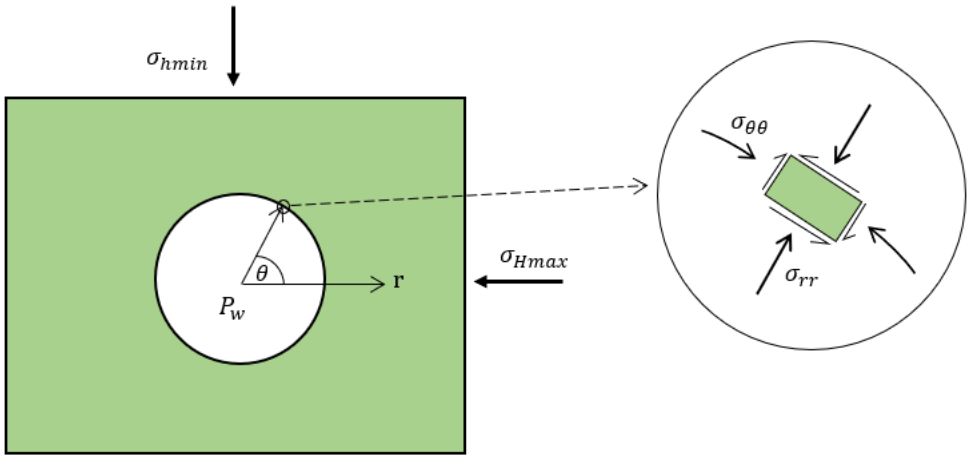

Figure 6. Cylindrical hole in an infinite elastic medium

In the drilling of a borehole, removal of material which provided support will result in stress concentrations around wellbore and leads to elastic and potentially, plastic deformations. These stress concentrations vary with both azimuthal position around the wellbore and the distance from

the wellbore wall. The deformation of the borehole wall in response to these stress concentrations is also a function of the rock strength and the state of stress (Zoback 2007). The stress concentration can lead to wellbore compressive failures known as breakout and tensile failure known as drilling induced fractures. To better understand the compressive failure and tensile failure, Kirsch proposed the following equations (Kirsch, 1898) for stresses around a vertical borehole:

$$\sigma_{rr} = \frac{1}{2}\left(\sigma_{Hmax} + \sigma_{hmin} - 2P_0\right)\left(1 - \frac{R^2}{r^2}\right) + \frac{1}{2}\left(\sigma_{Hmax} - \sigma_{hmin}\right) \times \left(1 - \frac{4R^2}{r^2} + \frac{3R^4}{r^4}\right)\cos 2\theta + \frac{P_w R^2}{r^2} \quad [1]$$

$$\sigma_{\theta\theta} = \frac{1}{2}\left(\sigma_{Hmax} + \sigma_{hmin} - 2P_0\right)\left(1 + \frac{R^2}{r^2}\right) - \frac{1}{2}\left(\sigma_{Hmax} - \sigma_{hmin}\right) \times \left(1 + \frac{3R^4}{r^4}\right)\cos 2\theta - \frac{P_w R^2}{r^2} \quad [2]$$

$$\boldsymbol{\sigma_{zz} = \sigma_v - 2\nu\left(\sigma_{Hmax} - \sigma_{hmin}\right)\frac{R^2}{r^2}\cos 2\theta - P_0} \quad [3]$$

$$\boldsymbol{\tau_{r\theta} = \frac{1}{2}\left(\sigma_{Hmax} - \sigma_{hmin}\right)\left(1 + \frac{2R^2}{r^2} - \frac{3R^4}{r^4}\right)\sin 2\theta} \quad [4]$$

where σ_{rr} is the radial stress; $\sigma_{\theta\theta}$ is the tangential stress; σ_{zz} is the vertical stress; $\tau_{r\theta}$ is the shear stress; P_0 and P_w are the pore pressure and mud pressure, respectively; θ represents the angle measured from direction of σ_{Hmax}; R is the radius of the vertical borehole and r is the distance from the borehole center. To investigate the stress distribution on the borehole wall, making r = R (the borehole radius), the above equations are simplified as:

$$\boldsymbol{\sigma_{rr} = P_w} \quad [5]$$

$$\boldsymbol{\sigma_{\theta\theta} = \sigma_{Hmax} + \sigma_{hmin} - 2\left(\sigma_{Hmax} - \sigma_{hmin}\right)\cos 2\theta - P_w - 2P_0} \quad [6]$$

$$\boldsymbol{\sigma_{zz} = \sigma_v - 2\nu\left(\sigma_{Hmax} - \sigma_{hmin}\right)\cos 2\theta - P_0} \quad [7]$$

$$\boldsymbol{\tau_{r\theta} = 0} \quad [8]$$

The maximum and minimum wellbore stresses around the borehole are:

$$\sigma_{\theta(max)} = 3\sigma_{Hmax} - \sigma_{hmin} - P_w - 2P_0 \qquad at\ \theta = \frac{\pi}{2}, \frac{3\pi}{2} \quad [9]$$

$$\sigma_{z(max)} = \sigma_v + 2v(\sigma_{Hmax} - \sigma_{hmin}) - P_0 \quad at\ \theta = \frac{\pi}{2}, \frac{3\pi}{2} \qquad [10]$$

$$\sigma_{\theta(min)} = 3\sigma_{hmin} - \sigma_{Hmax} - P_w - 2P_0 \quad at\ \theta = 0, \pi \qquad [11]$$

$$\sigma_{z(min)} = \sigma_v + 2v(\sigma_{Hmax} - \sigma_{hmin}) - P_0 \quad at\ \theta = 0, \pi \qquad [12]$$

At $\theta = \frac{\pi}{2}$ and $\frac{3\pi}{2}$, the wellbore has the maximum stress concentration (in the direction of σ_h); at $\theta = 0$ and π, the wellbore has the minimum stress concentration (in the direction of σ_H).

Borehole breakout is a borehole enlargement where soils and rocks fail and spall away from the wellbore wall. The compression failure occurs when the stress defined by above equations exceeds the rock compressive strength. According to Equations 9 to 12, the maximum stress concentration happens at the direction of the minimum horizontal stress (σ_h). Hence, borehole breakouts are always at the azimuth of the minimum horizontal stress (σ_h). Tensile failure or drilling induced fractures (DIFs) can also happen during drilling. At $\theta = 0$ and π, the stress concentration is the minimum. If the mud pressure is high enough, the minimum tangential tress $\sigma_{\theta(min)}$ can become a very small or even negative value. When the negative stress exceeds tensile strength of rock, induced fractures will be created. DIFs are narrow and sharp features oriented along the maximum horizontal stress (σ_H) direction since the stress concentration is the minimum (Tingay, Reinecker, and Müller 2008).

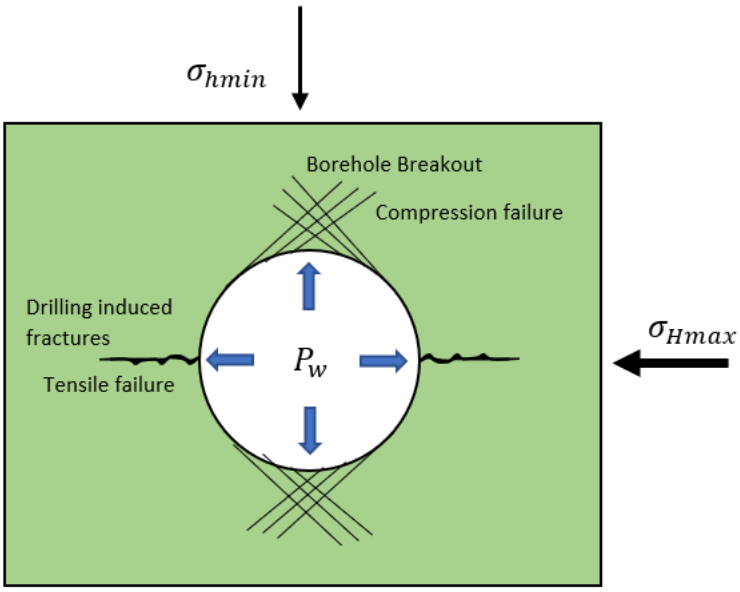

Figure 7. A schematic diagram of wellbore failures

2.3 Interpreting Wellbore Failures (breakouts) from Geophysical logs

Borehole breakouts are considered valuable indicators of in-situ stress orientation. In the World Stress Map, approximately 19% of the stress orientation indicators are determined by borehole breakout (Tingay, Reinecker, and Müller 2008). Borehole breakouts can be interpreted through several types of log data such as image data and caliper data. In this research, six-arm caliper measurements in a vertical well were used to provide the wellbore geometry and diameter data. Therefore, in this section, the interpretation methods of borehole breakouts from image log data and six-arm caliper log data will be introduced.

2.3.1 Interpreting Breakouts from Image log

Borehole imaging was first developed for fracture detection and well remediation in the 1950's (Orleans and Spring 1999). Currently, it has become a common, effective technology in the wireline well logging industry for identifying a variety of geological features and borehole conditions. The accuracy of the image can be as small as in centimeters scale. The devices can be

classified into three groups: 1) Optical imaging; 2) acoustic imaging and 3) electrical imaging, and are described below.

(1) Optical imaging devices are modern technologies that can be operated in both open-hole and cased hole for visual inspection, condition verification and operations (Orleans and Spring 1999). Photographic and television cameras are run downhole to provide a high-resolution color image of the wellbore. One limitation of this device is that the fluid in the well has to be transparent in order to acquire high quality images.

(2) The acoustic imaging tool consists of a rapidly rotating piezoelectric transducer that can operate at ultrasonic frequency in pulse-echo mode. The transducer emits a high frequency sonic pulse travelling through the drilling fluid. Then it hits the wall or casing and bounces back and is received by the transducer. The acoustic imaging tool then records the travel time as well as the amplitude of the return pulse (Tingay, Reinecker, and Müller 2008); Both the travel time and the amplitude are a function of the distance to the wall, or casing, and the velocity of the fluid in the borehole. Finally, the data is processed into images of the borehole wall based on the wall reflectance (return amplitude) and the radius (travel time) (Orleans and Spring 1999).

(3) The electrical imaging tool provides the images of the borehole wall based on electrical resistivity contrasts (Ekstrom 1986). During the measurement, an electric current flow into the formation and then is received by the tool. The current density is related to the formation resistivity and the resistivity in turn is a function of porosity, pore geometry and fluid, cementation and minerology.

In this research, data acquired from a wireline deployed six-arm electrode micro-imaging tool is utilized for examining borehole breakouts in Well 8-29. It has six independent arms, on each arm,

electrode arrays are mounted to measuring the micro-resistivity changes on the borehole wall. Each pad arm has 60 degrees of measurement to cover the whole azimuth. It provides a high-resolution wellbore wall picture based on resistivity contrasts. This resistivity information of the borehole reflects the wellbore geometry, allowing one to observe wellbore breakout directly. Originally, the caliper pad measures the resistivity of the formation while it is rotating and sliding closely against the wall. In the case of breakout, the wellbore enlargement generates gaps between the tool pad and the wellbore wall, as a result, the tool is forced to measure the resistivity of the drilling mud. Because of the high resistivity of the drilling fluid and typical characteristic of breakouts, borehole breakout is identified as broad, parallel, poorly resolved zones located on opposite sides of the borehole (Tingay, Reinecker, and Müller 2008). Figure 8 shows an example of borehole breakout interpreted on a Formation Micro Imager (FMI) log. The breakout is observed on the image as poorly resolved zones roughly oriented towards East and West.

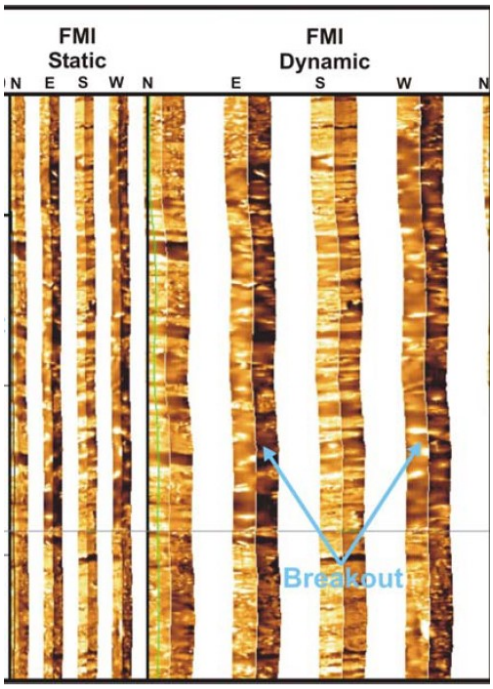

Figure 8. Borehole breakout observed on Formation Micro Imager (FMI) log (Bell, 1996)

2.3.2 Interpreting Breakouts from Caliper log data

In a circular borehole, the caliper tool is rotating (due to the cable torque) and measuring the diameter of the wellbore. When it comes across the enlargement zone, one or several measurement arms (pads) will be trapped in the breakout zone and the tool will stop rotating. In that condition, the extended arms are larger than the wellbore diameter. Based on the criteria for interpreting breakouts from four-arm caliper data, Table 2, as proposed by Plumb and Hickman (1985), Bell (1990), Zajak and Stock (1997) and Reinecker (2003), breakouts are illustrated in an example in Figure 9. Based on the response of arms C1 and C3 (which are in gauge) and C2 and C4 (which are enlarged), Figure 9 shows that breakouts have occurred between the depth of 11,600 and 12,450 feet. This observation is also supported by no changes in the value of pad 1 azimuth, confirming that the tool is not rotating). At a depth near 12,500 feet, where there is no breakout, the tool starts to rotate again, and both sets of arms have the same length equal to the bit size. Note that at a depth of 12,600 feet, the caliper situation is reversed (C1 and C3 are enlarged and C2 and C4 are in gauge) but only as a result of 90° tool rotation - the breakout orientations remain the same over the depth interval illustrated in Figure 9.

Table 2. Criteria for interpreting borehole breakouts from four-arm caliper data

1. Tool rotation must cease in the zone of enlargement.
2. There must be clear tool rotation into and out of the enlargement zone.
3. The smaller caliper reading is close to bit size. Top and bottom of the breakout should be well marked.
4. Caliper difference must exceed bit size by 10%.
5. The enlargement orientation should not coincide with the high side of the borehole in wells deviated by more than 5°.
6. The length of the enlargement zone must be greater than 1 m.

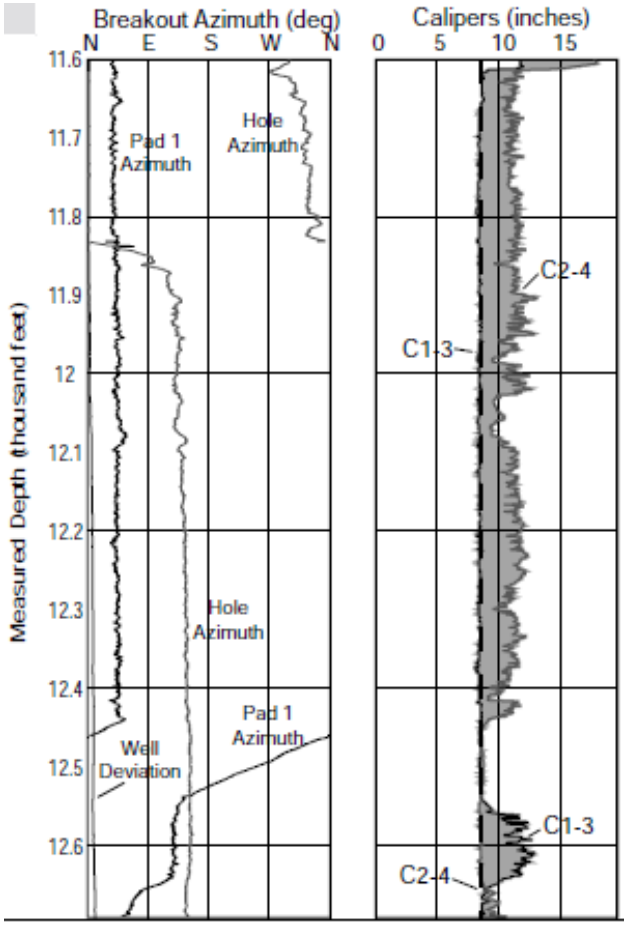

Figure 9. Four-arm caliper log plot displaying borehole breakouts (Zoback 2007)

Similarly, the criteria are also applicable for interpreting the results from six-arm caliper data. While interpreting wellbore breakouts from caliper data seems to be quite straightforward, it is important not to be deceived by washout or key-seats. These two types of wellbore failures both have at least one set of caliper arms larger than the diameter of the undamaged well. The differences are: washout is general sloughing of the entire wellbore in which all the six arms are larger than the diameter of the drill bit; key-seats are a notching of the well that happens only on one side of the wellbore. It is necessary to compare caliper data with wellbore imaging data to distinguish wellbore breakouts.

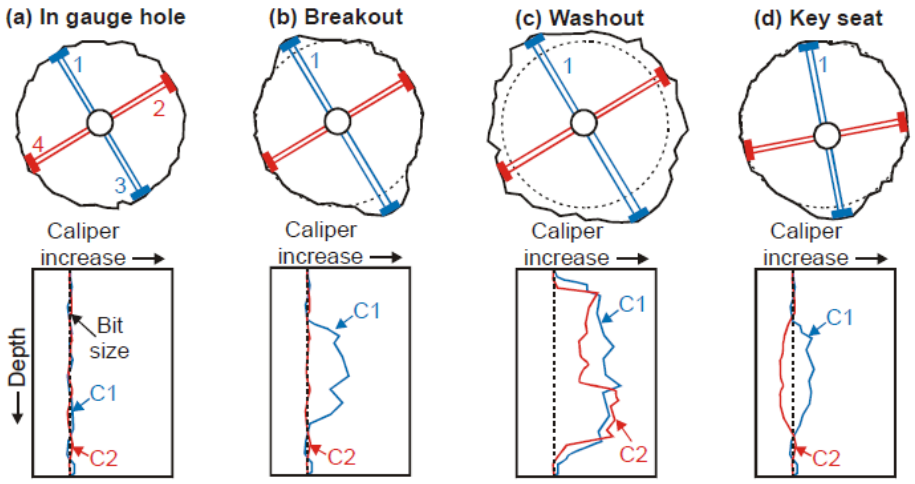

Figure 10. Common types of enlarged borehole and their caliper log response (after Plumb and Hickman, 1985)

2.4 Diagnostic Fracture Injection Test and Interpretation Methods

Optimizing the maximum steam injection pressure in the SAGD process requires knowledge of the in situ stress tensor to ensure that the injection pressure does not exceed the strength of the caprock. A diagnostic fracture injection test (DFIT) or mini-frac test is the most common method for estimating the minimum principal stress, which in many cases is the minimum horizontal stress. DFITs are short duration well tests where a small volume of fluid is injected into the formation until fracture initiation. During the pressure fall-off, pressure data is analyzed to obtain formation properties. Figure 11 illustrates a typical injection and fall-off curve of the mini-frac test. At first, the pressure increases linearly as long as the pumping rate is constant. After a certain point, the pressure increase departs from the linear trend. This point is referred as the leak-off point (LOP), where a hydraulic fracture will have formed. The peak point is regarded as the formation breakdown pressure (FBP) and after that the pressure drops. The reason is that the pumping fluid is "leaking" off from the unstable fracture to the formation faster than the pump can supply fluid. If the pumping continues at a constant rate, the pressure will drop to a stable value called the

fracture propagation pressure (FPP). When the pump is quickly stopped, the fluids stop flowing and the resulting pressure is termed the instantaneous shut-in pressure (ISIP). A good measurement of the least principal stress is to find the fracture closure pressure. After shut-in, the pressure keeps dropping because of fluid leak off and no additional fluids being added to the fracture. When the fluid pressure in the fracture drops to the extent which is equal to the total stress acting on the fracture surface perpendicular to the fracture, this point is called the fracture closure pressure (FCP) (Zoback 2007).

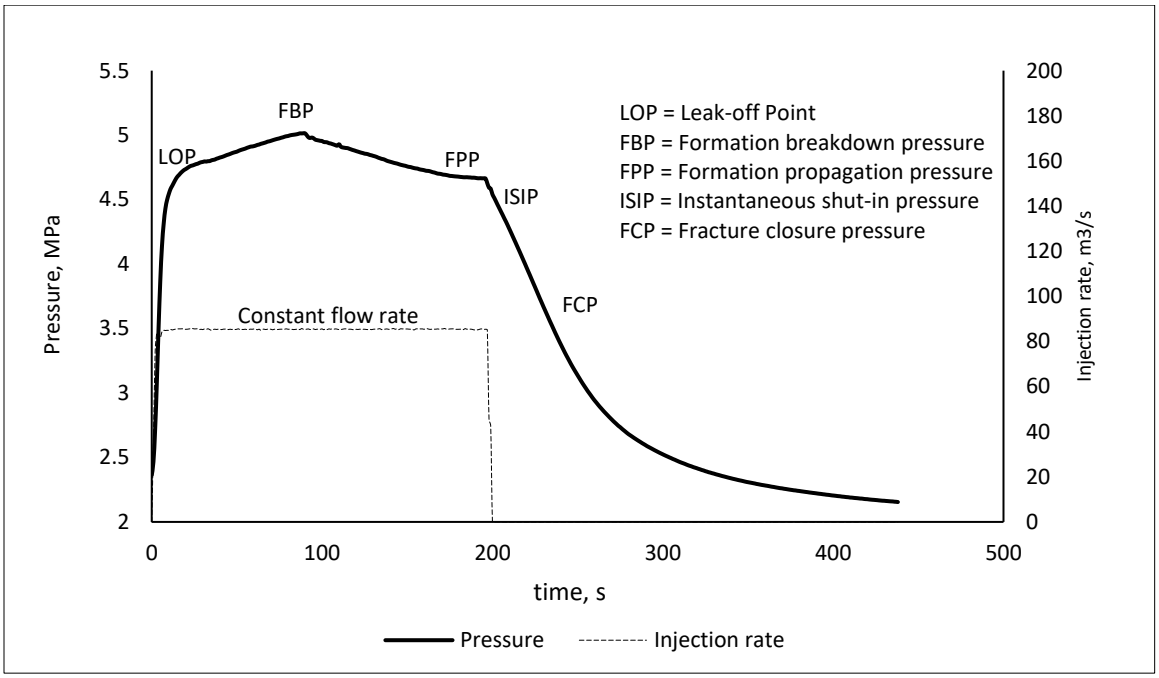

Figure 11. A schematic mini-frac test of pressure as a function of volume injected or equivalently time.

Various methods have been developed to determine the fracture closure pressure in the mini-frac analysis.

(a) G-function method: Nolte (1969) first introduced the G function method for determining closure pressure. G function is a dimensionless time function used to analyze pressure decline behavior during normal fluid leak-off. The G-function is plotted by Pressure versus G time which relating shut in time and total pumping time.

$$G(\Delta t_D) = \frac{4}{\pi}(g(\Delta t_D) - g_0) \quad [13]$$

$$g(\Delta t_D) = \frac{4}{3}\left((1 + \Delta t_D)^{1.5} - \Delta {t_D}^{1.5}\right) \quad [14]$$

$$\Delta t_D = \frac{(t - t_p)}{t_p} \quad [15]$$

where t is time since shut-in and t_p is the pumping time. The assumption behind this technique is the Carter leak-off, which is a one-dimensional leak-off model governed by Carter's equation to describe 1-D fluid filtration from fracture into the formation, coupled with material balance within the fracture. Years later, (Barree, Barree, and Craig 2009) proposed the holistic method that uses G function plots and their derivatives (P vs G, dP/dG vs G and GdP/dG vs G) to predict a more accurate closure event. The closure point can be found by: the pressure curve departs from the straight line; the value of the first derivative curve is no longer constant; the superposition derivative curve deviate from linearity. However, this guidance and hypotheses have been questioned by (Cramer 2015) who suggested a new method especially suitable for low permeability formations. It is assumed that the closing of the fracture can lead to a significance decrease in fracture compliance which in turn results in an increase in pressure derivative dP/dG. In this new fracture compliance method, the closure is picked by the local minimum in dP/dG plot or the increasing change in the slope of GdP/dG curve.

(b) The sqrt(t) plot: In this type of method, the pressure (P) is plotted against the square root of shut-in time. The closure is picked by the departure of the curve from the straight line. However, (Barree, Barree, and Craig 2009) pointed out that the method mentioned above may lead to a later closure event. The correct indication is to find the inflection point on the pressure curve. To do this, the first derivative of P vs sqrt(t) is also plotted and the point of maximum on the derivative curve is the inflection point on the pressure curve. Superposition derivatives are also used (same principle as in the G function method) to avoid incorrect closure picks.

(c) The ΔT derivative (log-log) plot: In the log-log method, the pressure change (ΔP) and derivative (ΔtdΔP/Δt) are plotted against time change since shut-in (Δt). Characteristic slopes on the plot represents different fracture flow regimes. If a slope of the pressure derivative curve 3/2 is presented and followed by a radial flow regime which has a 0 slope, the closure event can be indicated by the depart from the 3/2 trend (Mohamed, 2011).

(d) The Bachman method: Bachman, Walters, and Hawkes (2012) proposed this method by combing the Bourdet log-log derivative plot (which has a different time function than the ΔT log-log plot) with Primary Pressure Derivative plot (PPD). The two plots each has its own independent flow regime identification capabilities (based on the slope). Once the flow regimes have been identified using the two above-mentioned plots, a specialized Bourdet log-log plot can be developed for flow regime verification and closure determination. The closure event can be identified as followed: (1) rapid closure can be determined by any PPD increase or jump; (2) the end of Carter leak-off regime is considered to be a closure event; (3) if Carter leak-off is not present, the end of linear flow

will indicate closure. A detailed description of the methodology and principles followed by various examples can be found in Bachman et al., (2012).

(e) Fracture re-opening test: After the initial pressure build-up and drop-down cycle, during the subsequent fluid injection, the slope of the pressure curve should remain constant until fracture opens. The fracture will be re-opened when the pressure curve deviates from a straight line. The point of departure is chosen as the re-opening pressure and considered to be the upper limit of the minimum in-situ stress (Whitehead, 1989).

(f) Bilinear pressure decay rate method: Additional fracture extension and fracturing fluid leak-off are the causes of pressure decay. As the pressure decreases, it will finally reach a value equal to the stress acting on the fracture surface normal to the fracture. The pressure changes per unit time (dp/dt) plotted against pressure (P) results in a bi-linear curve. The first stage represents linear flow within the fracture and the second stage representing radial flow indicating fracture closure. The intersection of the two lines is considered to be the closure pressure, namely, the minimum in-situ stress (Haimson and Lee, 1989).

(g) Horner plot: the Horner plot is created by plotting pressure (p) vs log scale of (Tinj+t)/t (Horner 1951). The assumption of this method is that the pressure drops are controlled by radial flow after the fracture has completely closed. During fracture closing, the pressure curve deviates from a straight line and the final radial flow is observed as another straight line with different slope on the Horner plot. The transition between the two straight lines represents the onset of closure (Zadeh 2016). The closure pressure can be extrapolated from the radial flow straight line Barree et al, (2009).

3 Development of Constitutive Parameters for Clearwater and Wabiskaw Shale Lithologies

Generally, the Clearwater Formation and its lowermost unit, the Wabiskaw member are considered as caprocks for SAGD projects. For numerical modeling studies of caprock integrity, it is important to determine their geomechanical properties in order to develop appropriate constitutive models for their behavior. In this research, the results from consolidated drained triaxial compression tests were available for both Clearwater and Wabiskaw shales for the determination of parameters for constitutive models. Even with high quality laboratory data, uncertainty will remain in the results due to variability between samples. Consequently, to generalize the results and establish material parameters that best reflected the range of stress-strain behavior measured in the triaxial tests, numerical simulations were undertaken to "history match" the experimental results. A geomechanical simulator, FLAC3D, was used to calibrate the parameters of a constitutive model through manual, trial-and-error and curve-fitting procedures.

3.1 Triaxial Tests for Clearwater Formation

Table 3 summarizes the properties and characteristics of the tested Clearwater samples. Four consolidated drained triaxial compression tests were performed under confining stresses of 4 MPa, 3 MPa, 2 MPa and 1 MPa. For convenience and simplicity, samples will be named by their confining stress value hereafter. For example, sample C6T23S1 which was tested under a confining pressure of 4 MPa will be named Sample 4.

Table 3. Description of Clearwater Samples

Sample #		Depth (m)	Height (mm)	Diameter (mm)	Density (g/cm^3)	Effective confining (MPa)	Loading strain rate (1/s)	Peak strength (MPa)
C6T23S1	#4	142.92	146.59	67.55	2.13	4	2e-6	6.30
C9T33S1	#3	150.76	151.65	69.62	2.07	3	4e-7	5.34
C9T36S1	#2	152.93	149.66	69.28	2.08	2	4e-7	1.57
C12T47S1	#1	161.35	149.56	69.48	2.08	1	4e-7	3.07

Figure 12. Pictures for sample 1 and 4

3.1.1 Stress Strain Behavior

Figure 13 shows plots of deviator stress versus axial strain obtained from Clearwater tests for Clearwater shales under different confining stresses (4 MPa, 3 MPa, 2 MPa and 1 MPa). A well-defined peak was observed for each test. An anomalously low strength and Young's modulus were observed for Sample 2 and has consequently not been included in the strength calculations. Before the peak, hardening behaviors appeared for all curves after axial strains at about 70% of the peak point. There are also softening behaviors after the peak and followed by residual strengths.

3.1.2 Modulus of Elasticity and Strength Parameters

The concept of tangent modulus of elasticity was used here to determine the Young's modulus E. Young's modulus was computed as the slope of a line drawn from the origin to a point on the stress-strain curve at 70% of the maximum deviator stress, as illustrated in Figure 14. The variation

of E with effective confining stress is illustrated in Figure 15. As expected, Young's modulus increases with increasing effective confining stress. A logarithm trendline equation can describe this variation trend with the highest R^2 shown in Figure 15. No attempt was made to fit this trend through the unconfined compressive strength (UCS) point at zero effective confining stress since the UCS was unavailable.

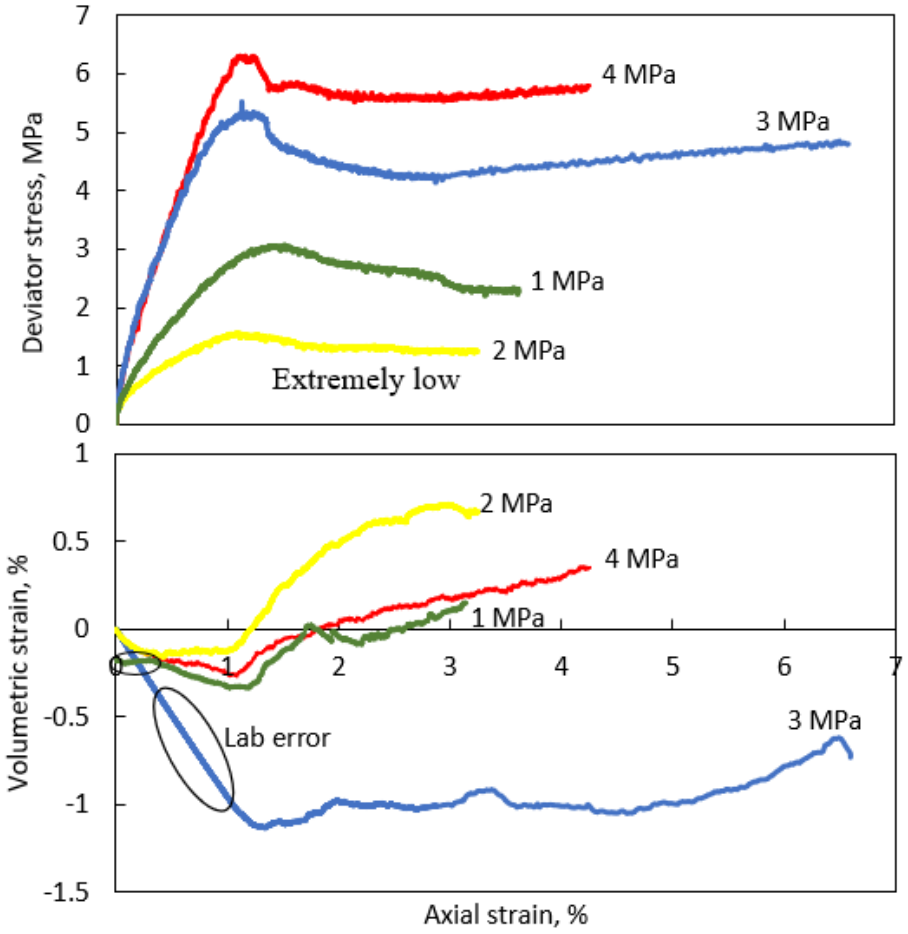

Figure 13. Deviator stress, axial strain and volumetric strain results for Clearwater shale experiments

Consequently, the logarithmic trendline is applicable over the stress range from 1 MPa to 4 MPa. Mohr's circle's at failure are plotted for each test and as shown in Figure 16, it is clear that Sample 2 is displaying anomalous behavior and has been excluded from the interpretation of shear

strength. Based on the results shown in Figure 16, effective cohesion was interpreted as 0.7 MPa and the effective angle of friction is 21˚.

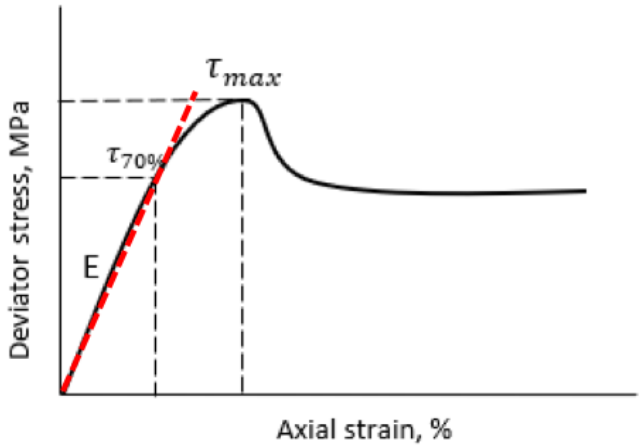

Figure 14. Criteria for calculating Young's modulus, E

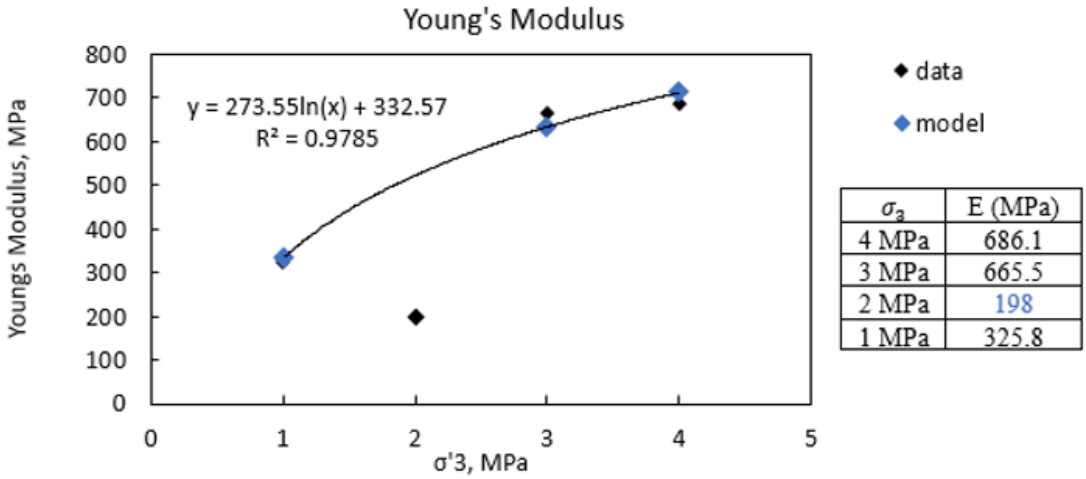

σ_3	E (MPa)
4 MPa	686.1
3 MPa	665.5
2 MPa	198
1 MPa	325.8

Figure 15. Young's modulus vs Confining stresses

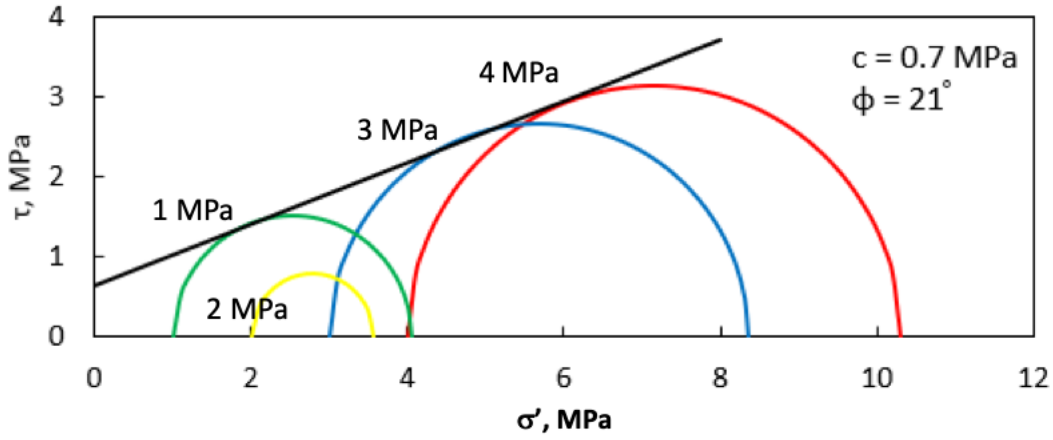

Figure 16. Mohr's Circles for Effective Confining Stresses of 4, 3, 2 and 1 MPa

3.1.3 Volumetric Strain Behavior

Radial strain was measured by circumferential chain-type strain instrument shown in Figure 17. Figure 13 illustrates the volumetric strain behavior of the Clearwater Formation shale specimens. It is postulated that there was a data acquisition error that resulted in the odd volumetric behavior exhibited by Sample 3. Sample 3's stress-strain response was consistent with two other specimens (Sample 1 and 4). In general, all the samples display initial period of contraction followed by a dilation response consistent with the strain softening behavior during shearing. As discussed early, Sample 2 was excluded from the dataset for determining shear strength and for the same reasons, it has been excluded from the volumetric behavior dataset. Consequently, only the behavior of Sample 1 and 4 have been used to estimate Poisson's ratio and dilation angle, which clearly limits the generality of the interpreted behavior.

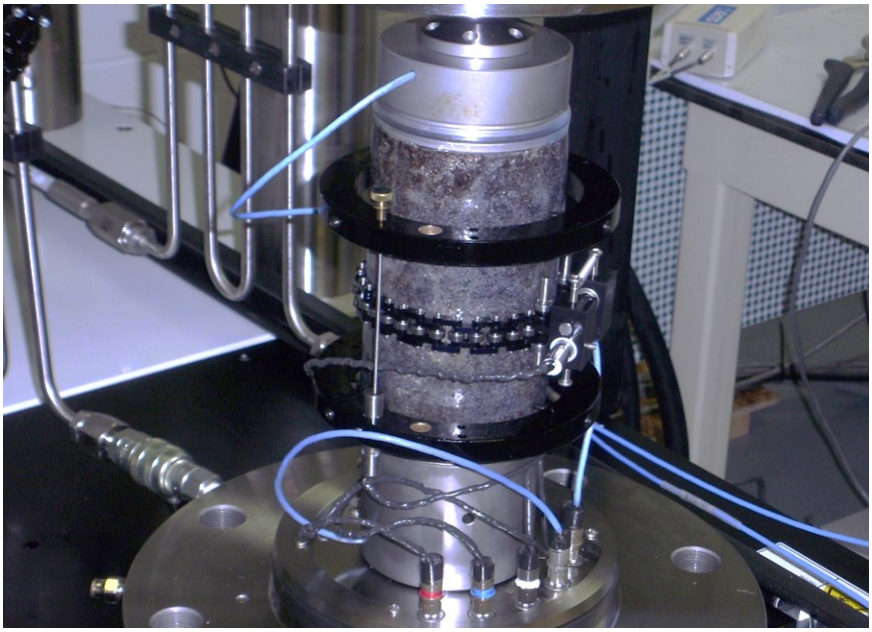

Figure 17. Triaxial test device for Clearwater samples

3.1.4 Simulations of Triaxial Tests for Clearwater Shales

In order to overcome the limitations of the small experimental dataset, a history matching exercise was completed to determine the most suitable constitutive parameters that provided a reasonable overall fit to the data. For stress-strain behavior, three curves (Samples 1, 3 and 4) were chosen to use for simulation and history matching and for volumetric behavior, two curves (Samples 1 and 4) were chosen. The constitutive model chosen to represent the behavior of the Clearwater Formation is a strain hardening/softening model. This model is based on the Mohr-Coulomb shear strength criterion that adopts variations in cohesion, friction angle and dilation angle as a function of plastic yielding, as illustrated in Figure 18. The modeling was carried out through user-defined softening functions (tables) in the numerical simulation software FLAC3D. The parameter e^{ps} represents the plastic shear strain.

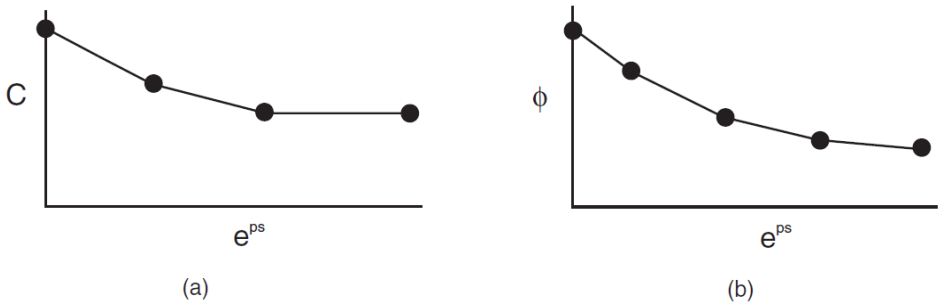

Figure 18. Approximation by linear segments of softening tables (a) cohesion (b) friction angle

Additionally, a nonlinear cohesion weakening friction strengthening (CWFS) model was also employed to capture the variation of shear strength parameters. The CWFS model assumes that as damage accumulates, cohesion degrades and in general an increasing friction angle is mobilized. The CWFS model offers sufficient versatility to be applied to a wide range of geomaterials with strain softening and strain hardening behavior (Rafiei and Martin 2018). Within the model, cohesion is mobilized first from a maximum value and degrading to a residual value and the friction angle increases from an initial value to a maximum value at peak strength and a subsequent reduction to a residual value. The degradation of cohesion and mobilization of friction can be expressed as:

$$\mathrm{c} = c_r + (c_i - c_r)\left[2 - \frac{2}{1+\exp\left(-5\frac{\varepsilon^p}{\varepsilon^p_{c,r}}\right)}\right] \quad [16]$$

$$\phi = \phi_i + (\phi_{max} - \phi_i)\left[\frac{2}{1+\exp\left(-5\frac{\varepsilon^p}{\varepsilon^p_{\phi,max}}\right)} - 1\right] - (\phi_{max} - \phi_r)\left[\frac{1}{1+\exp\left(-5\frac{2\varepsilon^p - \varepsilon^p_{\phi,r} - \varepsilon^p_{\phi,max}}{\varepsilon^p_{\phi,r} - \varepsilon^p_{\phi,max}}\right)}\right] \quad [17]$$

where c_i and c_r are the initial value and residual cohesion; ε^p is the plastic strain; $\varepsilon^p_{c,r}$ is the plastic strain at which cohesion has the residual value; ϕ_i, ϕ_r and ϕ_{max} are the initial, residual and maximum friction angle, respectively; $\varepsilon^p_{\phi,r}$ and $\varepsilon^p_{\phi,max}$ are the plastic strains at which friction angle approaches the maximum and residual value;

The numerical history-matching simulations were conducted based on the following steps:

a. A single cubic element was used in the numerical simulation for simplicity as all the meshes or grids are homogeneous in FLAC3D;
b. The initial conditions (confining stress) and boundary conditions (to match triaxial test) in the model were applied for each lab test;
c. Initial values of Young's modulus, cohesion, friction angle was assumed in the hardening/softening model; and
d. Simulations were run for the same isotropically consolidated triaxial compression stress paths executed in the lab and model parameters were adjusted until a good visual match was obtained.

3.1.5 Results and Conclusions

Figure 19 shows the comparison of stress-strain curves obtained from the simulations and experiments. Although Sample 2 showed anomalously low shear strength, the simulation result for 2 MPa is still shown in Figure 19 for reference. In general, the simulation results match the experimental behavior quite well not only with respect to peak strength but also for pre- and post-peak behavior. Coefficient of determination r^2 was also determined for each curve, which is 0.979, 0.967 and 0.93 for 4 MPa, 3 MPa and 1 MPa. The magnitudes of the initial and calibrated parameters are summarized in Table 4. The variation in cohesion and friction angle with plastic

strain are summarized in Figure 20. Effective cohesion drops from 0.675 MPa to a post-peak value of 0.575 MPa. The effective friction angle has an initial value of 14° which increases to a peak of 21.5°, consistent with value obtained from the M-C criterion and then decreases to 19°at higher plastic strains in the post peak region. Based on this history match data, the parameters for the CWFS model are listed in Table 5.

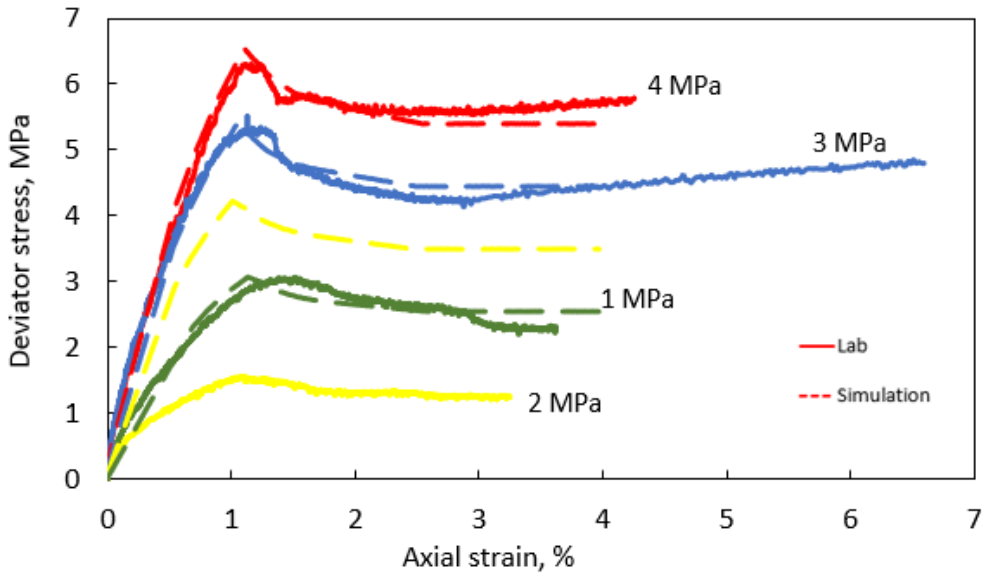

Figure 19. Deviator stress versus axial strain curves and comparison between laboratory results and simulation results

Table 4. Initial and calibrated input modulus parameters

Sample #		Confining stress, MPa	Young's Modulus, MPa		Poisson's ratio	
			Initial	Calibrated	Initial	Calibrated
C6T23S1	#4	4	686	711.8	0.320	0.33
C9T33S1	#3	3	665	633.1	/	
C9T36S1	#2	2	198	522.2	/	
C12T47S1	#1	1	325	332.6	0.327	

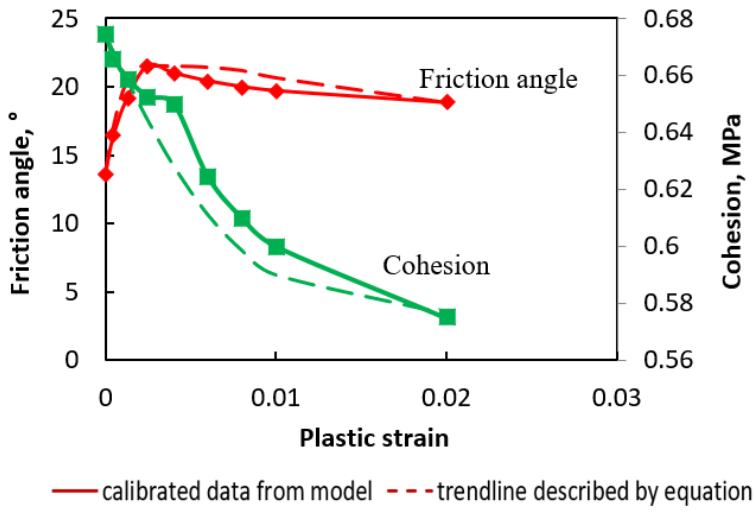

Figure 20. Calibrated strength parameters versus plastic strain

Table 5. Parameters in Cohesion Degradation Friction Mobilization equations

Cohesion (MPa)	c_i	c_r	$\varepsilon_{c,r}^p$		
	0.67	0.57	0.02		
Friction (°)	ϕ_i	ϕ_{max}	ϕ_r	$\varepsilon_{\phi,max}^p$	$\varepsilon_{\phi,r}^p$
	13.6	21.5	18.8	0.0025	0.02

Figure 21. shows comparison between simulation results and laboratory data of volumetric behaviors. The simulation results of sample 4 and sample 1 match perfectly. Poisson's ratio 0.33 can fit the volumetric behavior under shearing. The maximum dilation angle 10 ° occurs immediately after the peak, then it drops to 3.5° as plastic strain increases. In general, the combined constitutive model proposed for this type of soil perfectly match the stress-strain behaviors at different confinement levels. However, less credit is given to the simulation results for volumetric behaviors because the poor quality of data.

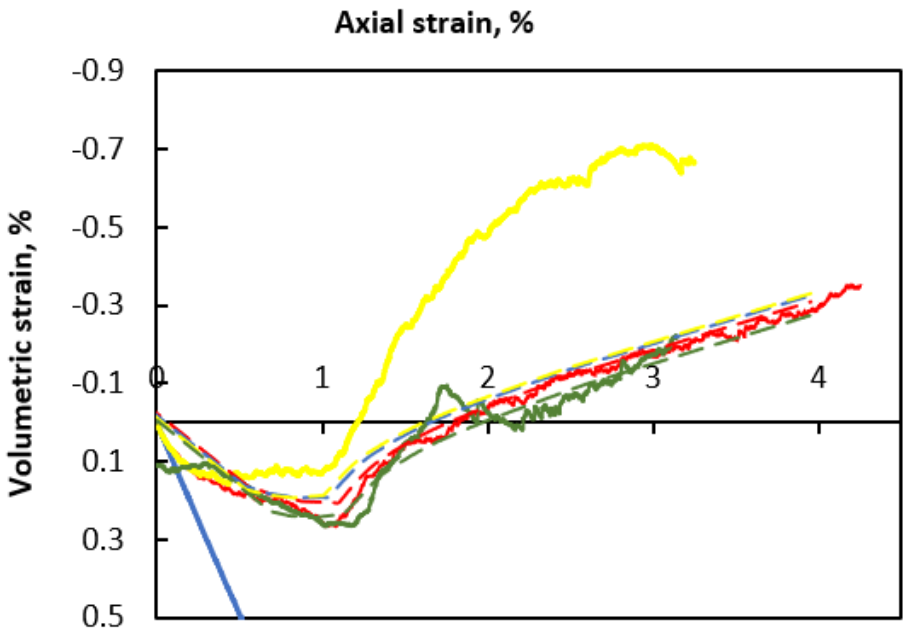

Figure 21. Volumetric strain vs axial strain curves and comparison between laboratory results and simulation results

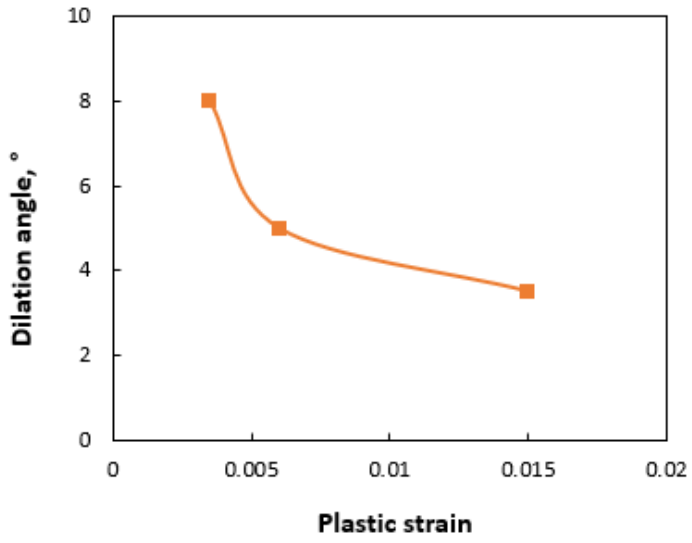

Figure 22. Calibrated dilation angle vs plastic strain

3.2 Triaxial Tests for Wabiskaw Formation

Figure 23 illustrates the pre- and post-test conditions for the specimens. Table 6 summarized the properties of the tested Wabiskaw samples. Four consolidated drained triaxial tests were also

performed under confining stress 1 MPa, 0.5 MPa, 0.2 MPa and 0.1 MPa. Successive load increments are applied once consolidation has ceased. For simplicity, the sample curves are named as sample 1, 2, 3 and 4 respectively hereafter.

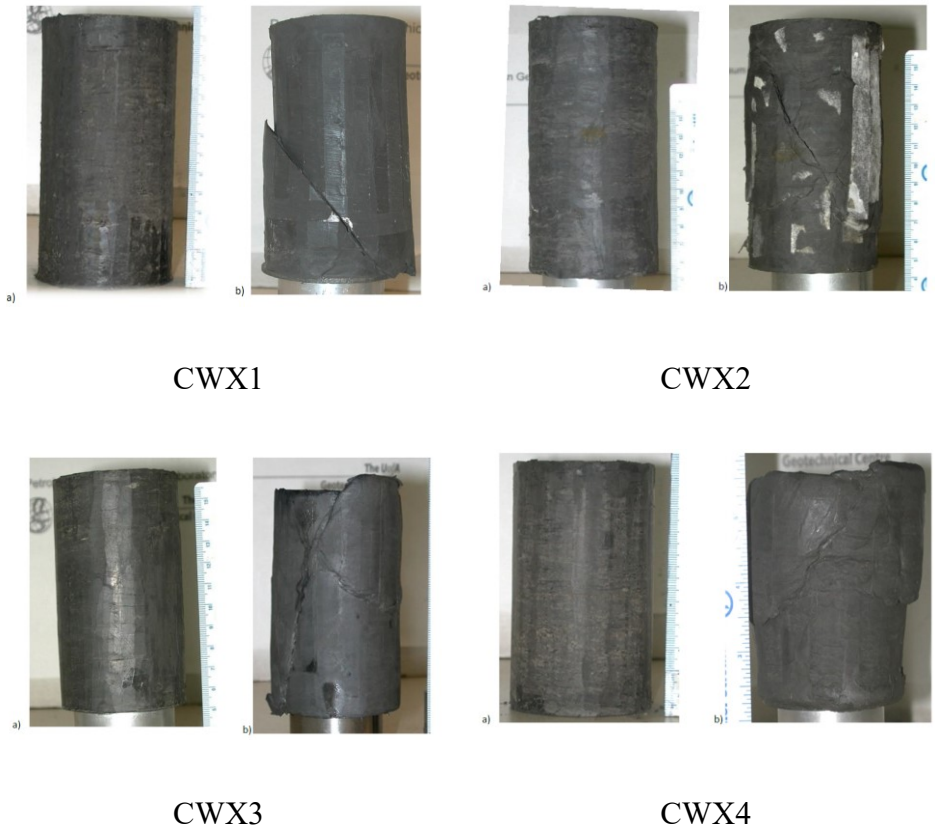

CWX1 CWX2

CWX3 CWX4

Figure 23. Pre- and post-peak conditions for Wabiskaw samples

Table 6. Description of Wabiskaw samples

Sample #		Depth (m)	Height (mm)	Diameter (mm)	Density (g/cm^3)	Void ratio	Effective confining (MPa)	Peak strength (MPa)
CWX1	#1	79.83	139.81	70.52	2.05	0.555	1	4.34
CWX2	#2	80.35	139.93	68.88	2.06	0.513	0.5	2.19
CWX3	#3	79.68	128.08	63.10	2.06	0.544	0.2	1.66
CWX4	#4	80.21	128.82	63.03	2.01	0.550	0.1	0.68

3.2.1 Soil Shear Strength and Parameters

Figure 24 shows plots of deviator stress versus axial strain obtained from tests for the Wabiskaw samples under different confinement levels (1 MPa, 0.5 MPa, 0.2 MPa and 0.1 MPa). The same as Clearwater samples, they also show a moderate hardening behavior before peak and softening behavior after peak. Mohr-Coulomb strength parameters are shown in Figure 25 where c' equals 0.13 MPa and φ' was taken as 33°. Young's modulus of the Wabiskaw samples also show stress-dependent behavior. The Young's modulus is increasing with increasing confining stress and can be captured by the linear equation in Figure 26. A logarithm trendline can also describe this increasing trend with a higher coefficient of determination number. However, an extremely high Young's Modulus would be calculated under high confining stresses. Consequently, a linear trendline was selected to capture the behavior and able to make sure the Young's Modulus lies in a reasonable range.

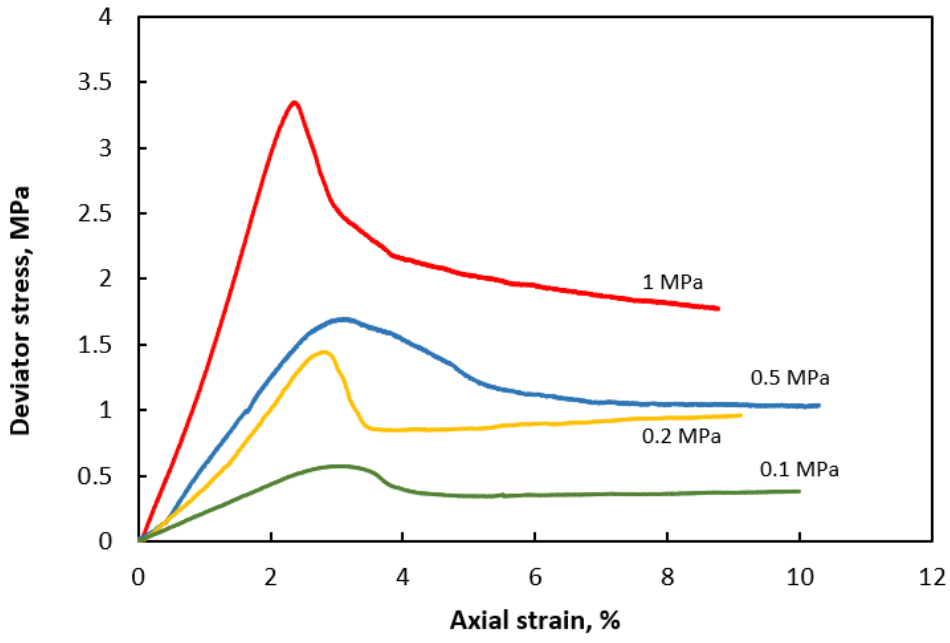

Figure 24. Deviator stress versus axial strain curves for Wabiskaw shale samples

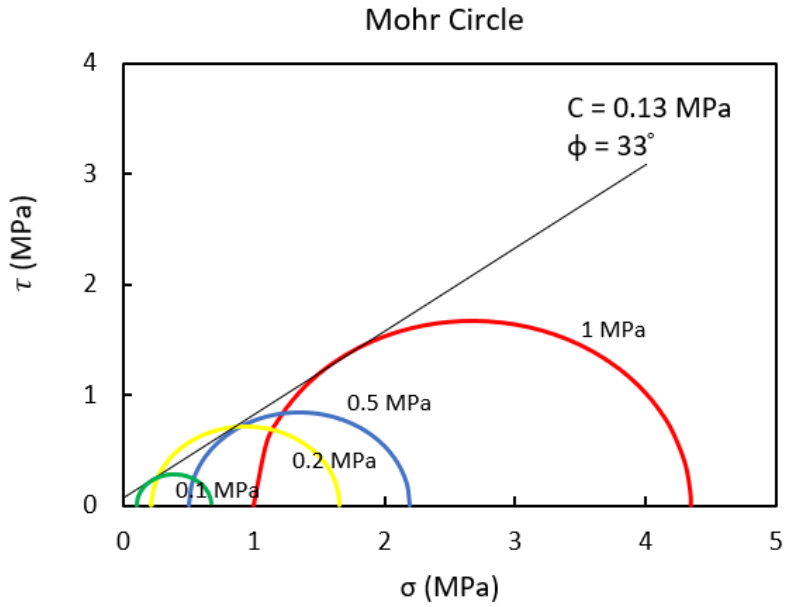

Figure 25. Mohr's Circle for Wabiskaw samples

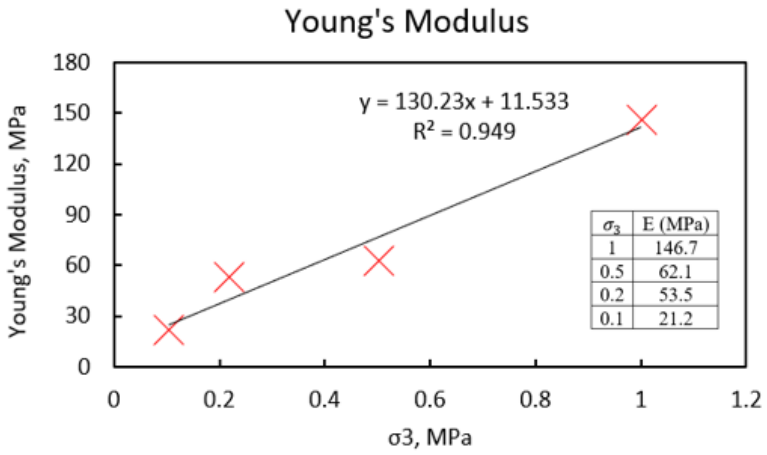

Figure 26. Young's modulus vs confining stress

3.2.2 Volumetric Behavior

Volumetric change is measured by the positive displacement pump used to control the pore pressure, which is set in constant pressure control mode during drained shear. Figure 27 shows the volumetric strain versus axial strain curves for different confining stresses. Before the inflection

point, four curves show good consistency and for axial strains less than 0.5%, can be described by a similar Poisson's ratio of 0.36. At axial strains greater than 0.5%, the specimens begin to experience dilatant volumetric strains. The availability of several reasonably consistent volumetric curves provides data to describe the variability of dilation angles with different confinement levels.

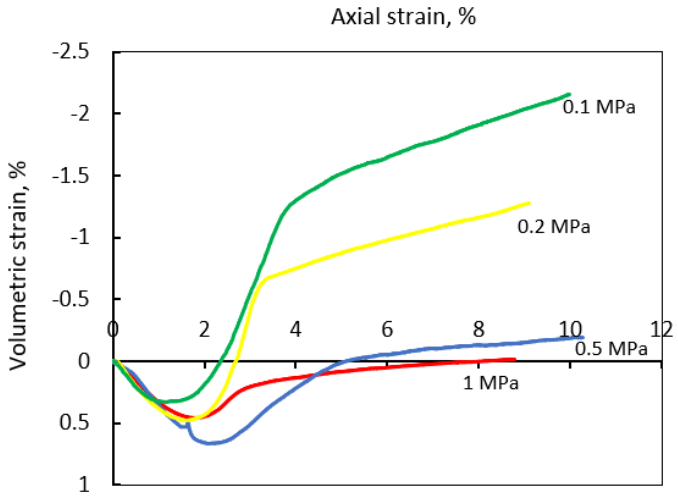

Figure 27. Volumetric strain vs axial strain curves for Wabiskaw samples from experimental tests

3.2.3 Simulation of Triaxial Tests for Wabiskaw Shales

In the simulation of triaxial tests for Wabiskaw samples, the same strain hardening/softening model and CWFS model has been adopted. From these simulations, it was only possible to achieve a consistent match for the tests results from Samples 1 and 4. It is unclear why the other test results did not conform to the model. While it is suspected there is inconsistency in the test results, it is equally plausible that models such as the hardening /softening model may not appropriate for this class of materials. Therefore, the calibration simulation has mainly relied on the results of these two samples. Typical curves of deviator stress versus axial strain are shown in Figure 28. The match between experimental data and simulation results are not as consistent as the results for the Clearwater samples, however the model was able to capture the general range of behavior for the

Wabiskaw samples. The magnitude of the initial and calibrated strength parameters are summarized in Table 7 and Figure 29. The changes of strength parameters are not as smooth as Clearwater samples, but again appears to be suitable in capturing the basic characteristics of the CWFS behavior. Table 8 summarizes the CWFS model parameters for the Wabiskaw Formation.

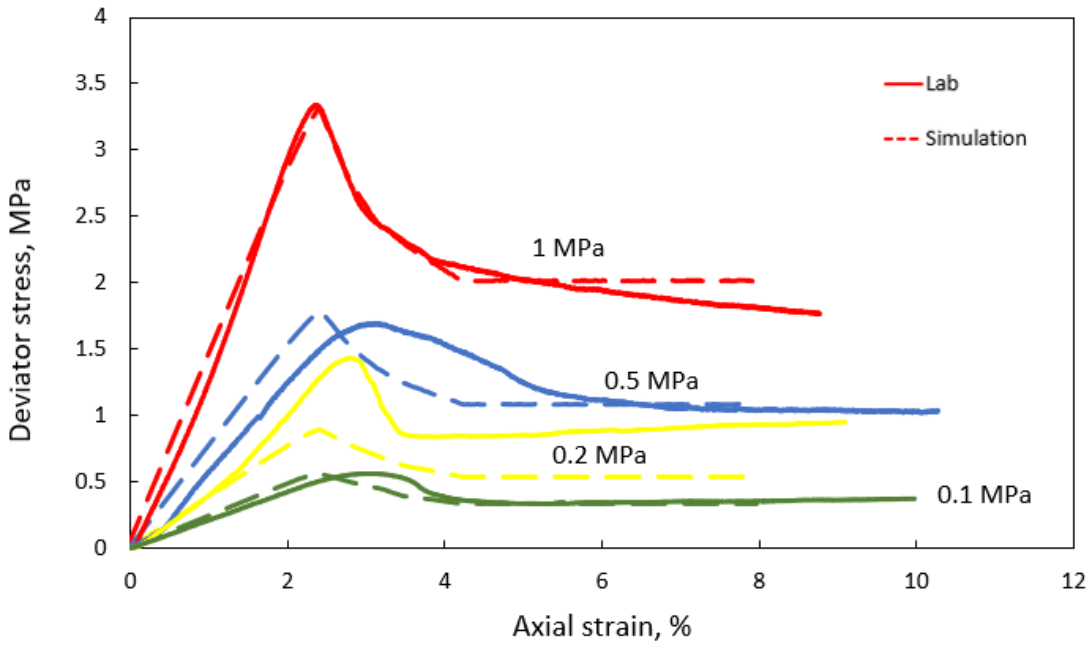

Figure 28. Deviator stress versus axial strain curves and comparison between laboratory results and simulation results

Table 7. Initial and calibrated input modulus parameters

Sample #		Confining stress, MPa	Young's Modulus, MPa		Poisson's ratio	
			Initial	Calibrated	Initial	Calibrated
C6T23S1	#1	1	146.7	141.8	0.35	0.36
C9T33S1	#2	0.5	62.1	76.9	0.33	
C9T36S1	#3	0.2	53.5	40.0	0.34	
C12T47S1	#4	0.1	21.5	25.1	0.32	

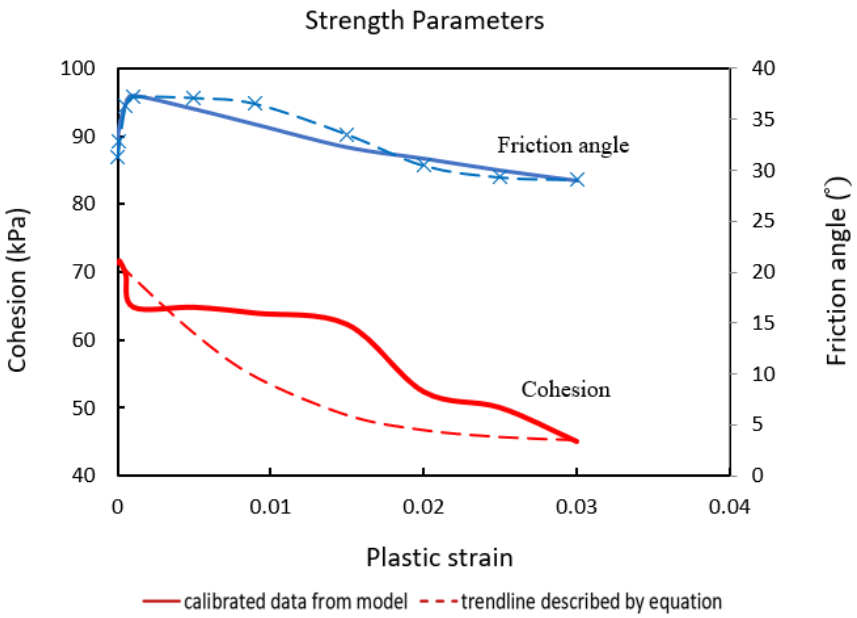

Figure 29. Calibrated strength parameters vs plastic strain

Table 8. Parameters in cohesion weakening friction strengthening (CWFS) equations

Cohesion (kPa)	c_i	c_r	$\varepsilon^p_{c,r}$		
	71.5	45	0.03		
Friction (°)	ϕ_i	ϕ_{max}	ϕ_r	$\varepsilon^p_{\phi,max}$	$\varepsilon^p_{\phi,r}$
	31	37	29	0.001	0.03

Figure 30 shows the comparison of volumetric curves between simulation results and experimental observations. Similar to the Clearwater Formation, Poisson's ratio equal to 0.36 can be used to calibrate the compression behavior of the soil. Beyond axial strains of approximately 2%, the rate of dilatant volume change or dilation angles vary with different confining stresses and decreases with plastic strain. Figure 31 shows the peak dilation angles for each curve. The peak values present right after the inflection point and the changes with confining stress can be captured by the equation in Figure 31. Figure 32 illustrates the variation in dilation angle as a function of plastic shear strain.

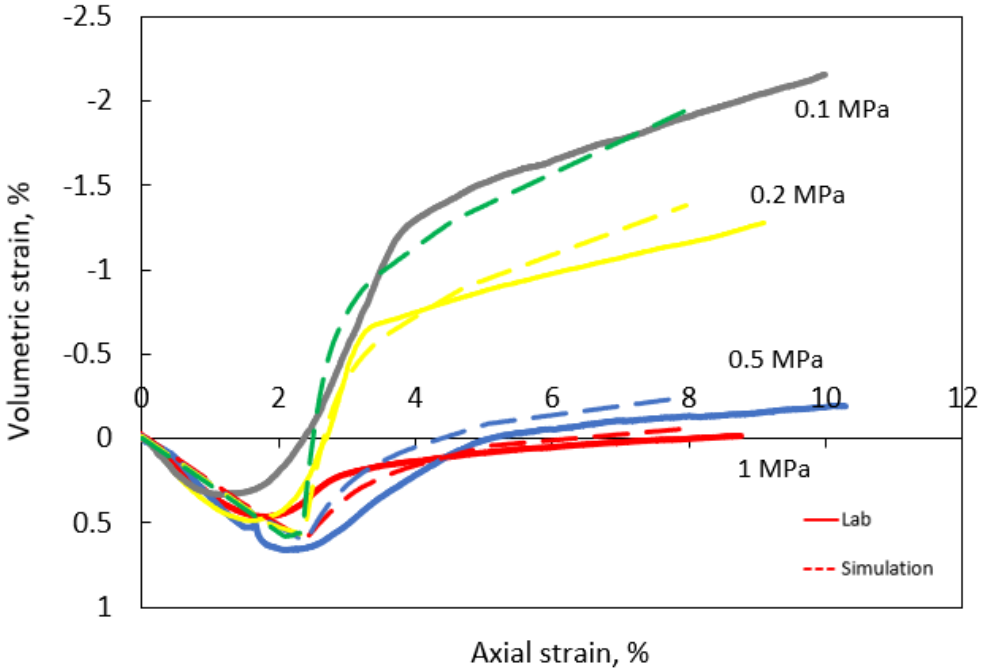

Figure 30. Volumetric strain vs axial strain curves and comparison between laboratory results and simulation results

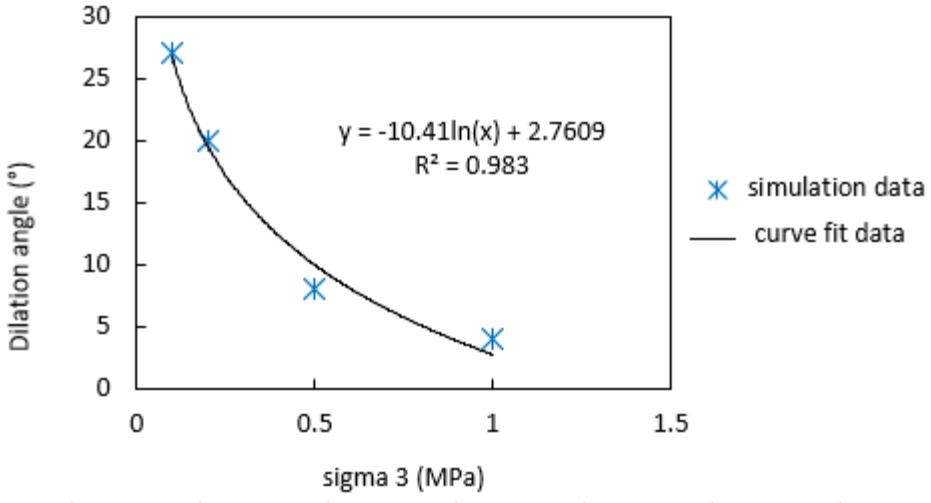

Figure 31. Relationship between peak dilation angle and confining stress

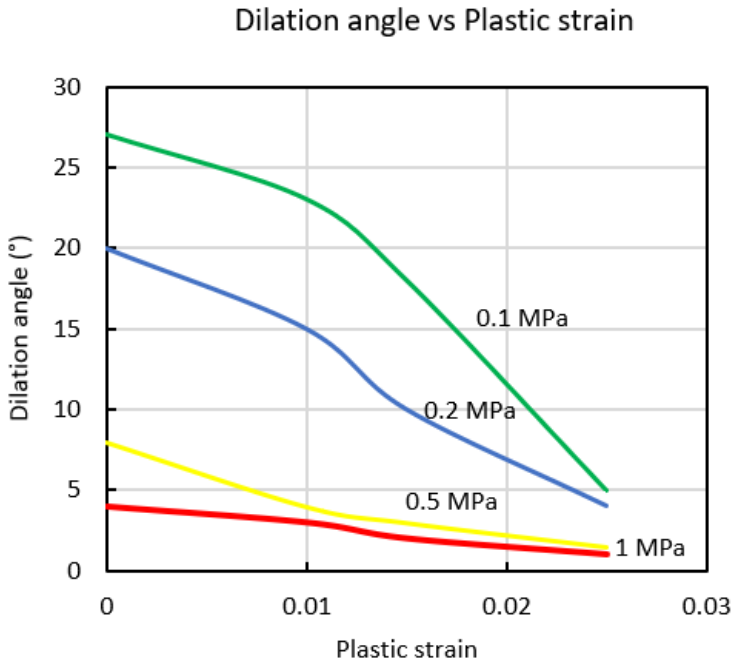

Figure 32. Relationship between dilation angle and plastic shear strain at different confinement level

3.3 Summary

For each formation, four triaxial tests have been conducted and provided for this research. Laboratory results show strain hardening and softening behaviors on the stress-strain curves. Besides, dilation behaviors can also be observed. The strain hardening/softening constitutive models have been calibrated to generate the best fit strength parameters for Clearwater and Wabiskaw formations. In general, simulation predictions and experimental observations show good agreement over the confining stresses utilized for the laboratory program. Considering the strength parameter variation tendencies proposed in the CWFS model, the cohesion weakening and friction mobilization equations have been generated. The constitutive models and their associated parameters determined in this chapter are utilized to represent caprock geomechanical behavior in modeling studies for the in situ stress calculations (Chapter 4).

4 Determination of In-situ Stresses

4.1 Overburden Stress

In general, the in-situ stresses can be decomposed into three orthogonal principal stresses. Because of tectonic forces and ground surface geological features, the stress state in the shallower subsurface generally is more variable and uncertain than deeper formations. For this research study, it has been assumed that the vertical stress is one of the principal stress directions and consequently, the other two principal stresses lie in the horizontal direction. The magnitude of the vertical total stress has been determined by integrating the density log and for missing data from the surface down to 41 m, it has been assumed as constant at 2.1 g/cm^3.

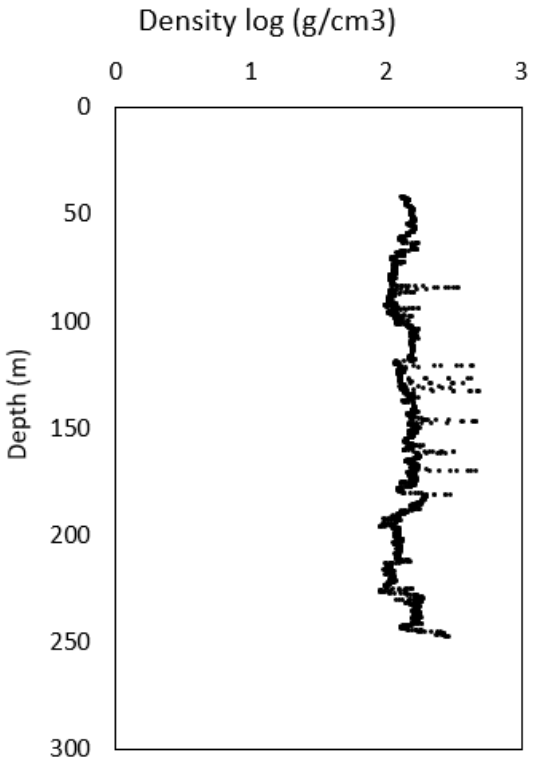

Figure 33. Density log of Well 8-29

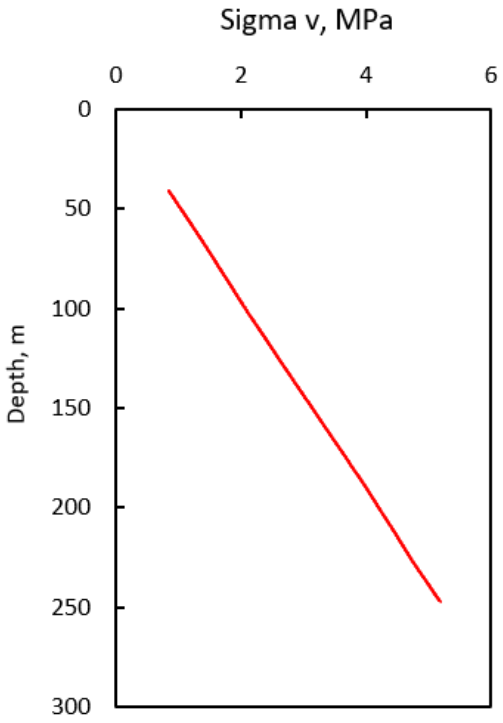

Figure 34. The profile of the overburden stress of along Well 8-29

4.2 Minimum Horizontal Stress

4.2.1 Direction of σ_h

Borehole failure processes, breakouts and fractures, have been used to determine the directions of horizontal stresses. A borehole breakout is a compression failure that occurs at the borehole wall in the direction of the minimum horizontal stress, σ_h while the induced fracture is a tensile failure that occurs in the direction of the maximum horizontal stress, σ_H. By identifying the existence of breakouts or induced fractures, the direction of either of the two horizontal stresses can be determined. The borehole failure information can in turn be interpreted by image log data and caliper log data.

The logging tool used to generate the data provided for this research was a six-arm caliper which has six independent arms to give an accurate measurement of the borehole cross-section. The first

function of the six-arm caliper is to provide a borehole image based on resistivity contrasts to analyze borehole failure – breakout, key-seat and washouts. Figure 35 illustrates the results from the Well 8-29 image log that shows multiple regions of borehole failure. Enlargement areas are identified as poorly resolved zones and circled in Figure 35. In the figure, eight cases show that most of the wellbore failures are washouts. Between the depth of 60 m to 61 m, a big key-seat more than 90˚ was identified in the northeast direction. Only two breakouts have been identified shown in the picture. The first one is between 127 m to 128 m which is in the Clearwater Formation and the other one is between 237 m to 239 m which is in the McMurray Formation. The two breakouts are oriented in the east and west directions.

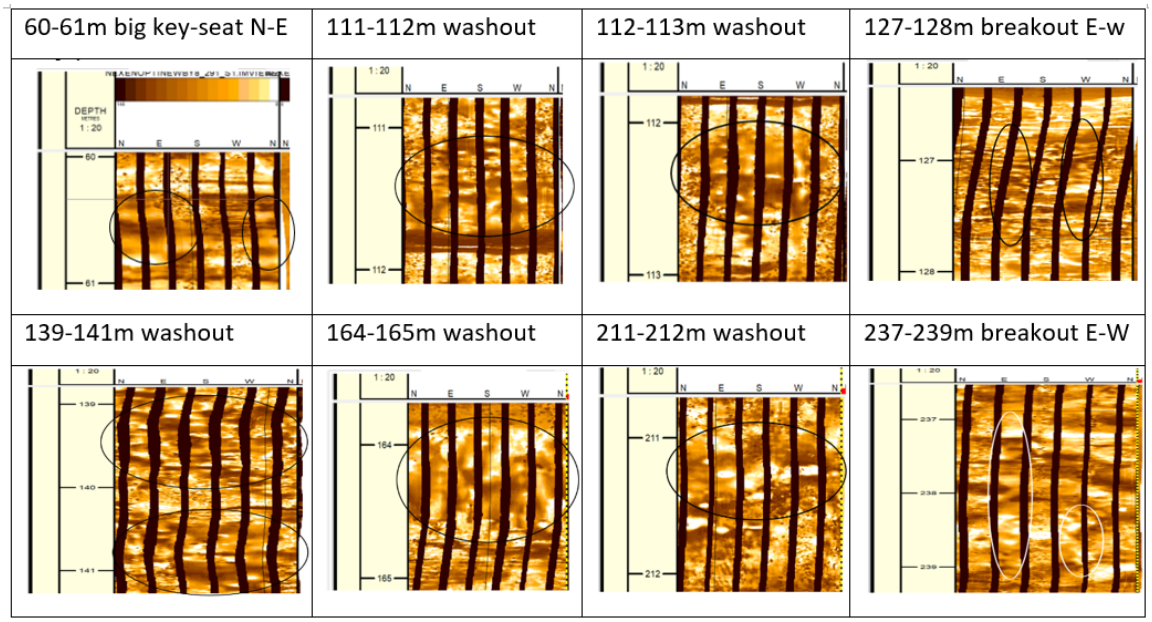

Figure 35. Wellbore failures along Well 8-29

The second function of a six-arm caliper is to measure the borehole geometry. The borehole diameter is measured by three sets of opposite arms. It is straightforward to identify where enlargement has occurred simply by drawing the borehole shape based on the six caliper measurements. Another advantage of the six-arm caliper is to distinguish between symmetrical

(stress-induced breakout) and asymmetrical (artificial key seat) failure types (Jarosiński 1998). However, unlike other tools such as four-arm calipers, which use two orthogonal pairs of caliper arms to help centralize the tool, the six-arm caliper has a unique tool decentralization challenge. The eccentricity can impact the measurement accuracy, so it becomes more complicated to determine the borehole geometry when a six-arm caliper is used and becomes more challenging for deviated wells. Hence, it is necessary to correct for tool eccentricity and ensure all caliper readings are referenced to the center of the borehole. Four methods were considered in this research to calibrate the data, as described below, with the elliptical algorithm, chord method and circle method ultimately chosen for the eccentricity analyses.

(1) Elliptical algorithm (Schwerzmann, Funk, and Blatter 2006): This method is particularly well suited for the condition of borehole breakout - it considers the borehole shape as an ellipse as the long side represents the breakout. The ellipse method is applicable for both elliptical and circular borehole shapes because a circle is simply a special case of an ellipse (Wagner, Müller, and Tingay 2004);

(2) Center of mass method (Jarosiński 1998): This method considers the pad as a point mass with the same mass m = 1; the coordinates of the tool center are then calculated by the summation of the pad vectors;

(3) Chord method (Wagner, Müller, and Tingay 2004): The chord approach uses the theorem of Pythagoras and the rule of chords to calibrate the caliper data. The offset determined by this method is always double the value resulting from the center of mass; and

(4) Circle method (Wagner, Müller, and Tingay 2004): The basic idea for this method is that any three points not in a straight line but in one plane can define a circle. By connecting the three points, a triangle can be formed. The perpendicular bisectors of the three lines

intersect at the center of the circle; For irregular borehole shape, all pads combinations need to be considered to get an average value of borehole center.

The error arising from the use of the above four methodologies has been summarized in Table 9 (Wagner et al., 2004). The error from using the center of mass approach is one to two times of the chord method and consequently, this approach was not adopted in the calibration of the caliper data for this research. In general, the following recommendations are given for choosing a particular method (Wagner et al., 2004): 1) both circle and chord method are suitable for circular borehole shape – for this research only the circle method was used because of the simplicity; 2) the ellipse algorithm is used for the condition of breakouts and 3) the chord approach is used in the key-seats regions.

Table 9. Comparison of result error of four tool decentralization methods.

Borehole Condition	Tool decentralization error (% of borehole radius)			
	Circle method	Ellipse algorithm	Center of mass method	Chord method
Circular boreholes	0	0	/	0
Elliptical boreholes	65	0	50	25
Small key-seats	40	50	45	20
Big key-seats	65	35	55	45

With horizonal stress anisotropy, the borehole wall will deform unequally. Elongation occurs in the direction of minimum horizontal stress while compression occurs in the direction of maximum horizontal stress. Generally, the deformation is not large enough to form breakouts or induced fractures but can still be used to diagnose the stress anisotropy and determine the orientations of the horizontal principal stresses (Figure 36).

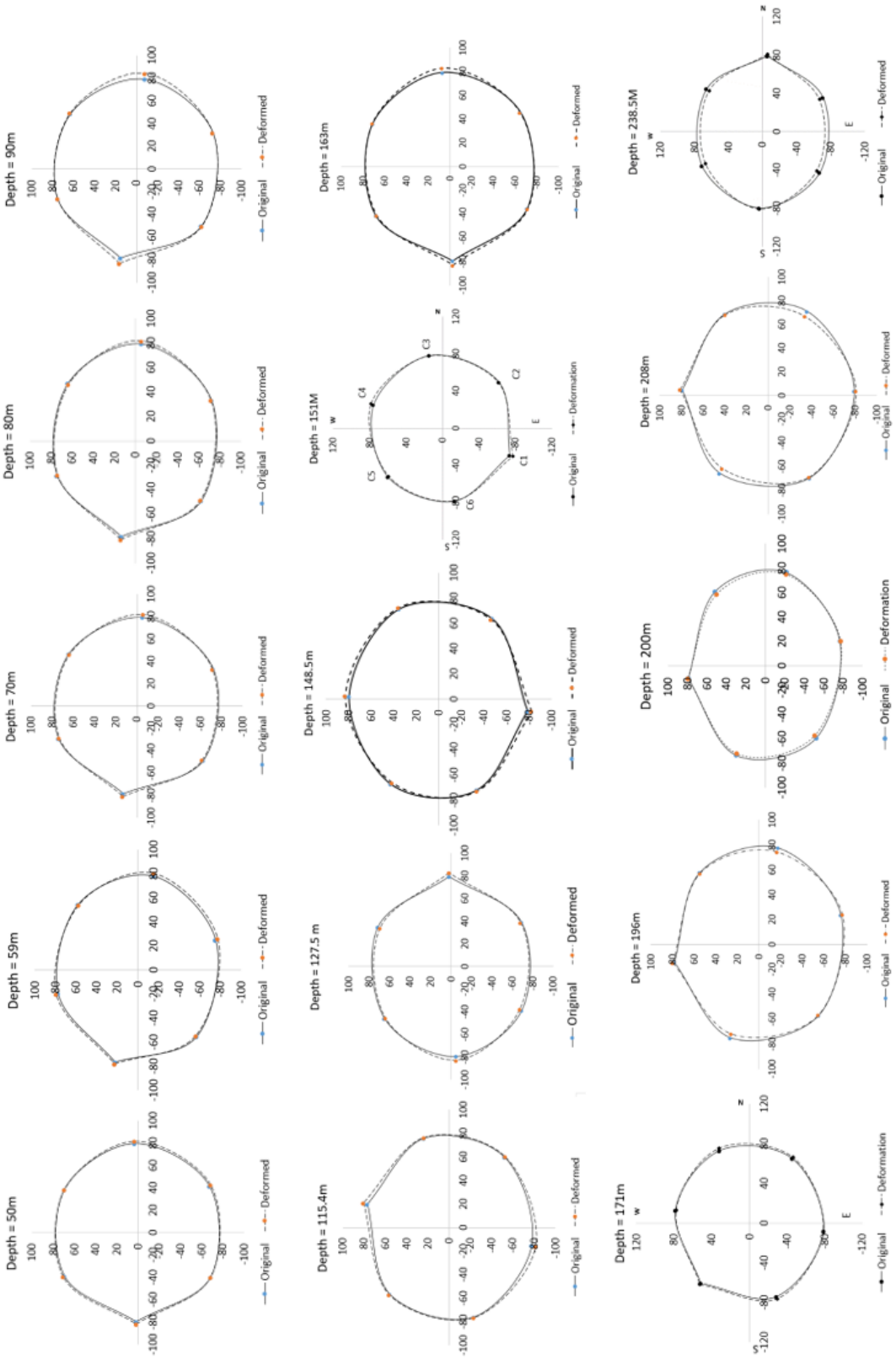

Figure 36. Distorted wellbore shape at different depths

After the correction of tool decentralization using the three methods mentioned above, the calibrated caliper data were used to plot the deformed shape of the wellbore section for different depths along Well 8-29. Combining the image log and caliper log, a set of data points in the direction of σ_h were generated and are summarized in Figure 37. In the upper strata between the depth of 50 m to 100 m which consists of quaternary sediments, σ_h is roughly aligned in the north-south direction with a standard deviation of 4.3˚. Between 100 m to 190 m which correspond to the depths of the Clearwater and Wabiskaw Formations, large variations of σ_h orientations can be observed in Figure 37 which can also be proved by the large standard deviation number 43.2˚. Variations in stress orientation with depth was also observed in Well 7-32-89-10W4 (Idowu 2011), which is also located in the Athabasca oil sands region. This example is a good demonstration for variation in stress orientation with depth. Nine borehole breakouts were examined over a depth interval of 1182.3 m to 2143 m. Two significant stress orientations between two depth intervals can be observed in Figure 38. In the McMurray Formation, σ_h has an average direction of 94˚ and 274˚ from the north with a standard deviation of 4.9˚. Consequently, σ_h in the McMurray Formation is aligned in the east-west direction.

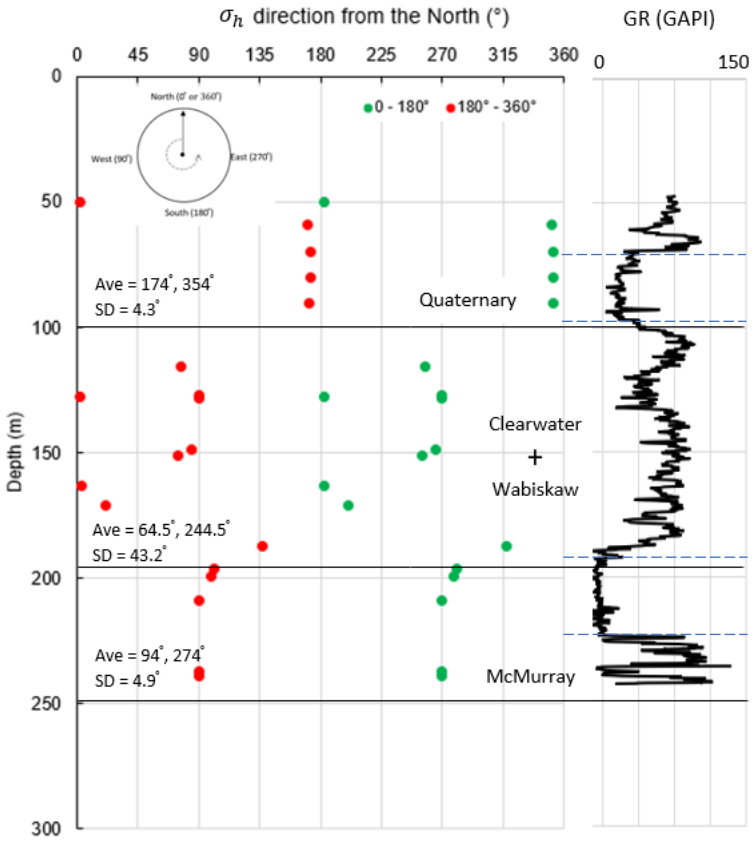

Figure 37. Directions of σ_h along Well 8-29

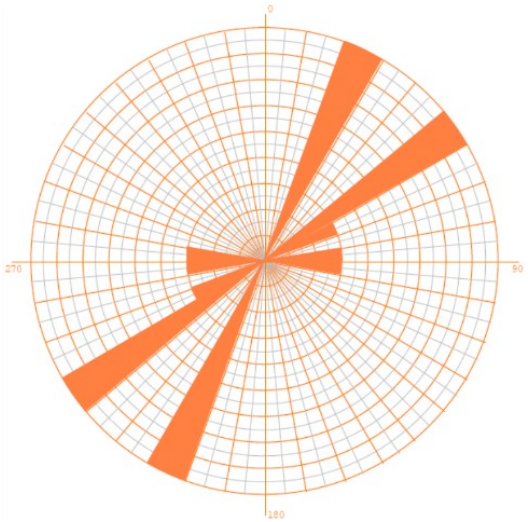

Figure 38. Minimum horizontal stress direction in Well 7-32-89- 10W4

Estimating the orientation of the minimum horizontal stress over different regional scales can also be problematic. Based on the database of breakout azimuths for 181 wells in the Western Canadian Sedimentary Basin (Bell et al., 1990), the majority of the orientations are in northwest-southeast direction, which is different than the result obtained from the analysis of the Well 8-29 data. The gamma ray log of Well 8-29 is shown in the right side of Figure 37. Between the depth of 70 m – 100 m, Quaternary deposits have a low gamma ray value. The gamma ray value is relatively constant reflects the uniform components and the homogeneity of the formation, therefore the orientation of σ_h remain constant with depth. Same situation exits in the McMurray Formation between 190 m to 230 m, the orientations of σ_h are roughly the same with little deviation along this depth interval. However, in the Clearwater and Wabiskaw Formation, the variable gamma ray suggests compositional changes in this formation. Also, based on the lithology, the main component of the caprock formation is mudstone which is also interbedded with siderite and silty sand. The stratigraphic properties shift back and forth between sandstone and shale. This heterogeneity of the formation composition causes stress orientation variations to a greater extent in those component transition zones. Another possible reason for the orientation change of the horizontal stresses at this well location is illustrated in Figure 39. On the west side of the well, a very deep Quaternary channel was eroded into major formations likely resulting in significant stress variations both during erosion and subsequent infilling of the channel. These processes along with associated collapse features illustrated in Figure 39 has very likely altered the local stress directions from those at a larger regional scale.

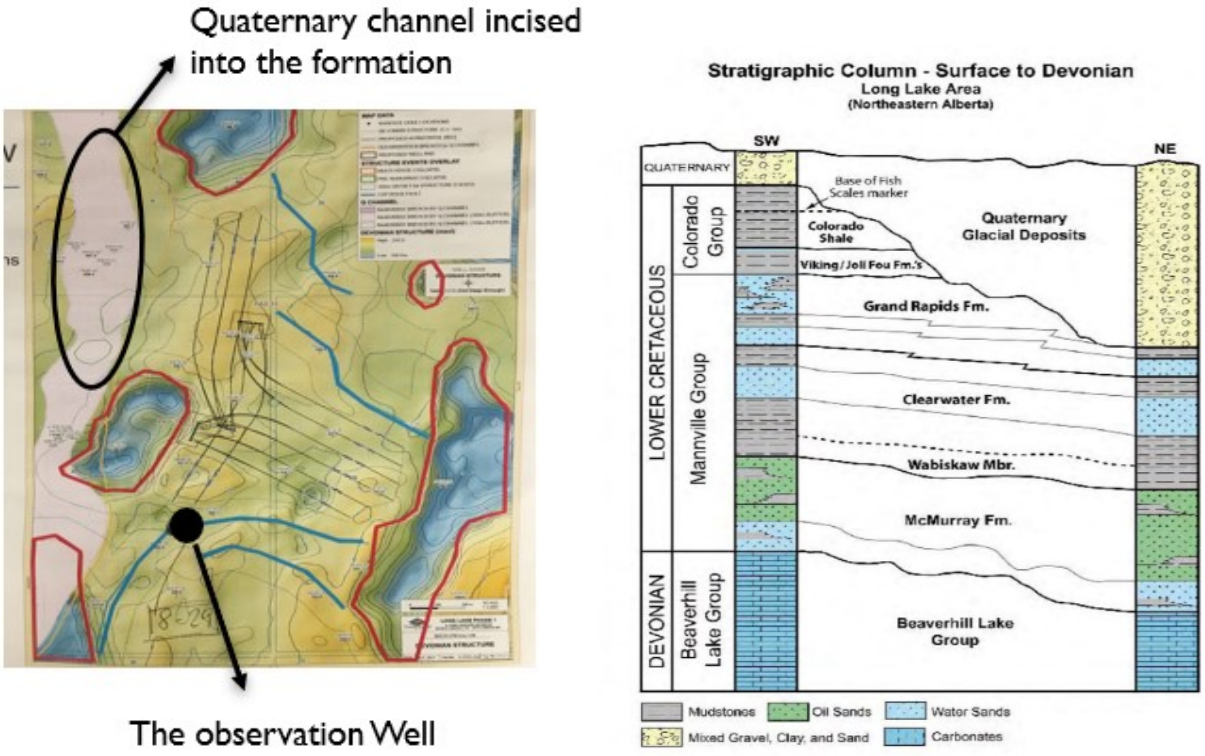

Figure 39. Well map and geological features around Well 8-29

4.2.2 Magnitude of σ_h

DFIT or mini-frac tests conducted in Well 8-29 have been provided to allow for the interpretation of the minimum in-situ stress. In each test, fluid was injected 5-7 times to ensure the fracture was beyond the wellbore affected region (Powless 2012). In most interpretation methods, the fracture closure pressure (FCP) on the pressure curve (bottom-hole pressure vs time) is regarded as the best estimate of the minimum in-situ stress. However, rocks are complex, heterogeneous materials with sets of natural fractures, microfractures and plane of weakness. These characteristics result in various closure mechanisms including pressure dependent leak-off associated with pre-existing fissures opening. Because of these processes, many pressure fall-off curves following shut-in do

not follow ideal shapes because of multiple closure mechanisms along with wellbore storage. Consequently, different methods are needed to interpret the data.

4.2.3 Discussion on Interpretation Methods

A total of four DFIT's were conducted in the Well 8-29. The four intervals are: the Clearwater Formation at 151 m depth, the Wabiskaw Formation at 171 m depth, the McMurray Formation at depths of 207 m and 237 m. For each test, 3 well-behaved cycles of pressure curves were selected, and 7 methods were used to interpret the fracture closure pressure. The following section will show the analysis plots and demonstrate the interpretation of the results obtained from a DFIT conducted at the depth of 151 m in the Clearwater Formation. Interpretation plots for the other three DFITs are provided in Appendix A.

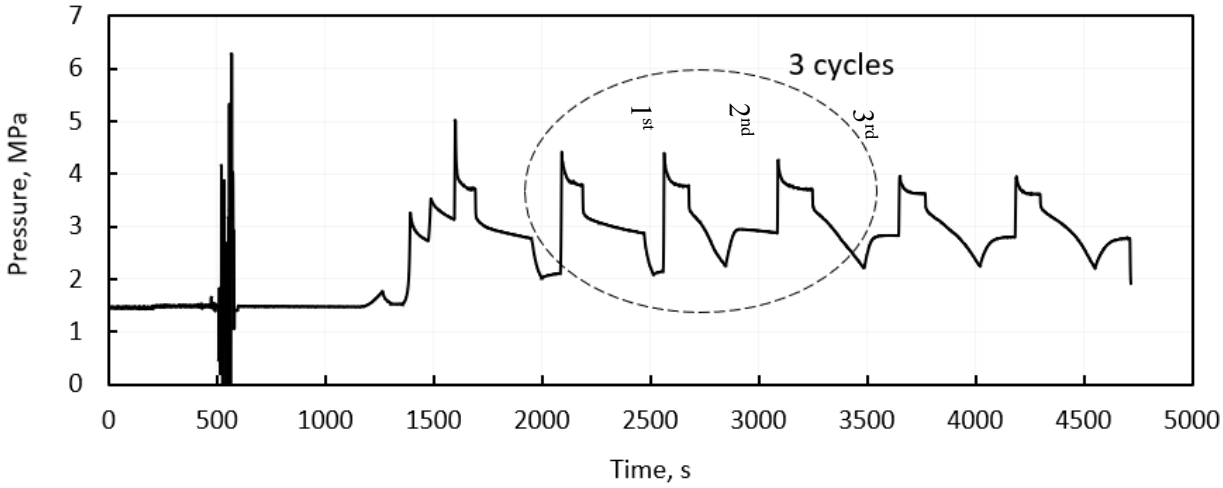

Figure 40. Multiple cycles in a DFIT (Mini-frac test)

4.2.3.1 G-Function Method

The holistic method (Barree, Barree, and Craig 2009) and the fracture compliance method (Cramer 2015) are both considered in the G-function plots. In the holistic method, the expected signature of the GdP/dG curve is a straight line though the origin and the closure are identified by the

departure from the straight line. Figure 41 shows the first pressure fall-off cycle at the depth of 151 m. According to Barree (2009), the "belly" shape of the GdP/dG curve indicates a storage phenomenon. The closure event happened at G = 12.4 which gives a closure pressure 2.7MPa. In the fracture compliance method, the characteristic derivative signatures are the upward inflection from the initial GdP/dG straight line or the departure from the minimum in dP/dG curve. Both criteria are satisfied at G = 0.48 in the 1st cycle. This time the fracture closure pressure is predicted as 3.1 MPa.

In the 2nd cycle (Figure 42), the closure pressure is 2.75 MPa from the holistic method and is 3.1 MPa from fracture compliance method. Some other local minimums on the pressure derivative curve (identified by black circles) can be seen in Figure 42. DFITs are short time period tests conducted several times within a test interval. During each pressure build-up and fall-off cycle, only hundreds of data points can be collected. Those data points are enough to describe subtle pressure changes while for pressure derivatives, fluctuations will show up in the plots which may be one of the reasons for the local minimums. Another possible cause is the reduction of the residual apertures. After the first mechanical closure at G = 0.48, it is possible for a residual fracture aperture to remain. As the fluid pressure within the fracture continues to drop, the residual aperture will slowly reduce due to the overburden stress and result in a second or partial "closure" event. In the 3rd cycle, closure pressure predicted by fracture compliance method is 3 MPa. The holistic method doesn't fit in this data.

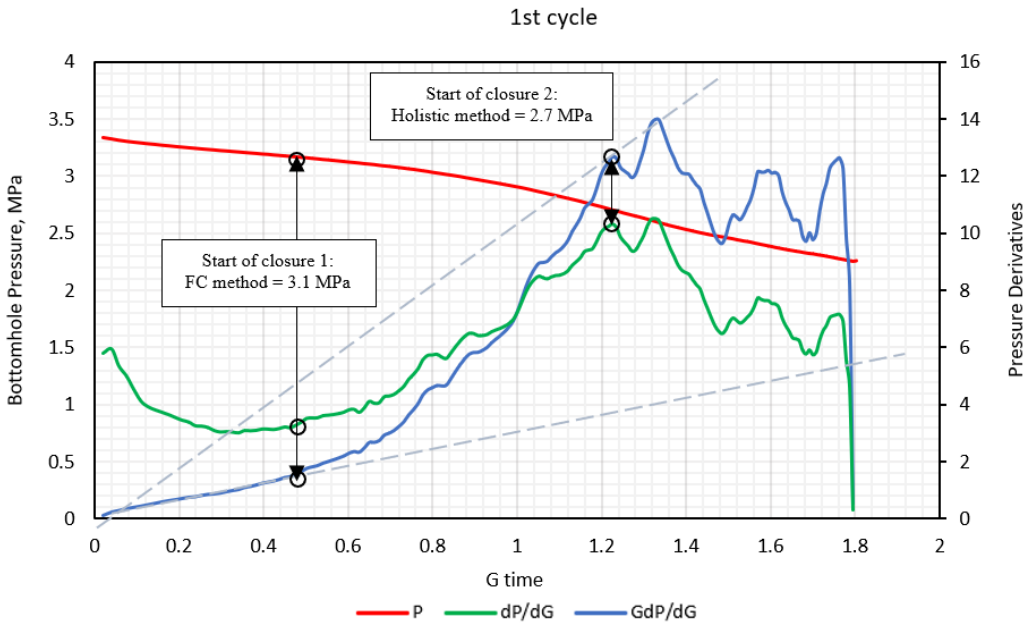

Figure 41. G - function plot for data of the 1st DFIT cycle at 151 m

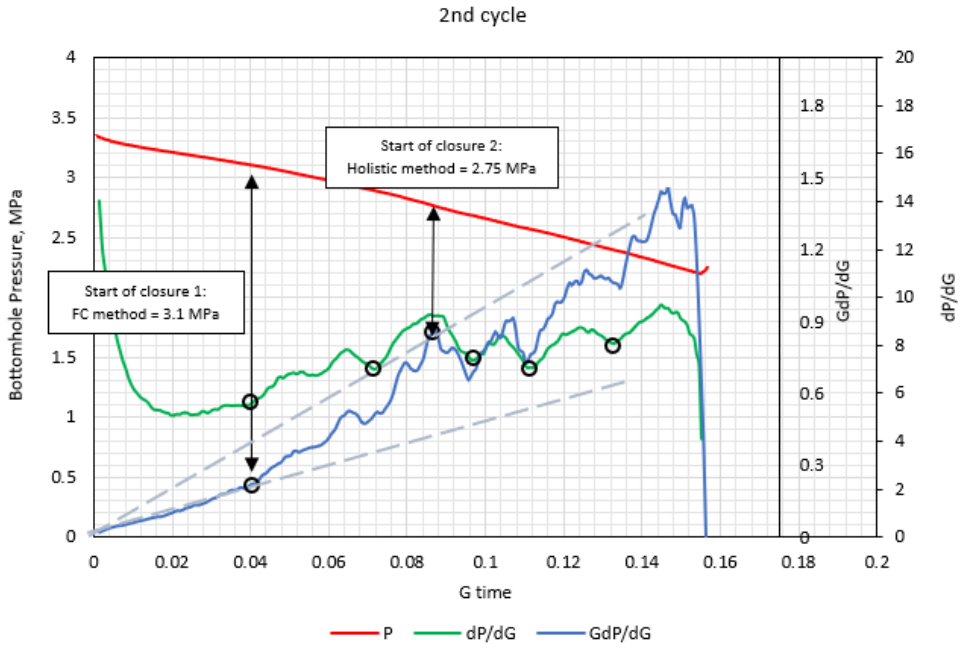

Figure 42. G - function plot for data of the 2nd DFIT cycle at 151 m

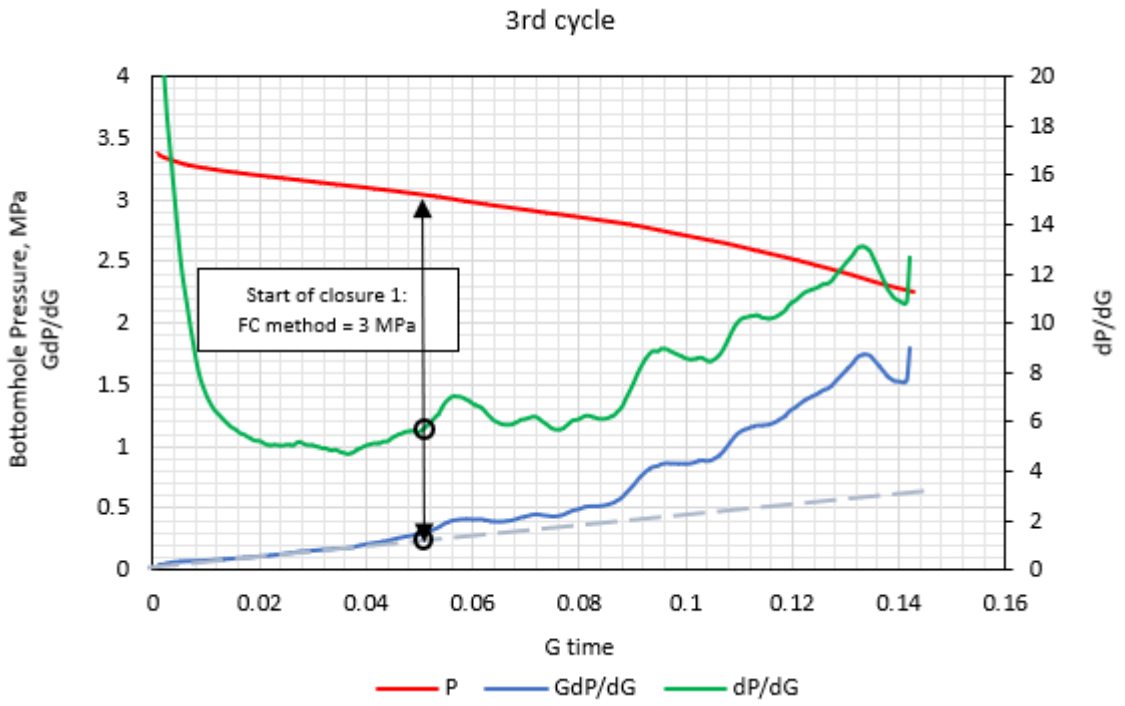

Figure 43. G - function plot for data of the 3rd DFIT cycle at 151 m

4.2.3.2 Square Root of Time

Figures 44-46 illustrate the square root of time results for the 3 DFIT cycles. The fracture closure pressure is selected by the maximum point of the derivative and similar to the way the G-function closure is picked, fracture compliance method can also be implemented here. The closure events are marked in Figure 44-46 and are 3.14 MPa, 3.15 MPa and 3.12 MPa for cycles 1, 2 and 3 respectively. The closure points interpreted here must also satisfy the requirement on the G-function method otherwise they aren't considered a closure event (Barree, Barree, and Craig 2009).

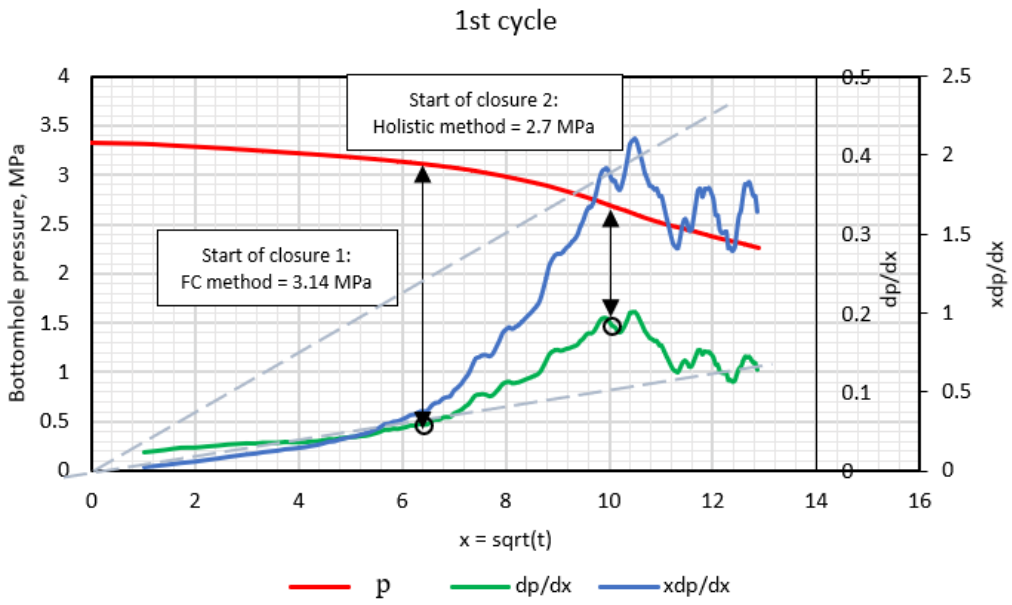

Figure 44. Sqrt (t) plot for data of the 1st DFIT cycle at 151 m

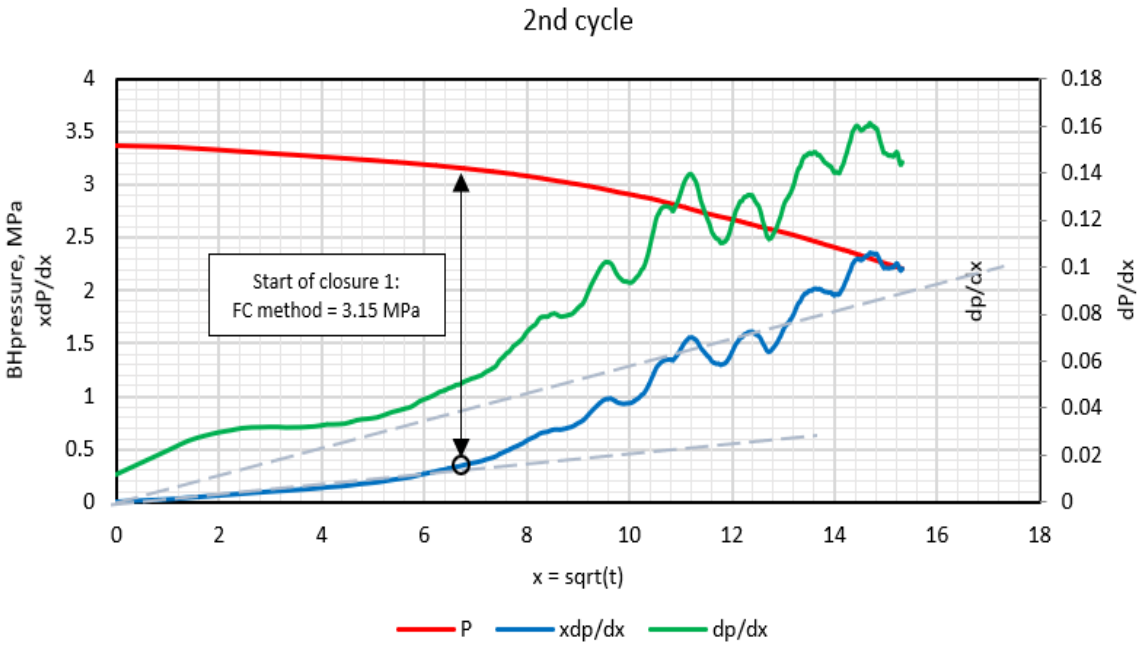

Figure 45. Sqrt (t) plot for data of the 2nd DFIT cycle at 151 m

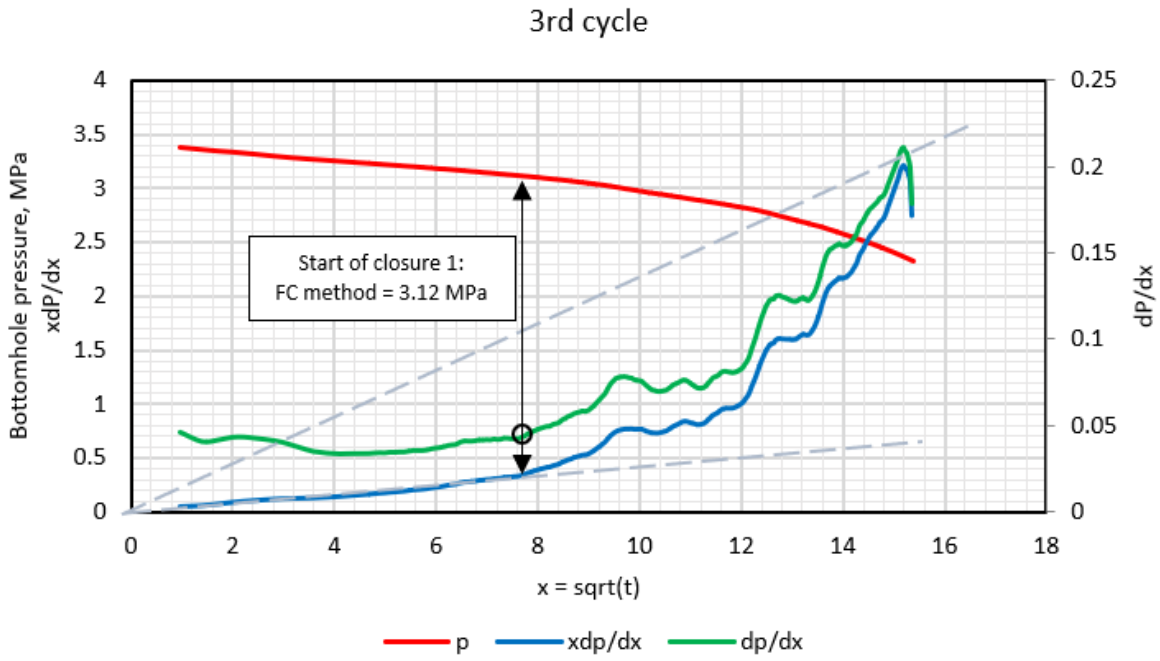

Figure 46. Sqrt (t) plot for data of the 3rd DFIT cycle at 151 m

4.2.3.3 Log-Log Plot

In the log-log diagnostic plot, the pressure derivative is defined as ΔtdΔP/dΔt. A characteristic slope of 3/2 represents fracture closure. Figures 47-49 show the log-log diagnostic plots of the three fall-off cycles at the depth of 151 m. From the logarithmic derivative (green curve) we can identify an early ½ slope derivative trend, a 3/2 slope for fracture closure and a late time 0 slope derivative trend. The ½ slope trend represents an early time linear flow. The intersection between early time ½ slope and the subsequent 3/2 slope indicates the start of closure at 3.07 MPa. After the 3/2 slope trend, the logarithmic derivative becomes constant (0 slope) when the pressure falloff is dominated by radial flow. At this time, the fracture has completely closed, and the closure pressure is interpreted as 2.7 MPa. Primary pressure derivative (PPD) is integrated with the log-log derivative to predict consistent fracture closure. The PPD appears to increase while fracture closing and continues decreasing after the fracture is closed.

In the second and third cycles, pressures at the start of the closure are almost the same as the first cycle; namely, 3.1 MPa and 3.08 MPa. However, the test was not conducted long enough to detect the transition to a radial flow regime and so it was not possible to estimate the end of the closure period.

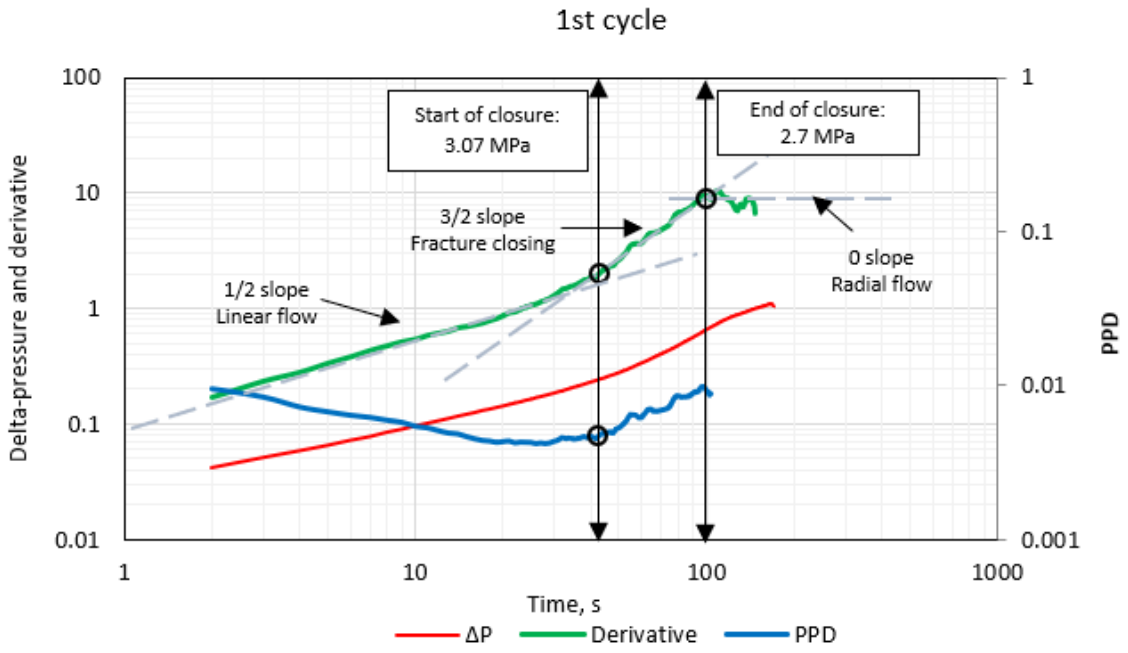

Figure 47. Log-log derivative plot for data of the 1st DFIT cycle at 151 m

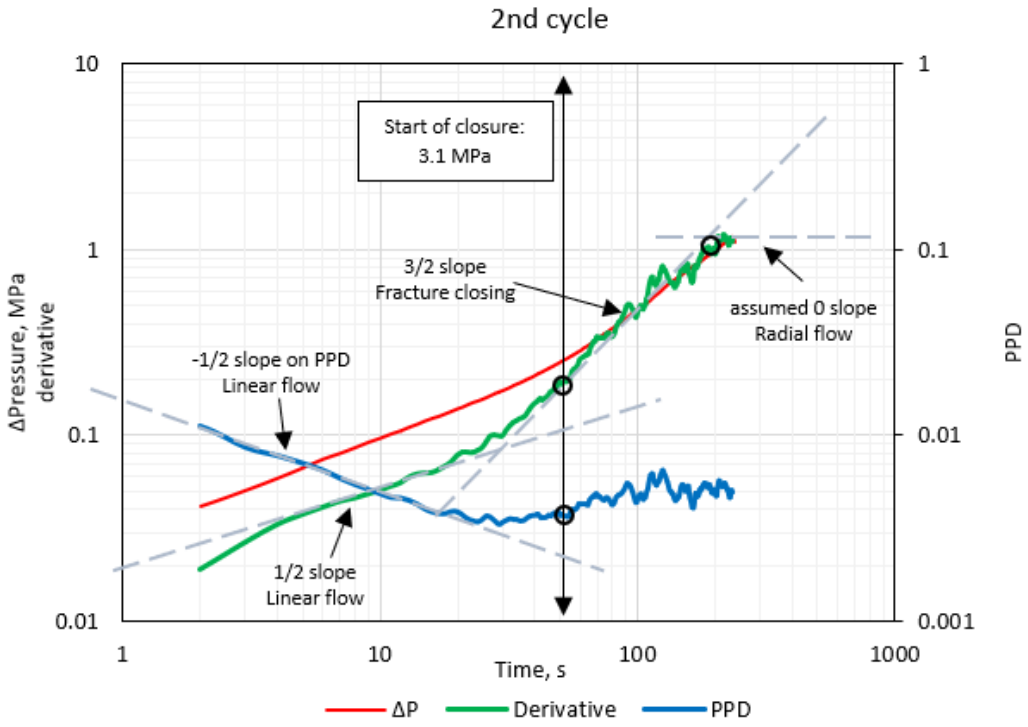

Figure 48. Log-log derivative plot for data of the 2nd DFIT cycle at 151 m

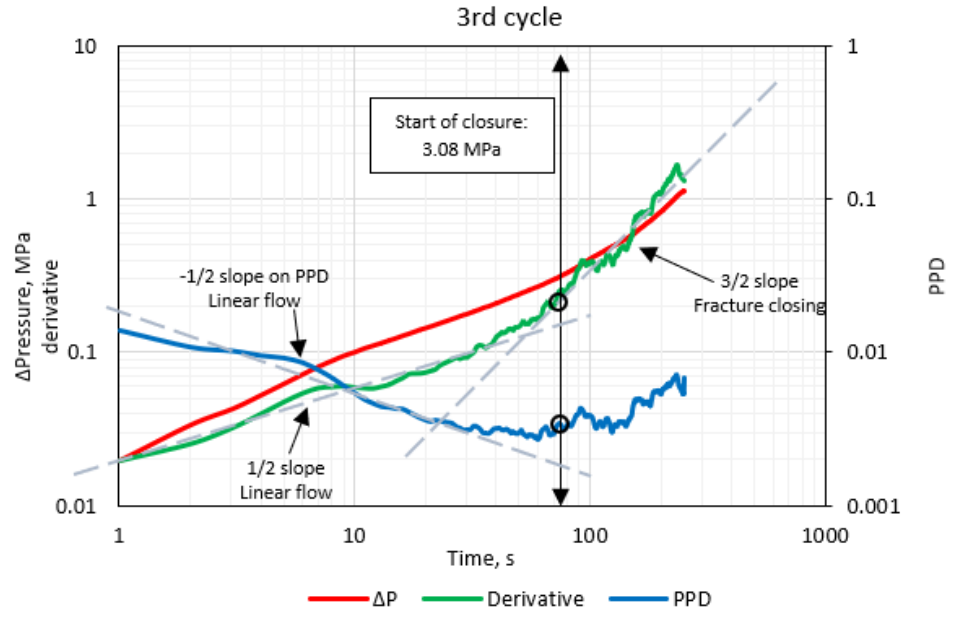

Figure 49. Log-log derivative plot for data of the 3rd DFIT cycle at 151 m

4.2.3.4 Bachman's Method

In this method, flow regimes are first identified using Bourdet log-log derivative plot. The function of Bourdet log-log derivative is different than ΔT log-log derivative which is ΔtdΔP/dΔt. It requires an assumption regarding to the flow regime. There are three different time functions defined for radial, linear and bilinear flow regimes (t_{er}, t_{el} and t_{eb} respectively). One of the advantages of the Bourdet log-log derivative technique is that the interpretation of flow regimes is not strongly affected by specific time functions. Only a minor distortion occurs if applying an alternate time function. Normally, radial flow is assumed in most of the commercial software. Therefore, the first Bourdet log-log derivative is defined as $t_{er}d\Delta P/dt_{er}$ in this research. Once a specific flow regime has been identified, a change in the Bourdet log-log derivative time function is made for that type of flow regime. And a new secondary Bourdet log-log derivative plot is generated to complete the analysis. Table 10 have been developed by Bachman, Walters, and Hawkes (2012) to aid the analysis in determining the various slopes for each recommended curve for each flow period and time range.

Table 10. Specialized time plotting functions and their slopes

Log-Log Flow Regime								
Equivalent time Derivative Function	Carter		Linear		Bilinear			
	Early time slope	Late time slope	Early time slope	Late time slope	Early time slope	Late time slope		
$\frac{t_{er}d\Delta P}{dt_{er}}$ (radial)	1/1	3/2	½	½	¼	¼		
$\frac{\Delta td\Delta P}{dt_{ec}}$ (Carter)	1/1	1/1	½	0	¼	-¼		
$\frac{\Delta t^{0.5}d\Delta P}{dt_{el}}$ (Linear)	1/1	3/2	½	½	¼	¼		
$\frac{\Delta t^{0.25}d\Delta P}{dt_{eb}}$ (Bilinear)	1/1	3/2	½	½	¼	¼		
Log-Log Flow Regime								
$PPD = \frac{d\Delta P}{d\Delta t}$	Radial		Carter		Linear		Bilinear	
	-1/1	-2/1	0	-1/2	-1/2	-3/2	-3/4	-7/4

It starts with the Bourdet log-log derivative which has an early ½ slope representing linear flow in Figure 50. Then, there is a transition into early and late time carter leak-off which have slopes of 1 and 3/2. After the late time carter leak-off occurs the fracture closure. The final flow regime is a late time bilinear flow period which has a slope of ¼. The associated slopes of the PPD curve are also labeled in the figure and give consistency for the flow regimes with the Bourdet log-log derivative curve. After carter leak-off has been identified, the equivalent carter leak-off log-log derivative is plotted in figure 51. According to Table 10, the carter flow regime appears as a unit slope on the equivalent curve for both early and late time carter leak-off. Characteristic slopes for the before and after closure flow regimes can also be found on this curve. The dP/dt_{sc} curve verifies the carter leak-off as a 0 slope and shows when it ends. At delta time = 19 s, the fracture closure occurs, the pressure at this time is 3.16 MPa. Similar to the log-log derivative method, no clear evidences of after-closure flow regimes. However, the end of carter flow can be identified on both equivalent curves. The fracture closure pressures are estimated as 3.15 MPa and 3.07 MPa, respectively.

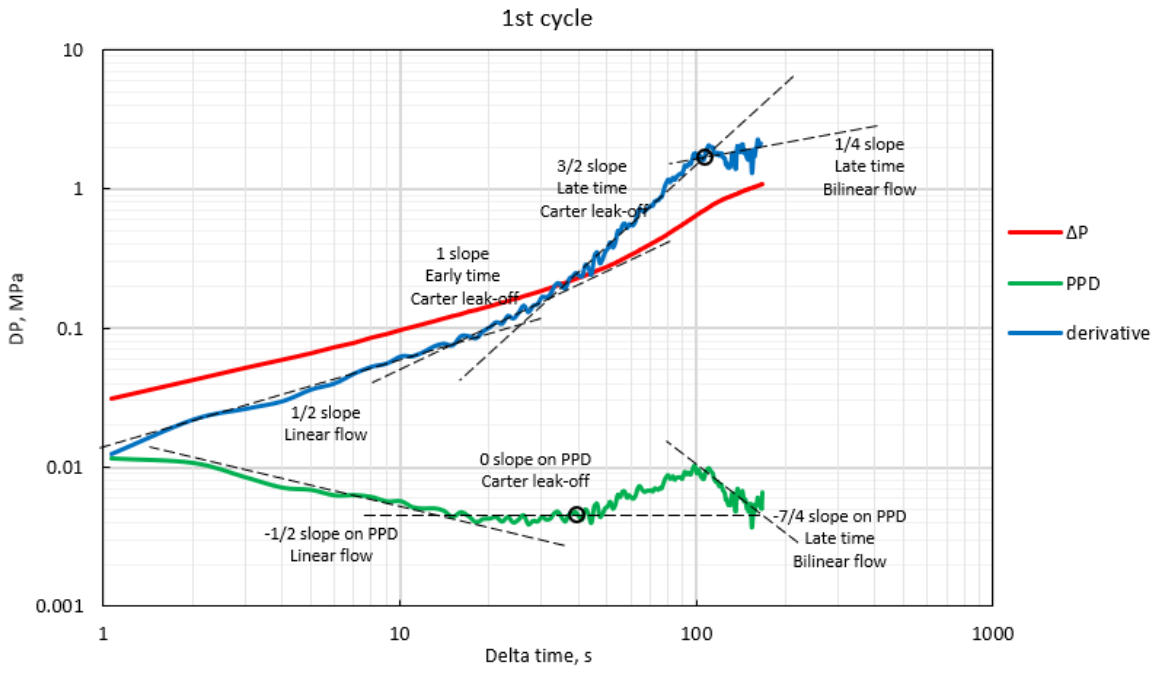

Figure 50. Bourdet log-log derivative and PPD plot for the 1st DFIT cycle at 151 m

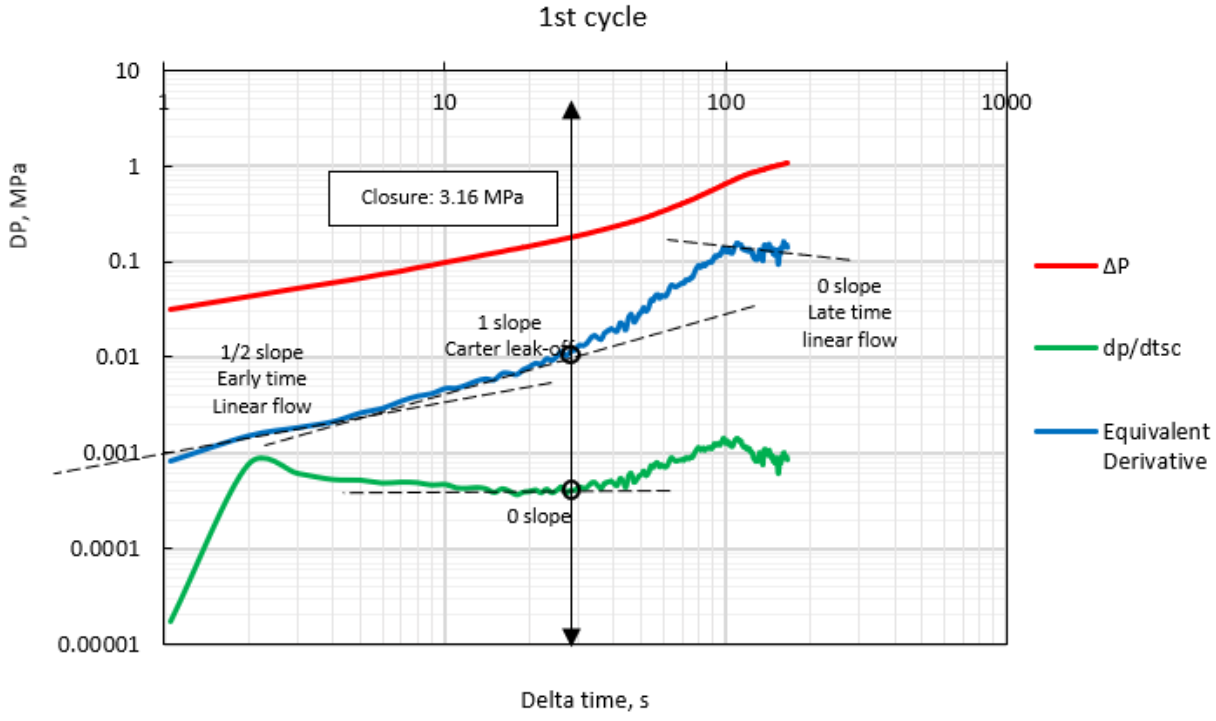

Figure 51. Equivalent Carter leak-off derivative plot for the 1st DFIT cycle at 151 m

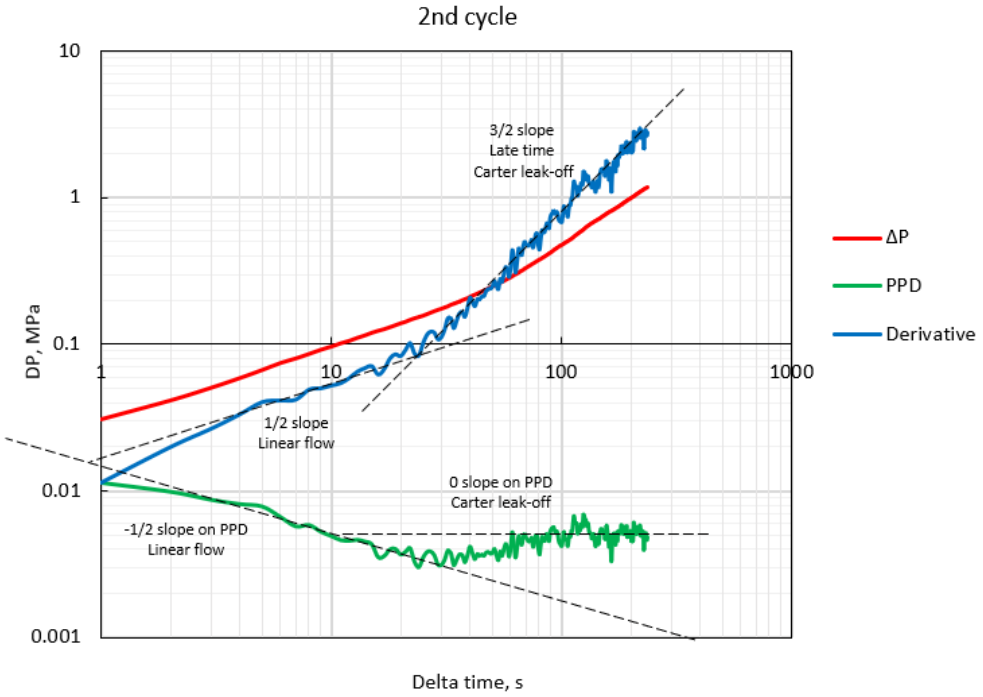

Figure 52. Bourdet log-log derivative and PPD plot for the 2nd DFIT cycle at 151 m

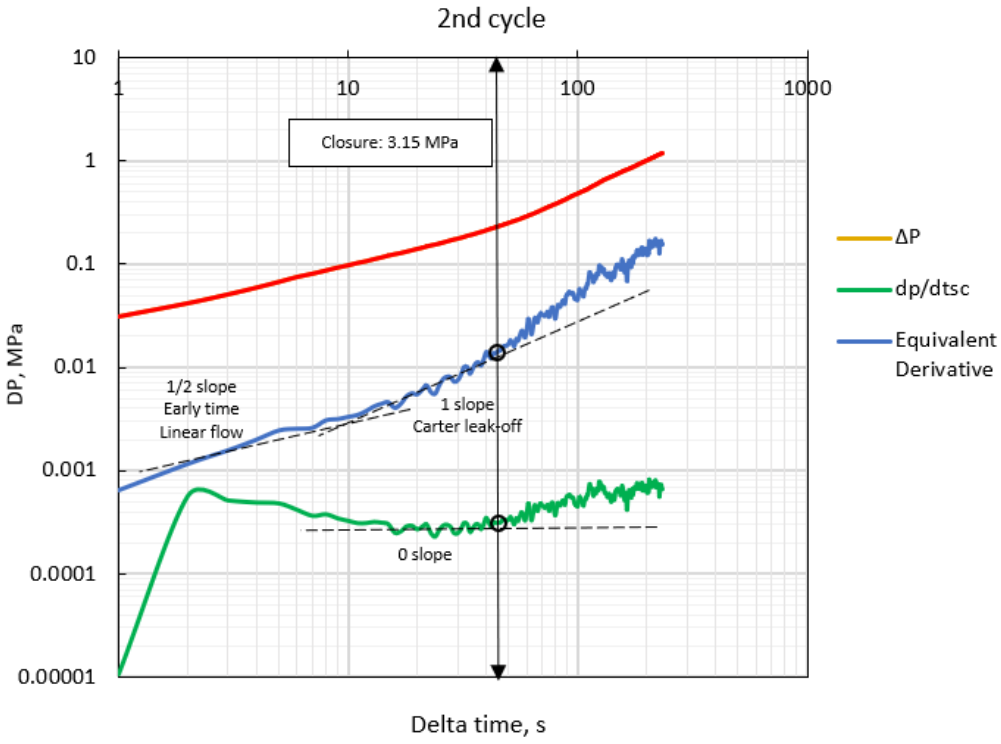

Figure 53. Equivalent Carter leak-off derivative plot for the 2nd DFIT cycle at 151 m

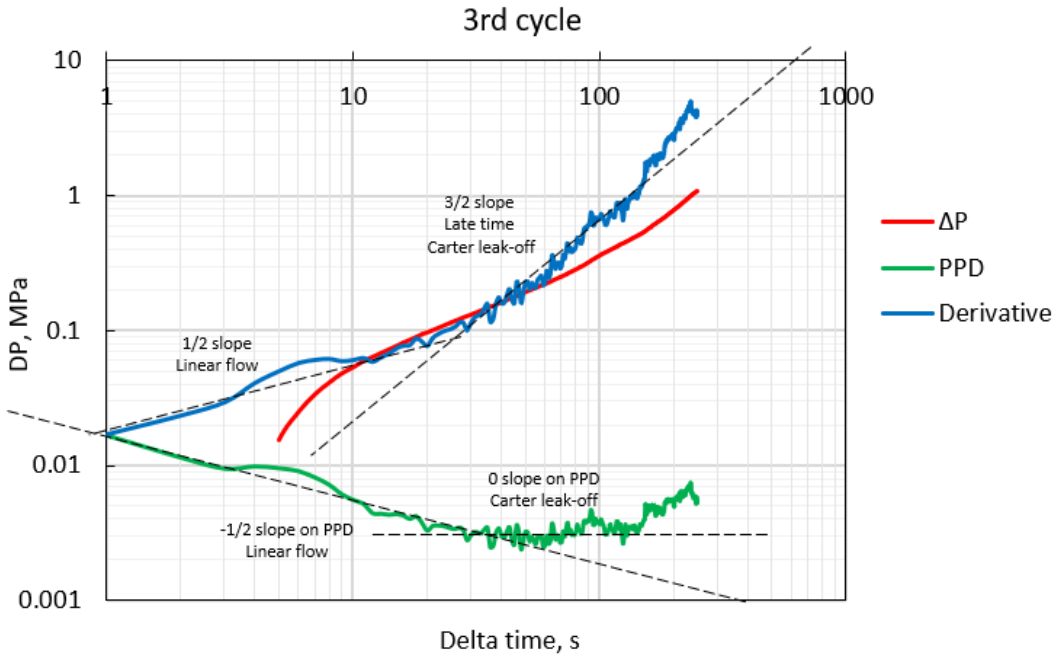

Figure 54. Bourdet log-log derivative and PPD plot for the 3rd DFIT cycle at 151 m

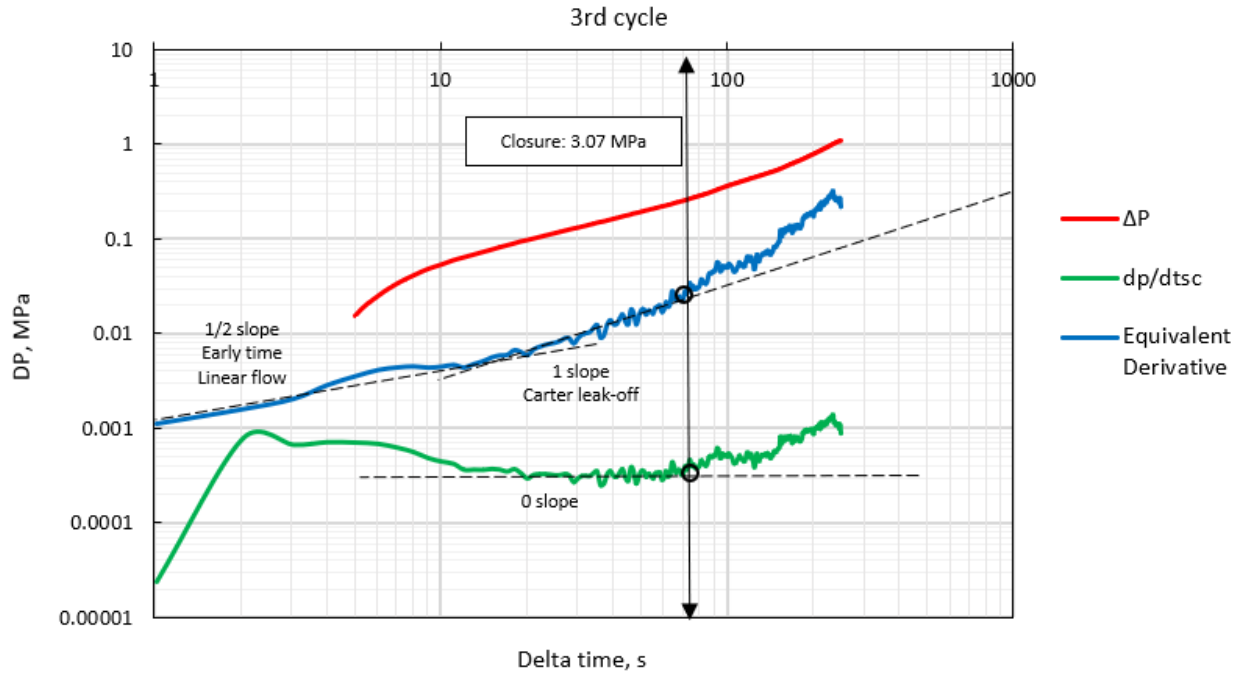

Figure 55. Equivalent Carter leak-off derivative plot for the 3rd DFIT cycle at 151 m

4.2.3.5 Horner plot:

Conventionally, a Horner plot is used to determine reservoir transmissibility. This method assumes that pseudoradial flow is the dominant flow regime in the pressure transient period before the fracture closes completely (Zadeh 2016). Horner time is defined as $(t_{inj}+dt)/dt$ and for a plot of pressure versus Horner time, as shown in Figures 56-58, the fall-off data will initially form a straight line and will begin to deviate from it once fracture closure occurs. All three cycles give consistent estimation of the closure pressure (2.9 MPa, 2.88MPa and 2.9 MPa).

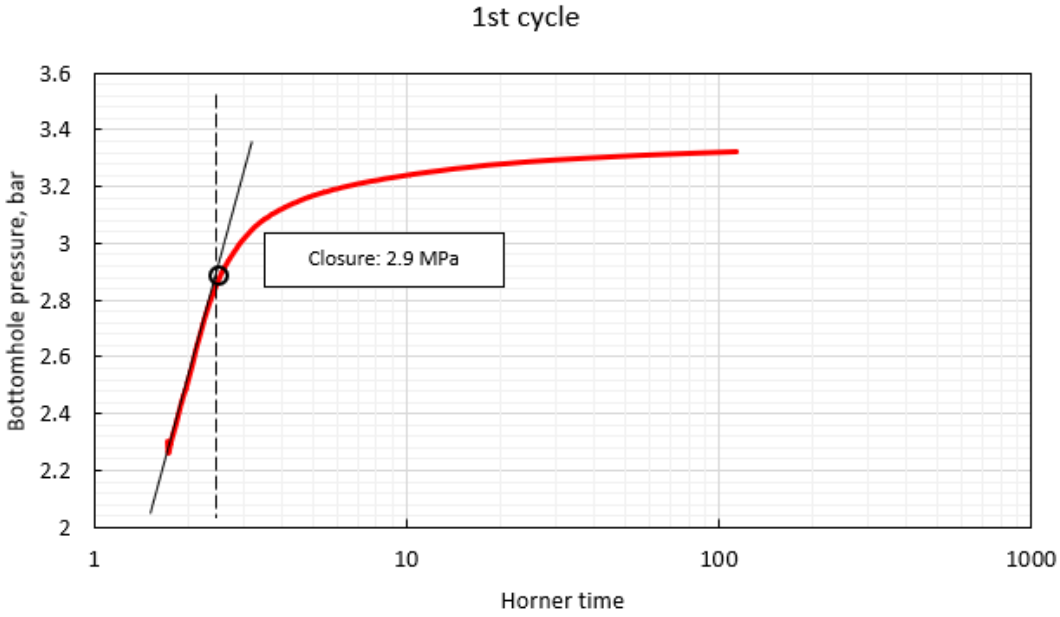

Figure 56. Horner plot for the 1st DFIT cycle at 151 m

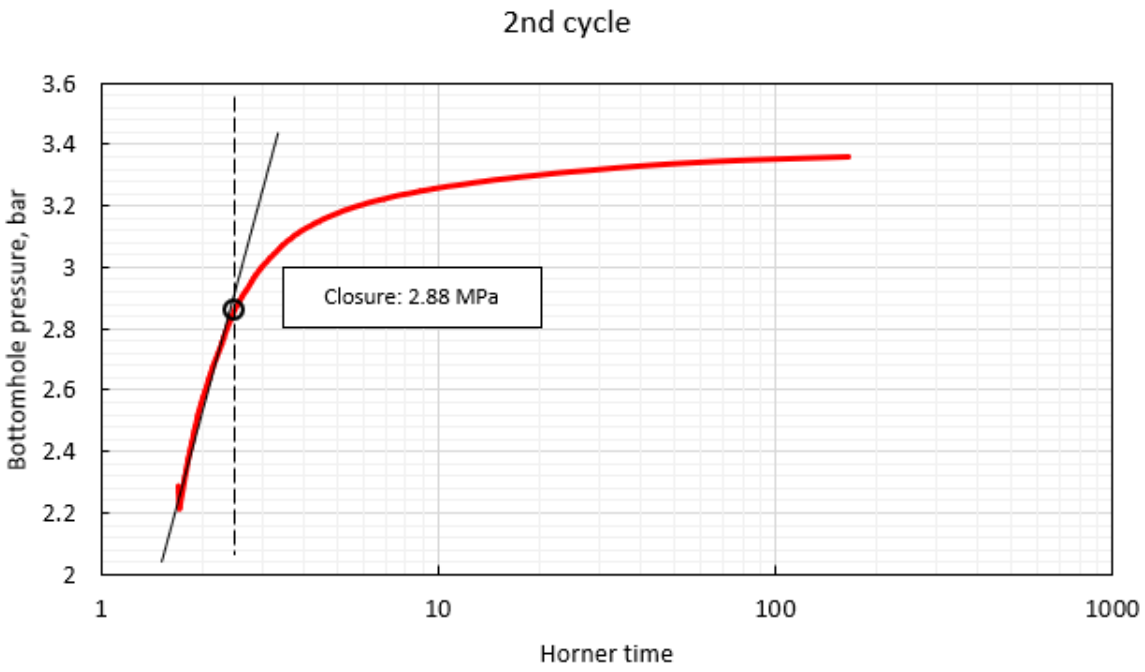

Figure 57. Horner plot for the 2nd DFIT cycle at 151 m

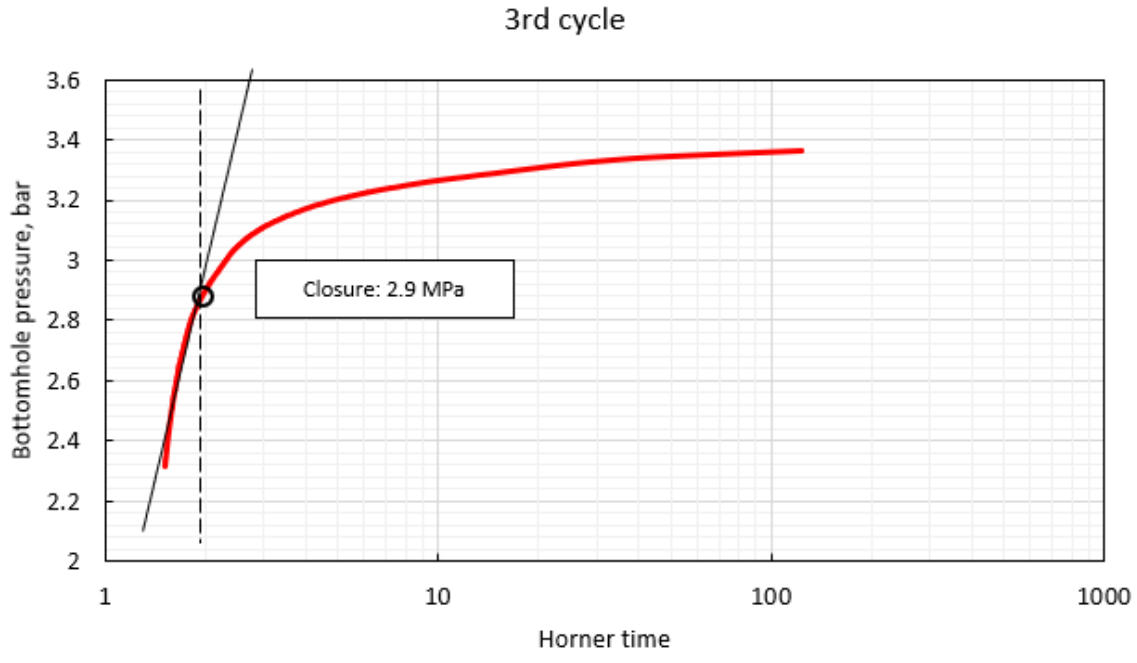

Figure 58. Horner plot for the 3rd DFIT cycle at 151 m

4.2.3.6 Pressure Decay Rate

The pressure decay rate method utilizes response from dP/dt versus bottom-hole pressure plot. These curves generally result in two bilinear segments with a transition zone separating them. As shown in Figures 59-61, the intersection point of the two trendlines is considered to be the closure pressure. The dP/dt vs P in pressure decay rate method shares a common theoretical foundation with the PPD method (dP/dt vs t). After shut-in, pressure is decreasing while the elapsed time is increasing. Consequently, the curves in Figures 59-61 can be considered as PPD curves if interpreting the horizontal axis from right to left. Consistent with the PPD method, the pressure decay rate method provides estimates of fracture closure pressure of 3.17 MPa, 3.23 MPa and 3.24 MPa for the three cycles.

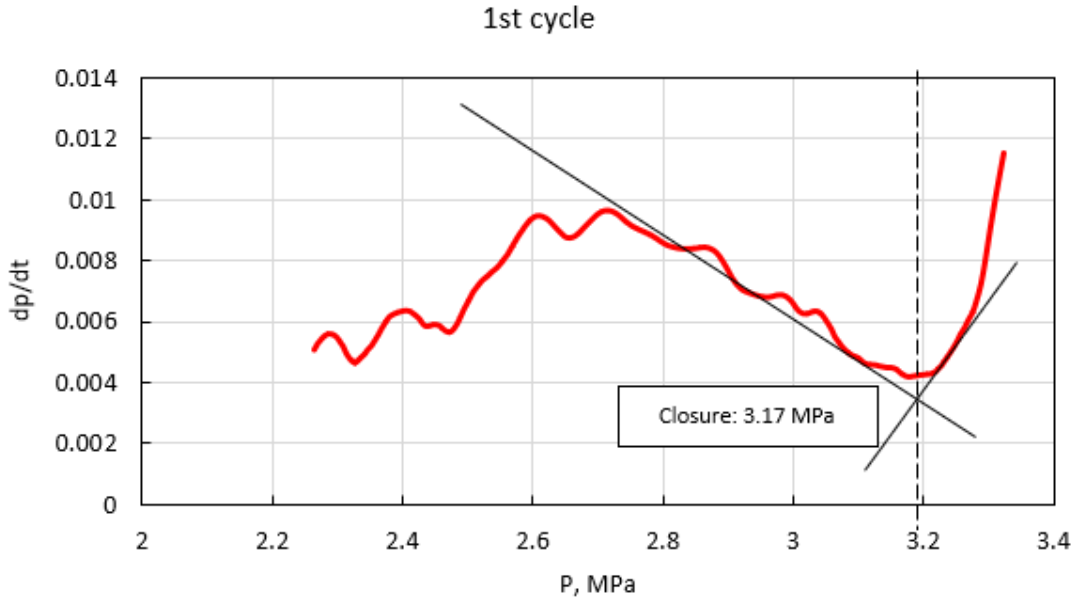

Figure 59. Pressure decay rate plot for the 1st DFIT cycle at 151 m

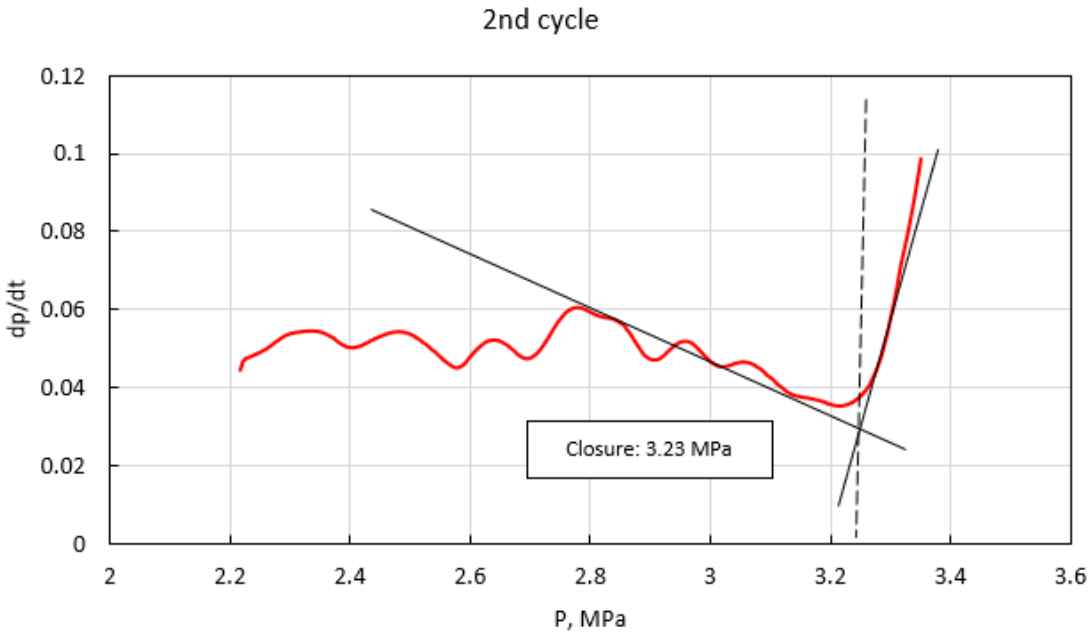

Figure 60. Pressure decay rate plot for the 2nd DFIT cycle at 151 m

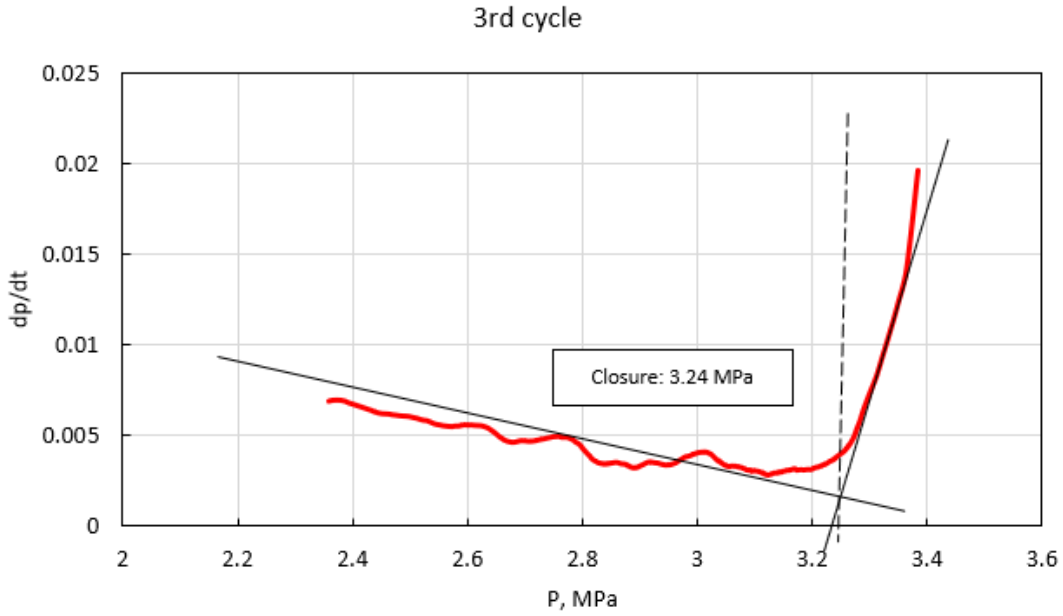

Figure 61. Pressure decay rate plot for the 3rd DFIT cycle at 151 m

4.2.3.7 Re-Opening Pressure

After the first DFIT cycle, the slope of the subsequent pressure build-ups in the 2nd, 3rd and 4th cycles should be constant until fracture opens. Departure from the linear pressure build-up trend can be represented by the leak-off points shown in Figures 62-64. Comparing to the previous estimates for the FCP, the values estimated from the re-opening pressure method are significantly larger. Therefore, results from this method are considered as upper limit estimates for the fracture closure pressure and used to guide the analysis for the other methods. Additionally, the interpretation procedure in this method can be subjective, since in most cases, there are not enough data points in the pressure build-up period, the change in slopes is not sufficiently obvious.

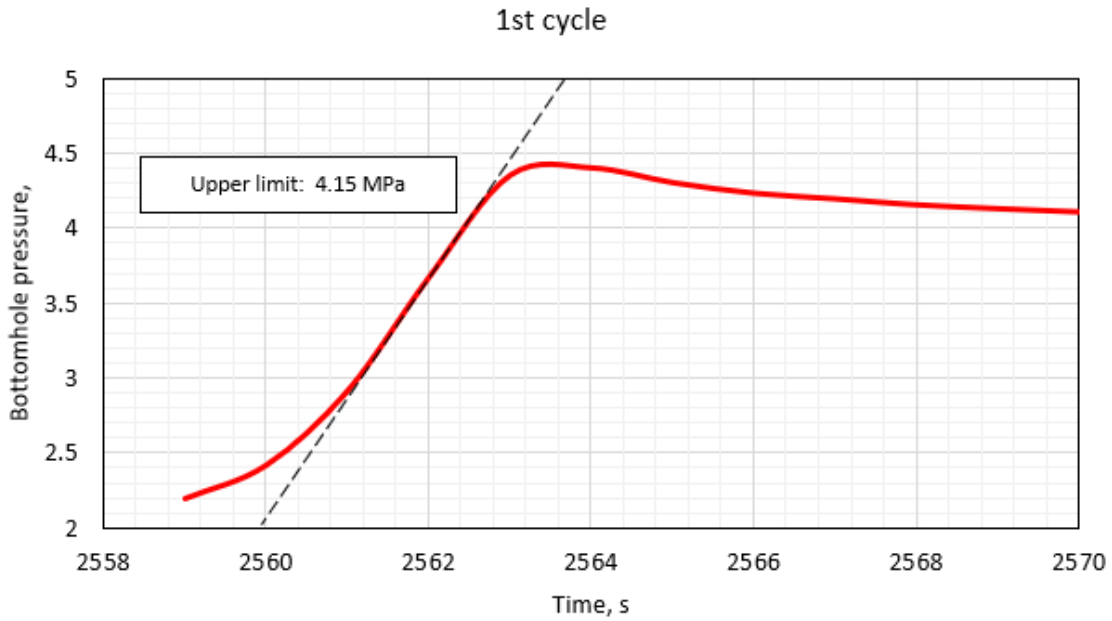

Figure 62. Reopening plot for the 1st DFIT cycle at 151 m

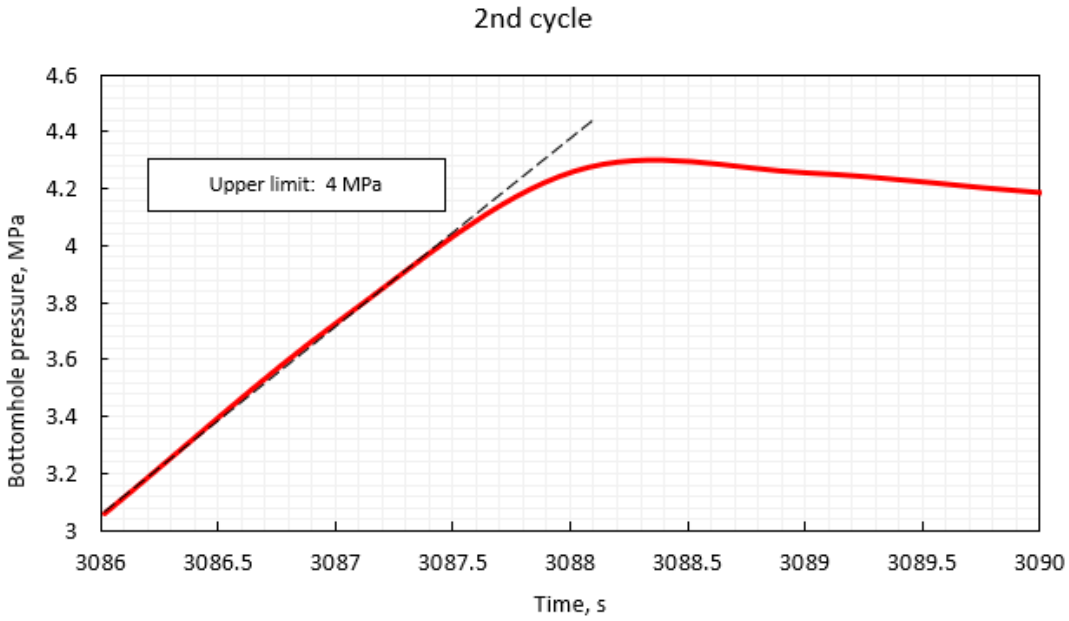

Figure 63. Reopening plot for the 2nd DFIT cycle at 151 m

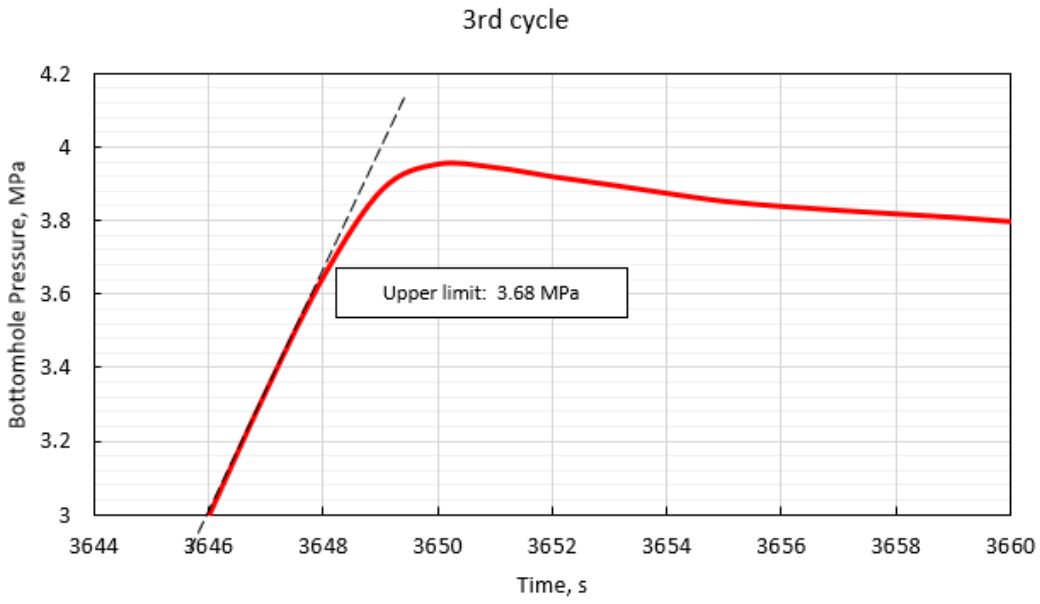

Figure 64. Reopening plot for the 3rd DFIT cycle at 151 m

Based on all seven interpretation methods, the closure pressure predictions from the DFIT test conducted at 151 m depth in the Clearwater Formation are summarized in Table 11. From the first

three method, the lower and upper limits of the closure pressure (minimum in-situ stress) can be estimated which may represent the start and end of the fracture closure period and range from 2.7 MPa to 3.16 MPa. Upper limit values determined from re-opening pressure method are not used in estimating the final closure pressure. As well, pressure at the start of the closure period was not used. Assuming equal applicability of the remaining interpretation methodologies and using values underlined in Table 11, the final closure pressure for the Clearwater Formation at a depth of 151m is determined as 2.88 MPa.

Table 11. DFIT interpretation results at 151 m

Method of interpretation	Closure Pressure (MPa)		
	First cycle	Second cycle	Third cycle
G-function	3.1 / 2.7	3.1 / 2.75	3
Square root of time	3.14 / 2.7	3.15	3.12
DT Log – Log derivative	3.07 / 2.7	3.1	3.08
Bachman's method	3.16	3.15	3.07
Horner's plot	2.9	2.88	2.9
Bilinear Pressure decay rate	3.17	3.23	3.24
Re-opening pressure (Upper limit)	4.15	4	3.68

Following the same methodology, estimations of the closure pressure from the other three DFIT tests are summarized in Tables 12-14. Analysis of these DFIT tests using the same interpretation techniques yields values of 3.11 MPa, 3.65 MPa and 4.92 MPa for 171 m, 207 m and 232 m depths, respectively.

Table 12. DFIT interpretation results at 171 m

Method of interpretation	First cycle	Second cycle	Third cycle
	Closure pressure (MPa)		
G-function	3.38 / 2.83	3.34 / 2.7	3.33
Square root of time	3.34 / 2.87	3.33	3.32
DT Log – Log derivative	3.37 / 2.9	3.33/2.6	3.26
Bachman's method	3.33	3.29	3.23
Horner's plot	3.18	3.20	3.18
Bilinear Pressure decay rate	3.5	3.5	3.46
Re-opening pressure (Upper limit)	4.5	4.1	4.2

Table 13. DFIT interpretation results at 207 m

Method of interpretation	First cycle	Second cycle	Third cycle
	Closure pressure (MPa)		
G-function	4.4 / 3.6	3.5	-
Square root of time	4.7 / 3.51	3.48	
DT Log – Log derivative	4.55 / 3.8	-	
Bachman's method	3.64	-	
Horner's plot	3.9	3.75	
Bilinear Pressure decay rate	-		
Re-opening pressure (Upper limit)	4.6	4.3	-

Table 14. DFIT interpretation results at 232 m

Method of interpretation	First cycle	Second cycle	Third cycle
	Closure pressure (MPa)		
G-function	4.79	4.92	4.8
Square root of time	-		
DT Log – Log derivative	5 / 4.9	5.2 / 4.95	5.27 / 5.07
Bachman's method	5	5.1	5.1
Horner's plot	4.8	4.8	4.85
Bilinear Pressure decay rate	5.1	-	
Re-opening pressure (Upper limit)	-	5.1	5.11

DFIT's provide an estimate of the minimum principal in-situ stress which can be the vertical stress so it is important to differentiate between vertical and horizontal stresses. Based solely on formation density estimation, the in-situ vertical stresses at the depths of the DFIT tests are computed to be 3.16 MPa, 3.60 MPa, 4.35 MPa and 4.86 MPa for 151 m, 171 m, 207 m and 232 m depths, respectively. If σ_{hmin} was indeed the minimum, the minimum stress result should a yield value lower than the vertical stress. This condition is met for depths of 151m, 171m and 207m where the estimated fracture closure pressure is clearly lower than the overburden stress. However, at the depth of 232 m, the minimum stress predicted is nearly identical to the vertical stress. This likely means that at 232 m depth, σ_v is the minimum in situ principal stress.

Table 15 Summary of predicted closure pressures with a range

Depth (m)	Lower value (MPa)	Higher value (MPa)	Closure pressure (MPa)	σ_v (MPa)
151	2.70	3.16	2.89 ± .18	3.16
171	2.83	3.33	3.11 ± .19	3.60
207	3.48	3.90	3.65 ± .16	4.35
232	4.79	5.10	4.92 ± .12	4.86

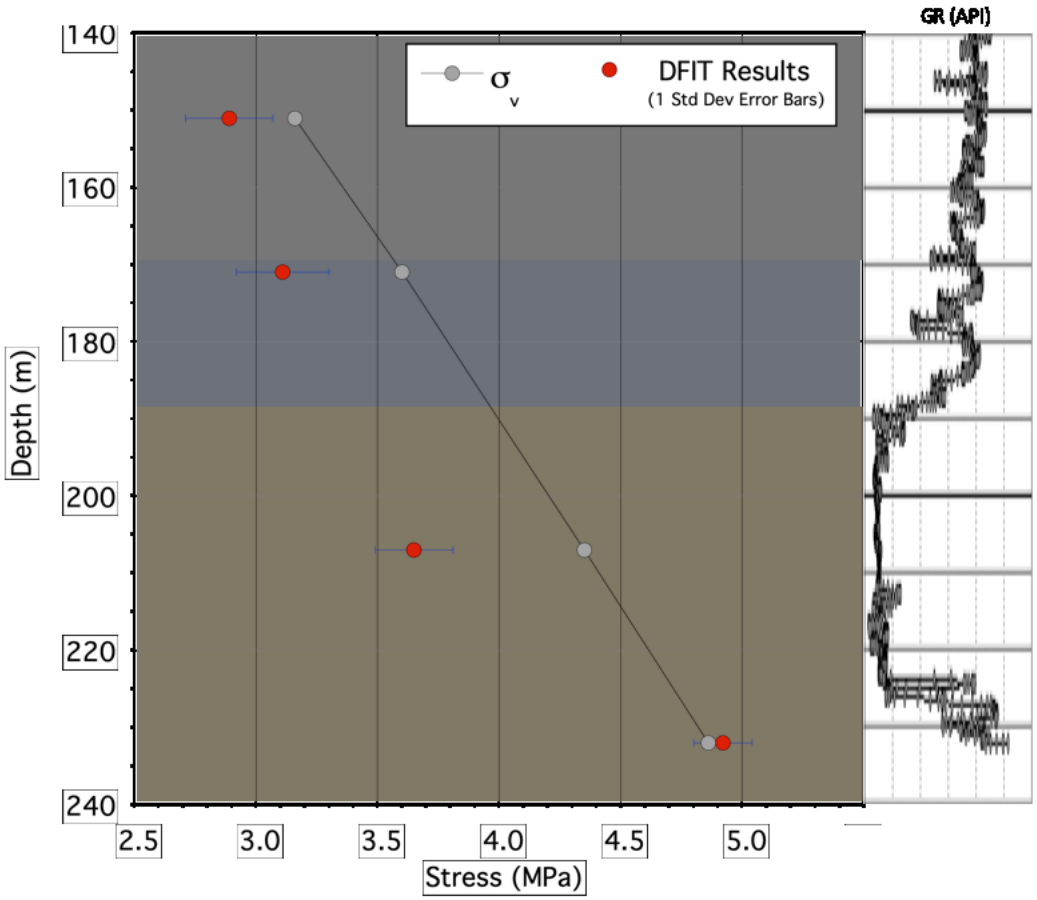

Figure 65. Comparison between closure pressure and the overburden stress

4.2.4 Discussion and Conclusions

DFIT data of four tests from different depth was analyzed and discussed. The results are interpreted by methods not only commonly used in the industry but also relative novel ones. Besides, multiple cycles were selected to help to give more accurate closure pressures. Comparisons between each interpretation method for four depth are summarized in Figure 66-69.

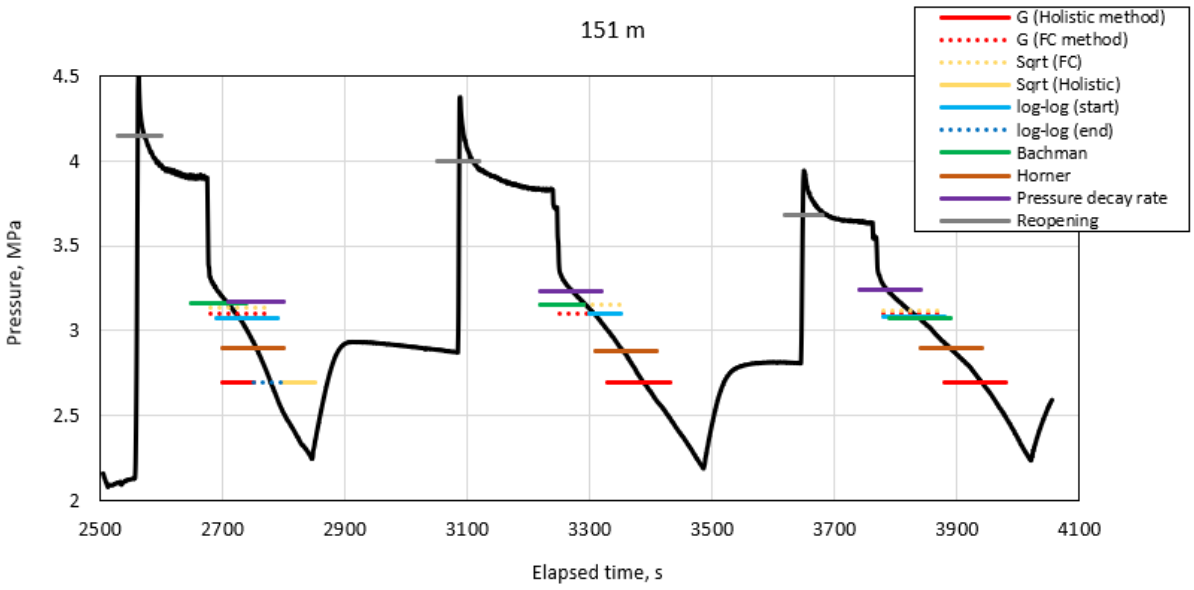

Figure 66. Pressure history during DFIT and interpretation methods at 151 m depth

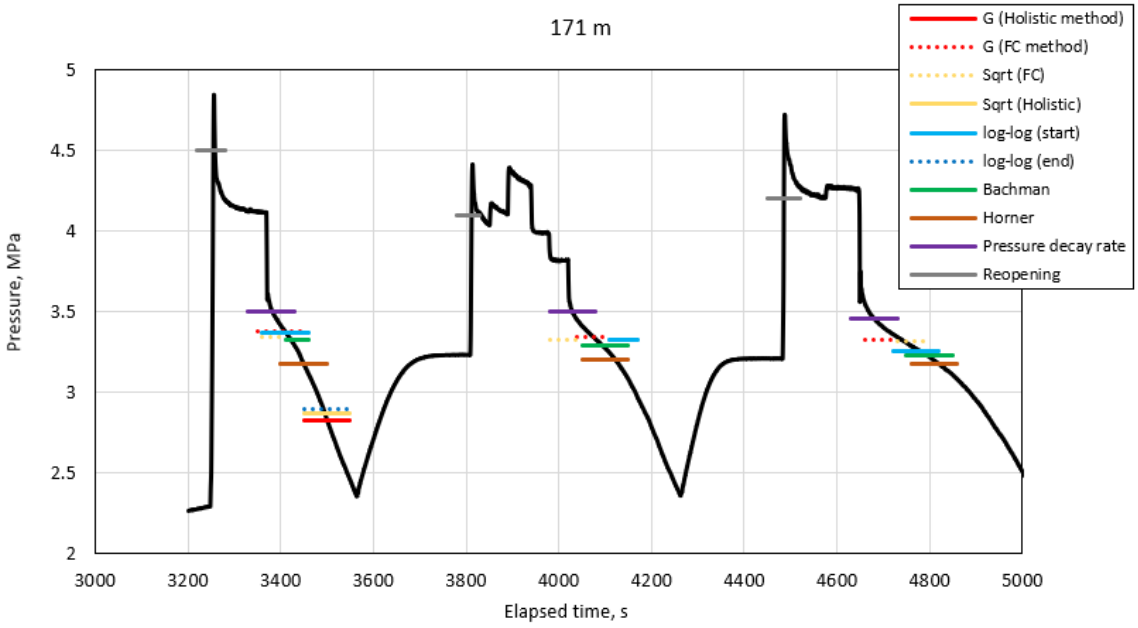

Figure 67. Pressure history during DFIT and interpretation methods at 171 m depth

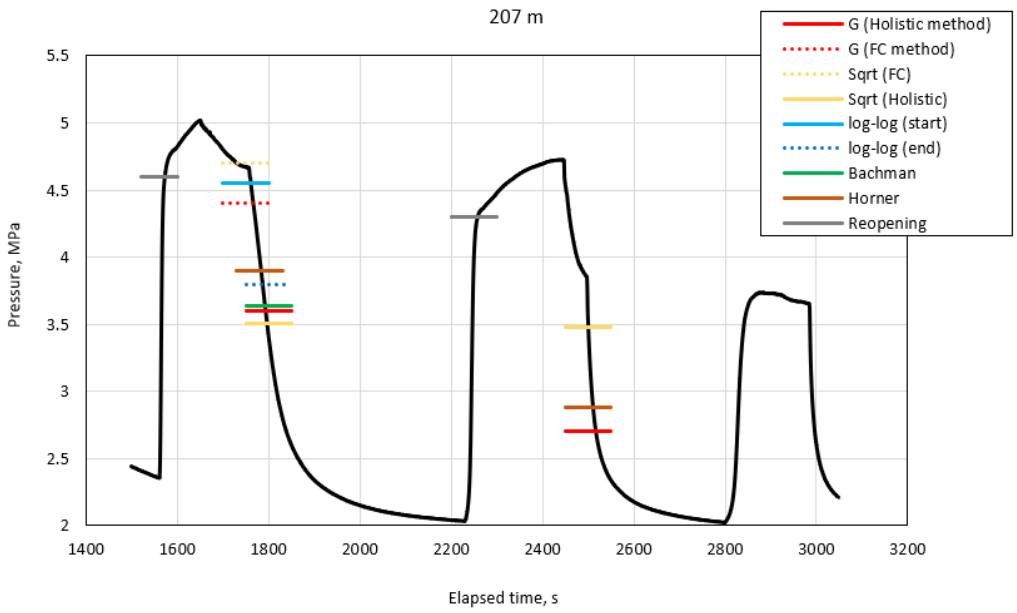

Figure 68. Pressure history during DFIT and interpretation methods at 207 m depth

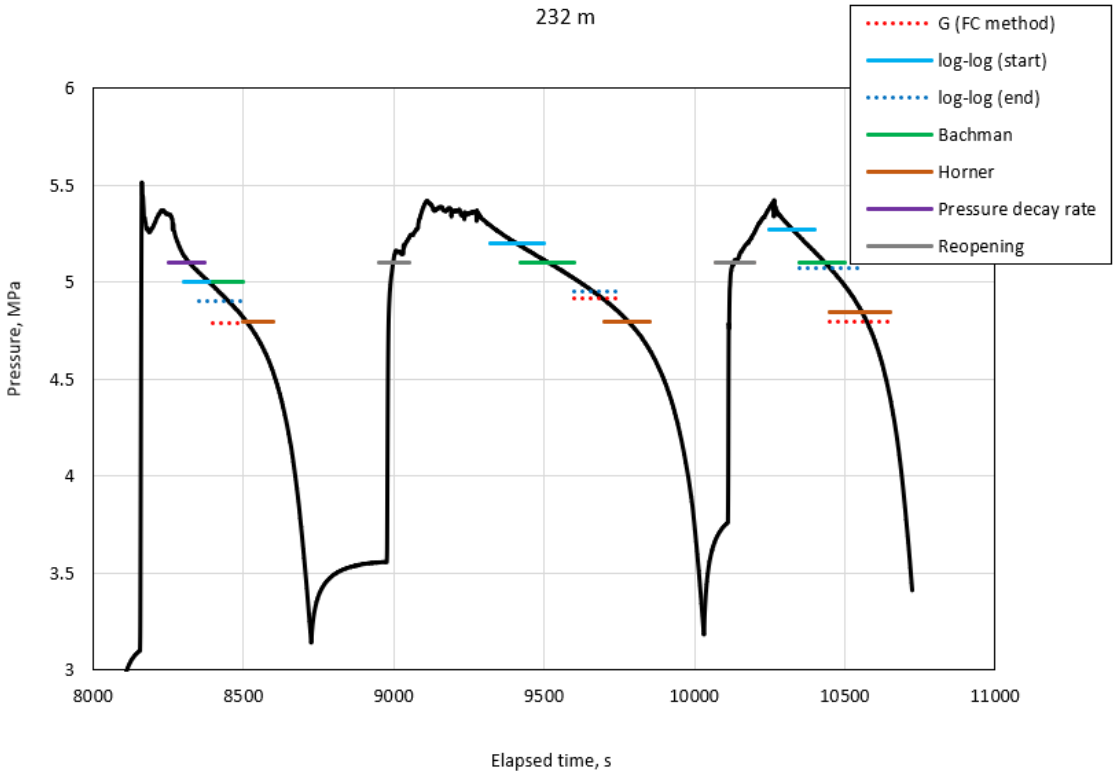

Figure 69. Pressure history during DFIT and interpretation methods at 232 m depth

Fracture closure is not an instantaneous event but a short duration process with a start and end. The log-log derivative method along with the PPD technique can successfully interpret the start and end of closure. It clearly explains the dominated flow regimes before and after closure (if the data is perfect) and the closing duration. Two methods were used in the G-function and square root of time plots. The fracture compliance method was proposed especially for low permeability reservoirs by Cramer (2015). It is noted that the closure selected by the fracture compliance method occurs much sooner and the pressure is higher than the holistic method in G Function and Square Root of time plots. By comparing with the log-log derivatives and PPD, fracture compliance results have a similar fracture closure value as pressure at the start of closure while the holistic method yielded consistent values with the pressure at end of the closure. So it may be possible that the two methods also constrain the start and end of the closure. The Bilinear and Bachman's method tend to give high closure pressure close to the start of closure. The final minimum in-situ stress is given with a range and average value for each depth. In caprock integrity problem such as SAGD operation, we prefer avoiding the open of tensile fractures and natural fissures that allow the steam to escape from the reservoir. To be conservative, a lower minimum in-situ stress is needed. On the contrary, if the caprock is relatively intact, a higher value may be preferred from a production and economics point of view. Based on the results in this research, the combination of G-function, square root of time and the log-log derivative method appear to predict consistent fracture closure pressure estimates.

4.3 Maximum Horizontal Stress

Several methods exist to estimate σ_H using hydraulic fracture or mini-frac test results. The maximum horizontal stress can be estimated by the stability analysis equation [9] – [12] when a hydraulic fracture is induced (Zoback 2007). At the point of minimum compression, a hydraulic

fracture will be induced when the tangential stress around the borehole exceeds the tensile stress of the formation materials. Assuming σ_h and material tensile strength have been determined, σ_H can be inverted through those equations. A major limitation with this method is that it is essentially impossible to detect fracture initiation during the pressurization stages of the mini-frac test. Another method utilizes the geometry of borehole breakouts to constrain σ_H as breakout width is a function of both σ_H and rock strength (Zoback 2007). For these two methodologies, the corresponding wellbore failure induced fracture or breakout must be observed in the well in order to constrain the magnitude of horizontal stresses but this does not happen in all wells and is the case for Well 8-29 used in this research. To overcome these limitations, numerical methods are adopted in this research to invert the caliper measured borehole wall displacements to the corresponding in situ stress field. Three-dimensional modelling software FLAC3D was used to simulate the wellbore deformation at different depths. By matching the wellbore displacement from simulation results to the oriented caliper data, the maximum horizontal stress was estimated.

4.3.1 Model Geometry

In FLAC3D, a quarter of the wellbore section was generated with the dimension 1000 mm x 1000 mm x 16 mm. A borehole was numerically drilled in the lower left corner with a radius of 79.5 mm. Because stress concentration and wellbore breakouts were expected to occur in the near wellbore region, a mesh geometric ratio 1.1 or higher with the maximum side length of a zone less than 2.0% of the borehole radius was utilized in the vicinity the area of wellbore wall. Walton and Diederichs (2015) suggested that this zonation size is dense enough to capture the failure mechanics while avoiding any mesh dependency effects. Elements with larger size are used for the region far away from the wellbore (Figure 70).

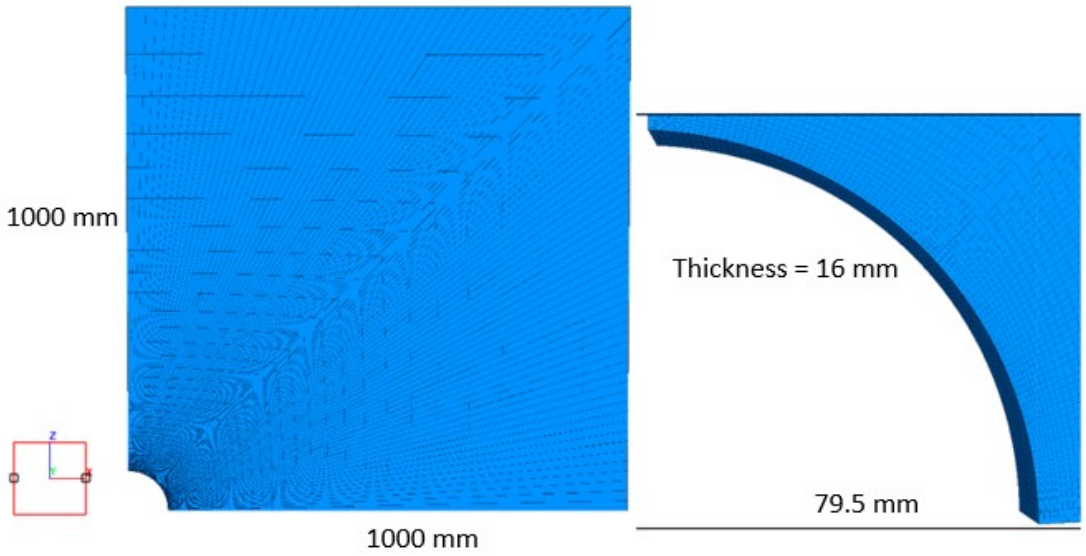

Figure 70. Geomechanical model for wellbore deformation simulation and a zoomed-in section

4.3.2 Boundary conditions

The boundary conditions for the plane stress model are illustrated in Figure 71. Roller boundaries are specified along the two axes of symmetry and the minimum and maximum horizontal stresses are applied to the other boundaries. The vertical or overburden stress is applied in the direction perpendicular to the model. The constitutive behavior generated in Chapter 3 was adopted for simulations in the Clearwater and Wabiskaw Formations. No simulations were conducted for the McMurray Formation.

Three steps were used to simulate wellbore deformation in this study:

1. a geostatic step to establish the initial stress conditions and ensure stress equilibrium within the model. The vertical stress at a particular depth is established using formation density, the minimum horizontal stress is set by the DFIT interpretations and the maximum

horizontal stress is varied to enable history matching to the caliper measured borehole deformation;

2. a borehole drilling step where elements representing the borehole were removed and a normal pressure applied to the borehole wall to simulate support provided by drilling mud which is the integration pressure of fluid column in the wellbore; and
3. a wellbore deformation step to model the unloading of the borehole wall.

As unloading occurred, if the zones on the borehole wall underwent compression failures, it was assumed these zones would be washed out by the drilling fluid creating the "breakout" zone. Therefore, once a grid block yielded, it would be "nulled" (removed) from the whole model as a way to imitate the generation process of the wellbore breakout.

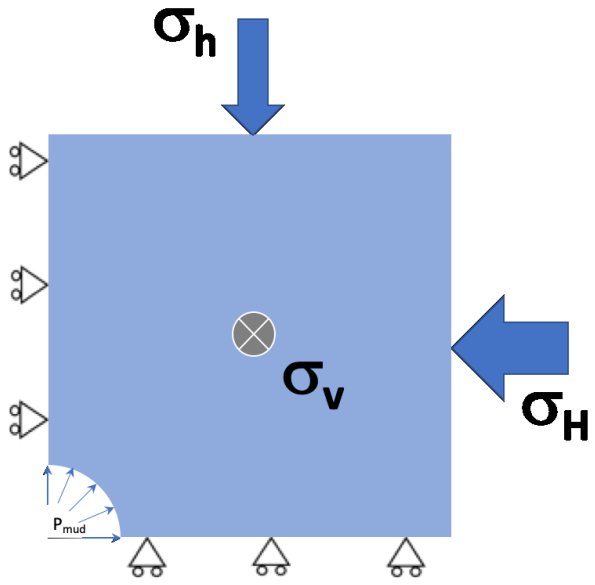

Figure 71. Boundary conditions of the wellbore section model

4.3.3 Discussion

Variations in the maximum horizontal stress (σ_H), will produce borehole wall "elongation" in the direction of σ_h. Figure 72(a) shows the one example of the simulation results of wellbore deformation at 151 m depth where under the chosen value of σ_H , five gridblocks have yielded in the direction of σ_h , indicating a breakout depth of 3.43mm. Systematic variation of σ_H in the simulations allows the modelling to match the deformations in the C1-C4 direction of the oriented caliper log measurements, as shown in Figure 72(b), which is 3.37 mm. As shown in Table 16, a value of σ_H needs to be determined that will match the caliper measured C1-C4 deformation of 3.37 mm. For the 151 m depth, robustness in the history match would have been improved by also attempting to match the deformation in the C2-C5 and C3-C6 directions. But unfortunately, at some depths, the compression displacements are too large to match by the simulation procedure and did not allow for this additional simulation step. These excessive compression displacements are caused by tool eccentricity along with other caliper measurement errors.

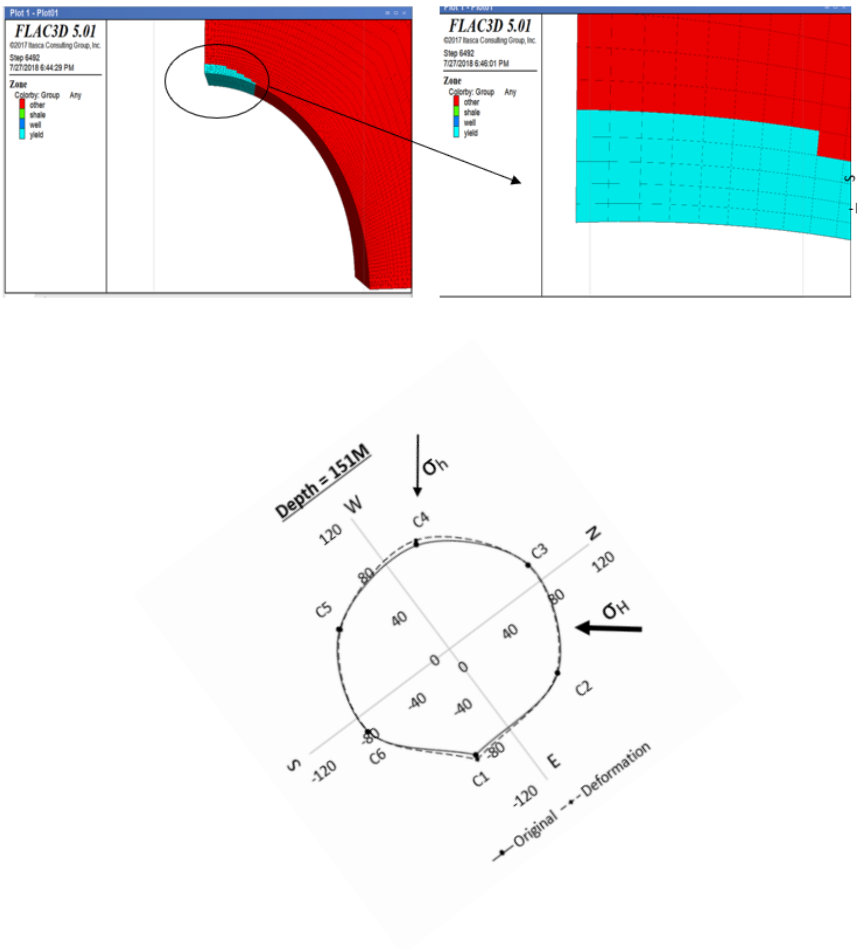

Figure 72. a) Simulation result plots and b) caliper measured deformed shape at 151 m depth in Clearwater Formation

Table 16. Distorted caliper data at 151 m depth

Depth 151 m	C1-C4	C2-C5	C3-C6
Diameter (mm)	165.75	156.98	158.40
Radius (mm)	82.88	78.49	79.20
Bit radius (mm)	79.5		
Δ (mm)	3.37	-1.00	-0.29

The maximum horizontal stresses determined from the history matching simulations conducted for the DFIT test depths of 151 m and 171 m are shown in Table 17. For the remainder of the depths for which horizontal stresses are reported in Table 17, a modification to the simulation history matching process was required. This is due to the fact that where there was no DFIT conducted, σ_h is an unknown and can't be set as a known value for the simulations. In order to match the caliper data at these other depths, both the minimum and maximum horizontal stress need to change during the simulation which leads to a non-unique solution. To overcome this limitation, the horizontal stress ratio (σ_H / σ_h) established for the Clearwater Formation (1.38 at 151 m depth) and the Wabiskaw Member (1.375 at 171 m depth) was assumed to be applicable for each zone. Figure 73 shows the final stress profiles along the observation well for the Clearwater Shale and Wabiskaw Member.

Results show decent applicability and good consistency between different depths. The stress gradient for the overburden stress, the minimum and maximum horizontal stresses for these two formations are 21.5 kPa/m, 18.7 kPa/m and 25.8 kPa/m, respectively. These stress gradients are indicative of a strike-slip faulting regime. Uncertainty still remains for the stress measurement at a depth of 232 m where its interpreted value of 4.9 MPa is essentially equal to the vertical overburden stress of 4.86 MPa. Further analyses are required to fully explain this phenomenon.

Table 17. Results of the stress profile along Well 8-29

Depth (m)	σ_H	σ_h	σ_H/σ_h	
115.375	3.27	2.37	1.38	Clearwater Formation
127.5	3.5	2.53	1.38	
130.5	3.53	2.55	1.38	
148.5	3.93	2.84	1.38	
151	3.98	2.88	1.38	
163	4.13	2.99	1.38	
171	4.4	3.2	1.375	Wabiskaw member
185	4.6	3.35	1.375	
196	4.75	3.45	1.375	
199	4.8	3.49	1.375	
208	5.08	3.7	1.375	

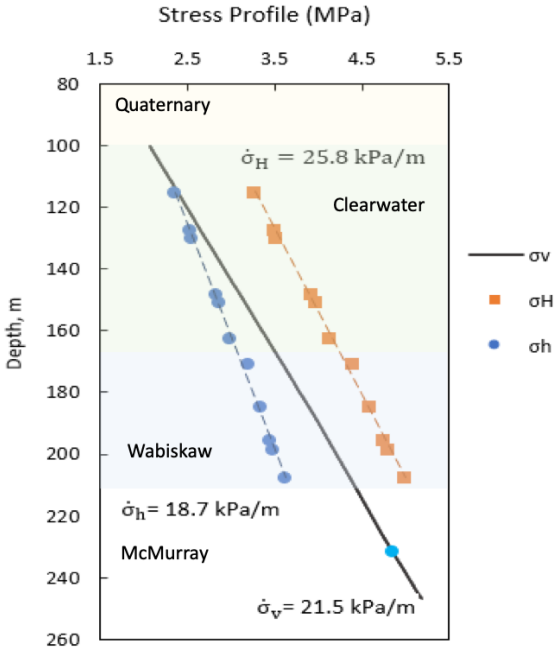

Figure 73. Results of the stress profile along Well 8-29

Results are also compared with work done by other researchers. The three oilsands regions in Figure 74 are located within the Athabasca oilsands area. The range of the minimum horizontal stress gradient between 18 – 23 kPa/m obtained for this region based on micro-frac testing is consistent with the estimates provided in this research. Figure 75 shows a well location from the Grizzly project (Big Guns Energy Services, 2013) within the Leismer field area, which is approximately 10 km northwest of Conklin, AB. Well 8-18-77-8W4 is located significantly south of Well 8-29, but a series of mini-frac tests were conducted in the same Clearwater Formation. The stress gradient of the minimum horizontal stress obtained in this Grizzly project varies between 15.3 – 18.3 kPa/m which is a little bit lower than stress gradients in this research but still within accepted range. Figure 76 summarizes the results from this research as well as others and shows the stress gradients with depth.

Figure 74. Locations of stress magnitude measurements in the Western Canada Sedimentary Basin (Bell 1990)

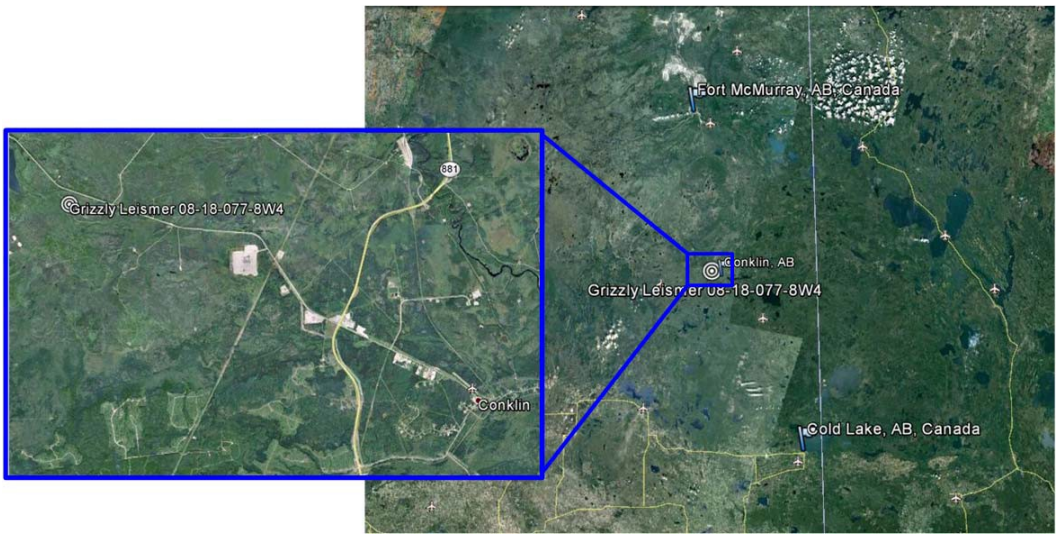

Figure 75. Location of well 08-18-077-08W4 (Big Guns Energy Services, 2013)

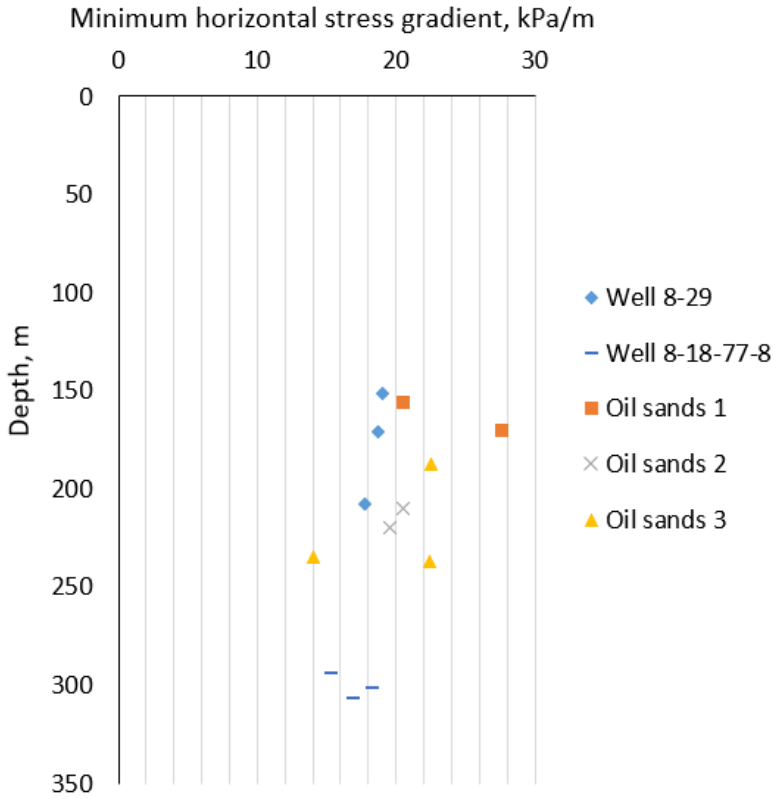

Figure 76. Results of stress gradients from different sources

5 Conclusions

5.1 Summary and Conclusions

Caprock integrity is a big issue in the SAGD thermal recovery process where pressurized steam must be reside safely within the reservoir. Excessive and higher pressure will fracture the caprock and release the steam into the caprock. To limit the maximum operation pressure, a requisite is knowing the in-situ stress and the caprock geomechanical properties. This research proposed an integrated method to assess the in-situ stress state along an observation well using lab and field data.

- Chapter 3 was a detailed analysis of laboratory test results of samples from Clearwater and Wabiskaw Formations. Two strain hardening/softening constitutive models and associated parameters were generated and calibrated for further numerical studies. For Clearwater Formation, Sample 2 was excluded from the strength calibration due to an anomalously low strength. Tangent Young's modulus was determined and increases with increasing confining stress described by a logarithm trend. However, the confining pressure did not affect the Poisson's ratio. Based on Mohr's Circles analysis, the effective cohesion was 0.7 MPa and the effective angle of friction is 21˚. Only Sample 1 and 4 have been used to estimate Poisson's ratio and dilation angle. A nonlinear cohesion weakening friction strengthening (CWFS) model was employed to parameters variations. A Poisson's ratio of 0.33 was determined and the variation of dilation angle was also described. In general, the simulation results and laboratory observations for Clearwater Formation show good visual match. However, less credit is giving to the volumetric prediction due to the poor quality of data. For Wabiskaw Formation, a linear trendline was used to describe the increasing Young's modulus with increasing confining stress. The effective cohesion and friction

angle were 0.13 MPa and 33°, respectively. A Poisson's ratio was determined as 0.36. The matches between strength curves for Wabiskaw Formation are not as consistency as those for Clearwater Formation, however, the volumetric behaviors were better matched and more detailly described.

- Chapter 4 summarized the determination of three principal in-situ stresses. The overburden stress was simply estimated by integration of the overburden weight at certain depth. Borehole images were used, and caliper log data were calibrated (using different methods for different borehole conditions) to determine the direction of σ_h. Variation in stress orientation with depth was observed. In the upper strata between 50 to 100 m σ_h is aligned in the N-S direction. In the strata of caprock and reservoir between100 to 240 m, the direction changes to E-W. Local geological features had very likely altered the local stress orientation. Then, DFIT data conducted on field was interpreted using several PTA types analyses to estimate the minimum component of the in-situ principal stress. Three cycles were selected from each test to help give more accurate closure pressures. Fracture closure event is a duration process with a start and end. The log-log derivative method combined with PPD curve can successfully give the start and end of closure. Results show that multiple interpretation methods are need and a combination of G-function, square root of time and log-log derivative method is enough to give a consistent prediction. Incorrect estimation can be result from wellbore storage, aperture recession and data fluctuation.
- Lastly, a numerical method has been used to invert for the maximum horizontal stress of the caprock. Previous results and geophysical log data of several depth intervals were selected for simulations in FLAC3D. By history matching the oriented borehole shape from calibrated caliper data, a series of maximum horizontal stresses can be determined.

Results show that for the caprock formations along well 8-29, the local faulting regime is strike-slip fault and the horizontal stress is in a range between 2.37 to 3.7 MPa for the minimum horizontal stress and 3.27 to 5.08 MPa for the maximum horizontal stress. The minimum and maximum horizontal stress gradients are estimated as 18.7 and 25.8 kPa/m. Stress gradients of the minimum horizontal stress results have been compared with work done by others in nearby locations and show consistency within reasonable range. Stress magnitudes of the maximum horizontal stress remains uncertainties because of a lack of contrast and confirmation.

5.2 Recommendations for Further Research

Determining accurate geomechanical properties are extremely essential for caprock integrity analysis. To describe the behavior of caprock materials from Clearwater Formation, it is necessary to have valid volumetric curves. The lack of valid volumetric data will lead to a misdescription of the volumetric behavior of caprock materials, which can create uncertainties to caprock integrity problems. For Wabiskaw samples, triaxial tests data under in-situ confinement conditions are necessary. Confining stresses from the provided triaxial tests data for Wabiskaw samples are between 0.1 to 1 MPa and the determined parameters are only applicable in this stress range. However, in following simulations of wellbore deformation, the constitutive model for Wabiskaw Formation was subjected to in situ confinement as large as 2 – 4 MPa. The generated geomechanical parameters are no longer suitable. Those parameters need to be calibrated in a reasonable stress range. Additionally, the variations of cohesion and friction angles need to be smoothed.

The proposed method in this research highly relies on the quality of the measurement data. The changes of the oriented caliper data from in gauge borehole are so small that can possibly be

considered as measuring error of decentralization. More work should be conducted on the wellbore deformation simulations using more oriented caliper data from different depths to preclude the influence of decentralization. It is better to have additional data (borehole images and caliper data) from adjacent wells to make consistent and reliable conclusions of stress orientation and magnitude.

The numerical method was only applied to and suitable for normal and strike-slip fault regimes where the minimum horizontal stress is the minimum in-situ stress. In the reverse fault regime, the overburden stress becomes the minimum component of the three in situ principal stresses. Consequently, DFIT or mini-frac tests data will no longer be used to estimate σ_h. A 3-dimentional model of a depth interval may required to simulate the mini-frac test. The magnitude of horizontal stresses may affect the pressure drop rate or leak off efficiency. In this case, the magnitude of horizontal stresses can be determined by history matching the pressure curve from mini-frac tests. For this purpose, the properties of the created fracture such as stiffness and aperture need to be fully understood in advance.

6 Reference

Aadnoy, B.S., Bell, J.S., 1998. Classification of drilling induced fractures and their relationship to in situ stress directions. The Log Analyst, pp. 27–42.

Addis M.A., Last N.C., Yassir N.A. 1996. Estimation of horizontal stresses at depth in faulted regions and their relationship to pore pressure variations. SPE Formation Evaluation J., 11-18, March. SPE-28140-MS.

Alberta, Employment, Immigration and Industry. December. Alberta Oil Sands Industry Updat (PDF). Government of Alberta. Archived (PDF) from the original on 2008-04-09.

Anderson, E. M. 1951. The dynamics of faulting and dyke formation with applications to Britain. Edinburgh and London, Oliver and Boyd, 2d ed.

Bachman, R.C., Walters, D.A., Hawkes, R.A.et al. 2012. Reappraisal of the G Time Concept in Mini-Frac Analysis. Paper presented at the SPE Annual Technical Conference and Exhibition, San Antonio, Texas, 8-10 October. SPE-160169-MS.

Bachman, R.C., Afsahi, B., and Walters, D. 2015. Mini-Frac Analysis in Oilsands and their Associated Cap Rocks Using PTA Based Techniques. Paper presented at the SPE Canada Heavy Oil Technical Conference, Calgary, Alberta, Canada, 9-11 June. SPE-174454-MS.

Barree, R.D. 1998. Applications of Pre-Frac Injection/Falloff Tests in Fissured Reservoirs - Field Examples. Paper presented at the SPE Rocky Mountain Regional/Low-Permeability Reservoirs Symposium, Denver, Colorado. Society of Petroleum Engineers. SPE-39932-MS.

Barree, R.D., Mukherjee, H. 1996. Determination of Pressure Dependent Leakoff and Its Effects on Fracture Geometry. Paper presented at the 1996 Annual Technical Conference and Exhibition, Denver, CO, Oct. 6-9. SPE-36424-MS.

Barree, R.D., Barree, V.L. and Craig, D.P. 2007. Holistic Fracture Diagnostics. Paper presented at the SPE Rocky Mountain Technical Symposium, Denver, 16-18 April. SPE-107877-MS.

Barree, R.D., Barree, V.L., and Craig, D. 2009. Holistic Fracture Diagnostics: Consistent Interpretation of Pre-frac Injection Tests Using Multiple Analysis Methods. Paper SPE Production & Operations 24 (3), 396–406.

Barton, C. A., Moos, D., PESKA, P. & ZOBACK, M. D. 1997. Utilizing wellbore image data to determine the complete stress tensor: application to permeability anisotropy and wellbore stability. The Log Analyst, 38(6), 21-33.

Bell, J. S. 1990. Investigating stress regimes in sedimentary basins using information from the oil industry wireline logs and drilling records. Geol. Soc. London, Spec. Publ. 48, 305–325.

Bell, J. S. and Gough, D. I. 1979. Northeast-Southwest Compressive Stress in Alberta: Evidence from Oil Wells. Earth Planet. Sci. Lett., 45, 475-482.

Bell, J. S., Price, P. R., and McLellan, P. J. 1994. In-situ stress in the western Canada Sedimentary Basin. In Geological atlas of the western Canada sedimentary Basin. Mossop, G.D., Shetsen, I: Canadian Society of Petroleum Geologists and Alberta Research Council, 439 – 446.

Berkowitz, N., & Speight, J. G. 1975. The oil sands of Alberta. Fuel, 54(3), 138-149.

Big Guns Energy Services. 2013. Mini-frac Analysis Report.

Bourdet, D.P., Whittle, T.M., Douglas, A.A. and Pirard, Y.M. 1983. A New Set of Type Curves Simplifies Well Test Analysis, World Oil, May.

Brudy, M., and Kjørholt. H. 2001. Stress orientation on the Norwegian continental shelf derived from borehole failures observed in high- resolution borehole imaging logs: Tectonophysics, 337, 65-84.

Camac, B., Hunt, S.P. and Boult, P. 2004. Applications of stress field modelling using the distinct element method for petroleum production. Paper presented at Asia Pacific Oil and Gas Conference and Exhibition Perth, 18-20 October 2004. SPE-88473-MS.

Chai, J. C., Carter, J. P., & Hayashi, S. 2007. Modelling strain-softening behaviour of clayey soils. Lowland Technology International, 9(2), 29-37.

Chatterjee, R. Mukhopadhyay, M. 2003. Numerical modelling of stress around a wellbore. Paper presented at SPE Asia Pacific Oil and Gas Conference and Exhibition, Jakarta, Indonesia, 9-11 September. SPE-80489-MS

Cheng, Z. & Detournay, C. 2016. Plastic hardening model I: Implementation in FLAC3D. In Proc. 4th Itasca Symposium on Applied Numerical Modeling, Lima, Peru, 7-9 March.

Craig, D. P., Odegard, C. E., Pearson Jr, W. C., & Schroeder, J. E. 2000. Case History: Observations from Diagnostic Injection Tests in Multiple Pay Sands of the Mamm Creek Field, Piceance Basin, Colorado. Paper presented at SPE Rocky Mountain Regional/Low-Permeability Reservoirs Symposium and Exhibition, Denver, CO, 12-15 March. SPE-60321-MS

Cramer, D. 2015. Reexamining DFIT Interpretation Methods. SPE Gulf Coast Section Completions & Production Study Group Luncheon.

Dart, R.L. 1989. In situ stress analysis of wellbore breakouts from Oklahoma and the Texas Panhandle, in K. S. Johnson, ed., 1988 Anadarko Basin Symposium: Oklahoma Geological Survey Circular 90, p. 97–120.

Duan, K., Kwok, C. Y. 2016. Evolution of stress-induced borehole breakout in inherently anisotropic rock: Insights from discrete element modeling. Journal of Geophysical Research: Solid Earth, 121(4), 2361-2381.

Eckert, A., Liu, X. 2014. An improved method for numerically modeling the minimum horizontal stress magnitude in extensional stress regimes. Int. J. Rock Mech. Min. Sci. 9(70), 581–592.

Ekstrom, M., Dahan, C., Chen, M., Lloyd, P., Rossi, D. 1987. Formation imaging with microelectrical scanning arrays. Log Anal. 28 (3), 294-306.

Energy, S. 2014. Suncor MacKay River Project 2014 AER Performance Presentation: Subsurface (Approval No. 8668). Suncor Energy, Calgary.

Fjar, E., Holt, R. M., Raaen, A. M., Risnes, R., & Horsrud, P. 2008. Petroleum related rock mechanics (Vol. 53). Elsevier.

Glass, D.J. 1990. Lexicon of Canadian stratigraphy, Volume 4, Western Canada, Including Eastern British Columbia, Alberta, Saskatchewan and Southern Manitoba. Canadian Society of Petroleum Geologists, Calgary, Alberta, 772p.

Gronseth, J. M. (1989 January. Geomechanics Monitoring of Cyclic Steam Stimulation Operations in the Clearwater Formation. IS-1989-166 in ISRM International Symposium. International Society for Rock Mechanics and Rock Engineering, France, 28-31, August.

Haimson, B C, and M.Y. LEE. 1989. "Stress Measurement Parameters." 26(6): 447–56.

Hawkes, R.V., Anderson, I., Bachman, R.C., and Settari, A. 2013. Interpretation of Closure Pressure in the Montney Shale using PTA Techniques. Paper presented at the Hydraulic Fracturing Conference, The Woodlands, 4-6 February. SPE-163825-MS.

Horner, D. R. 1951. Pressure build-up in wells. In 3rd world petroleum congress. World Petroleum Congress, The Hague, the Netherlands.

Huber, K., Fuchs, K., Palmer, J., et al. 1997. Analysis of borehole televiewer measurements in the Vorotilov drillhole, Russia—first results. Tectonophysics, 275(1-3), 261-272.

Idowu, O. A., & Schmidtt, D. A. 2011. Updating the Tectonic Stress Map of Alberta Using Borehole Breakout Method. In Recovery–2011 CSPG CSEG CWLS Convention.

Ienaga, M., McNeill, L. C., Mikada, H., Saito, S., Goldberg, D., & Moore, J. C. 2006. Borehole image analysis of the Nankai Accretionary Wedge, ODP Leg 196: Structural and stress studies. Tectonophysics, 426(1-2), 207-220.

Jarosiński, M. 1998. Contemporary stress field distortion in the Polish part of the Western Outer Carpathians and their basement. Tectonophysics, 297(1-4), 91-119.

Kim, G. Y., & Narantsetseg, B. 2015. Fractures and Breakouts Analysis from Borehole Image Logs: Preliminary Results for Interpretation of Stress History and In Situ Stress State. Marine Georesources & Geotechnology, 33(6), 579-585.

Kirsch, C. 1898. Die theorie der elastizitat und die bedurfnisse der festigkeitslehre. Zeitschrift des Vereines Deutscher Ingenieure, 42, 797-807.

Lee, M. Y., & Haimson, B. C. 1989. Statistical evaluation of hydraulic fracturing stress measurement parameters. In International Journal of Rock Mechanics and Mining Sciences & Geomechanics Abstracts 26(6), 447-456.

LeRiche, A., Kalenchuk, K., & Diederichs, M. S. 2017. Estimation of in situ stress from borehole breakout for improved understanding of excavation overbreak in brittle anisotropic rock. ARMA-2018-434 presented at the 8th International Conference on Deep and High Stress Mining.

Li, P. 2006. Numerical simulation of the SAGD process coupled with geomechanical behaviour. Ph.D. dissertation. University of Alberta.

Li, X., El Mohtar, C. S., & Gray, K. E. 2016. Numerical modeling of borehole breakout in ductile formation considering fluid seepage and damage-induced permeability change. In 50th US Rock Mechanics/Geomechanics Symposium Held in Huston, 26-29 June.

Li, Y., Guo, Y., Zhu, W., Li, S., & Zhou, H. 2015. A modified initial in-situ Stress Inversion Method based on FLAC3D with an engineering application. Open Geosciences, 7(1) 824-835.

Liu, G., & Ehlig-Economides, C. 2016. Interpretation methodology for fracture calibration test before-closure analysis of normal and abnormal leakoff mechanisms. Paper presented at SPE Hydraulic Fracturing Technology Conference. The Woodlands, Texas. SPE-179176-MS.

Ljunggren, C., Chang, Y., Janson, T., & Christiansson, R. 2003. An overview of rock stress measurement methods. International Journal of Rock Mechanics and Mining Sciences, 40(7-8), 975-989.

Long Lake 2012 – Subsurface Performance Presentation.

Lynse, P. 1986. Determination of borehole shape by inversion of televiewer data. The Log Analyst, 27(3), 64-71.

Marongiu-Porcu, M., Ehlig-Economides, C.A., Economides, M.J., 2011. Global model for fracture fall off analysis. Paper Presented at the North American Unconventional Gas Conference and Exhibition. Society of Petroleum Engineers, The Woodlands, Texas. SPE-144028-MS.

Marongiu-Porcu, M., Retnanto, A., Economides, M. J., & Ehlig-Economides, C. 2014. Comprehensive Fracture Calibration Test Design. Paper presented at SPE Hydraulic Fracturing Technology Conference. Society of Petroleum Engineers. SPE-168634-MS.

Mather, Clive "The Oil Sands of Alberta" on YouTube, Canada Broadcasting Corporation.

Mattar, L., & Zaoral, K. 1992. The Primary Pressure Derivative (PPD) A New Diagnostic Tool in Well Test Interpretation. Journal of Canadian Petroleum Technology, 31(04).

Meng, C., Wei, L., & Yuan, R. S. C. 2014. Coupled fluid flow and geomechanics modeling for DFIT analysis in unconventional gas development. Paper presented at the International Petroleum Technology Conference, Kuala, Lumpur, 10-12 December. IPTC-18159-MS.

Mohamed, I. M., Azmy, R. M., Sayed, M. A. I., Marongiu-Porcu, M., Economides, C. 2011. Evaluation of after-closure analysis techniques for tight and shale gas formations. Paper presented at the SPE Hydraulic Fracturing Technology Conference. The Woodlands, Texas, 24-26 January. SPE-140136-MS.

Mohan, G. M., Sheorey, P. R., & Kushwaha, A. 2001. Numerical estimation of pillar strength in coal mines. International Journal of Rock Mechanics and Mining Sciences, 38(8), 1185-1192.

Naidu, R. N., Guevara, E. A., Twynam, A. J., Rueda, J. I., Dawson, W., Moses, E., & Rylance, M. 2015. Understanding Unusual Diagnostic Fracture Injection Test Results In Tight Gas Fields-A Holistic Approach To Resolving The Data. Paper presented at SPE Middle East Unconventional Resources Conference and Exhibition. SPE-172956-MS.

Nexen. 2013. Long Lake 2012 – Subsurface Performance Presentation.

Nolte, K. G. 1979. Determination of fracture parameters from fracturing pressure decline. Paper presented at the SPE Annual Technical Conference and Exhibition Las Vegas, Sept. SPE - 8341-MS.

Oldakowski, K., Sawatzky, R. P., & Alvarez, J. M. 2016. Geomechanical Properties of Clearwater Shale at Elevated Temperatures. Paper presented at Canada Heavy Oil Technical Conference. SPE-180694-MS.

Plumb, R. A., & Hickman, S. H. 1985. Stress-induced borehole elongation: A comparison between the four-arm dipmeter and the borehole televiewer in the Auburn geothermal well. Journal of Geophysical Research: Solid Earth, 90(B7), 5513-5521.

Powless, K. R. 2012. The use of pressure transient analysis tools to interpret mini-frac data in alberta oilsands caprocks. Paper presented at the SPE Heavy Oil Conference Canada. SPE-157843-MS.

Prensky, S. E. 1999. Advances in borehole imaging technology and applications. Geological Society, London, Special Publications, 159(1), 1-43.

Prusek, S., & Bock, S. 2008. Assessment of rock mass stresses and deformations around mine workings based on three-dimensional numerical modelling. Archives of Mining Sciences, 53(3), 349-360.

Reinecker, J., Tingay, M., & Müller, B. 2003. Borehole breakout analysis from four-arm caliper logs. World stress map project, 1-5.

Reiter, K., Heidbach, O., Schmitt, D., Haug, K., Ziegler, M., & Moeck, I. 2014. A revised crustal stress orientation database for Canada. Tectonophysics, 636, 111-124.

Renani, H. R., & Martin, C. D. 2018. Cohesion degradation and friction mobilization in brittle failure of rocks. International Journal of Rock Mechanics and Mining Sciences, 106, 1-13.

Schwerzmann, A., Funk, M., & Blatter, H. 2006. Borehole logging with an eight-arm caliper–inclinometer probe. Journal of Glaciology, 52(178), 381-388.

Seiler, D., King, G., & Eubanks, D. 1994. Field test results of a six-arm microresistivity borehole imaging tool. Paper presented at the Society of Professional Well Log Analysts, SPWLA 35th Annual Logging Symposium. Paper W, 19-22, June.

Shafie Zadeh, N. 2016. Multiple Packer Techniques for In Situ Stress Measurement in Hard Soils-Soft Rocks. Ph.D. dissertation. University of Alberta.

Soliman, M. Y., Craig, D. P., Bartko, K. M., Rahim, Z., & Adams, D. M. 2005. Post-closure analysis to determine formation permeability, reservoir pressure, residual fracture properties. Paper presented at the SPE Middle East Oil and Gas Show and Conference. SPE-93419-MS.

Soliman, M. Y., Shahri, M., & Lamei, H. 2013. Revisiting the before closure analysis formulations in diagnostic fracturing injection test. Paper presented at the SPE Hydraulic Fracturing Technology Conference. SPE-163869-MS.

Song, J., Yuan, Y., Gu, S., Yang, X., Yue, Y., Cai, J., & Jiang, G. 2017. 2D numerical simulation of improving wellbore stability in shale using nanoparticles based drilling fluid. Energies, 10(5), 651.

Starfield, A. M., & Cundall, P. A. 1988. Towards a methodology for rock mechanics modelling. In International Journal of Rock Mechanics and Mining Sciences & Geomechanics Abstracts 25(3):99–106.

Syfan, F. E., Newman, S. C., Meyer, B. R., & Behrendt, D. M. 2007. Case history: G-Function analysis proves beneficial in Barnett shale application. Paper presented at the SPE Annual Technical Conference and Exhibition. SPE-110091-MS.

Tingay, M., Reinecker, J., & Müller, B. 2008. Borehole breakout and drilling-induced fracture analysis from image logs. World Stress Map Project, 1-8.

Vermeer, P. A., & De Borst, R. 1984. Non-associated plasticity for soils, concrete and rock. HERON, 29 (3), 1984.

Wagner, D., Müller, B., & Tingay, M. 2004. Correcting for tool decentralization of oriented six-arm caliper logs for determination of contemporary tectonic stress orientation. Petrophysics, 45(06).

Walton, G., & Diederichs, M. S. 2015. A mine shaft case study on the accurate prediction of yield and displacements in stressed ground using lab-derived material properties. Tunnelling and Underground Space Technology, 49, 98-113.

Walton, G, Diederichs, MS, Hume, C & Kalenchuk, K 2015. Borehole breakout analysis to determine the in situ stress state in hard rock. Proceedings of the Forty-ninth US Rock Mechanics/Geomechanics Symposium, American Rock Mechanics Association, Alexandria, Virginia, pp. 287–304.

Wang, D. F., Yassir, N., Enever, J., & Davies, P. 1997. Laboratory investigation of core-based stress measurement using synthetic sandstone. International Journal of Rock Mechanics and Mining Sciences, 34(3-4), 328-e1.

Whitehead, W. S., Gatens III, J. M., & Holditch, S. A. 1989. Determination of in situ stress profiles through hydraulic fracturing measurements in two distinct geologic areas. In International Journal of Rock Mechanics and Mining Sciences & Geomechanics Abstracts, 26(6), 637-645.

Yuan, S. C., & Harrison, J. (2006, January). Modeling breakout and near-well fluid flow of a borehole in an anisotropic stress field. Paper presented on the Golden Rocks 2006, The 41st US Symposium on Rock Mechanics (USRMS). ARMA-06-1157

Zajac, B. J., & Stock, J. M. 1997. Using borehole breakouts to constrain the complete stress tensor: Results from the Sijan Deep Drilling Project and offshore Santa Maria Basin, California. Journal of Geophysical Research: Solid Earth, 102(B5), 10083-10100.

Zemanek, J., Glenn, E. E., Norton, L. J., & Caldwell, R. L. 1970. Formation evaluation by inspection with the borehole televiewer. Geophysics, 35(2), 254-269.

Zhang, X., Last, N., Powrie, W., & Harkness, R. 1999. Numerical modelling of wellbore behaviour in fractured rock masses. Journal of Petroleum Science and Engineering, 23(2), 95-115.

Zheng, Z., Kemeny, J., & Cook, N. G. 1989. Analysis of borehole breakouts. Journal of Geophysical Research: Solid Earth, 94(B6), 7171-7182.

Zhou, J. W., Xu, W. Y., Li, M. W., Zhou, X. Q., & Shi, C. 2009. Application of rock strain softening model to numerical analysis of deep tunnel. Chin J Rock Mech Eng, 28(6), 1116-1127.

Zoback, M. D. 2010. Reservoir geomechanics. Cambridge University Press.

Zoback, M. D., Moos, D., Mastin, L., & Anderson, R. N. 1985. Well bore breakouts and in situ stress. Journal of Geophysical Research: Solid Earth, 90(B7), 5523-5530.

Appendix A - DFIT Interpretation at the depth of 171 m in well 8-29

G-function method:

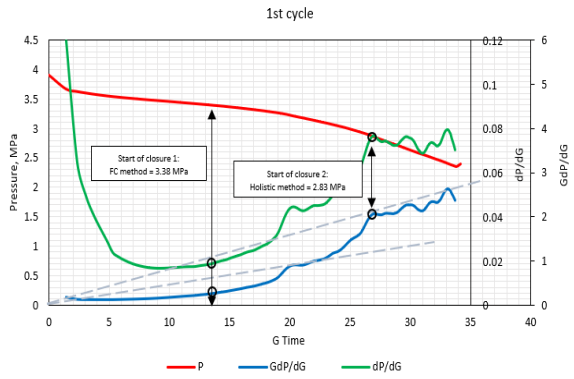

Figure A-1-a. G-function plot for the 1st DFIT cycle at 171 m depth

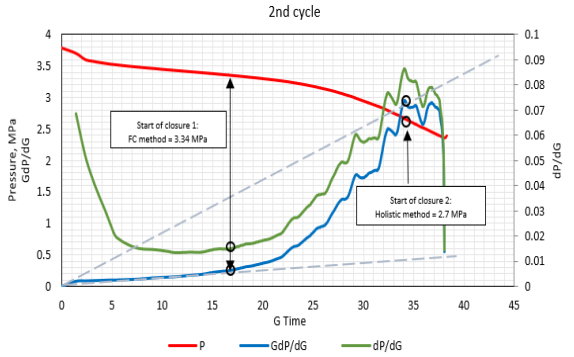

Figure A-1-b. G-function plot for the 2nd DFIT cycle at 171 m depth

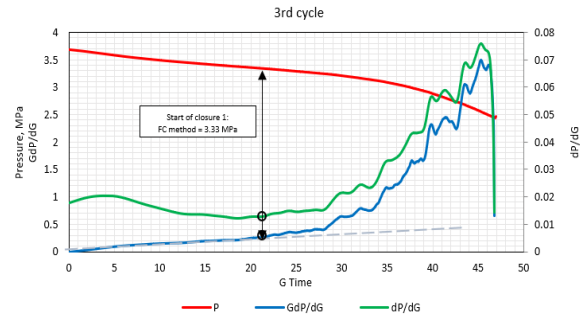

Figure A-1-c. G-function plot for the 3rd DFIT cycle at 171 m depth

Square root of time method:

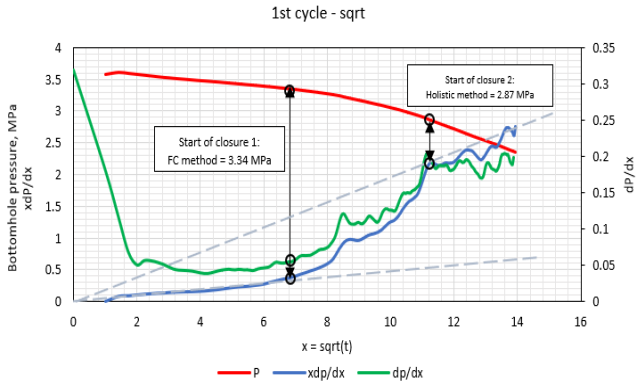

Figure A-2-a. Sqrt(t) plot for the 1st DFIT cycle at 171 m depth

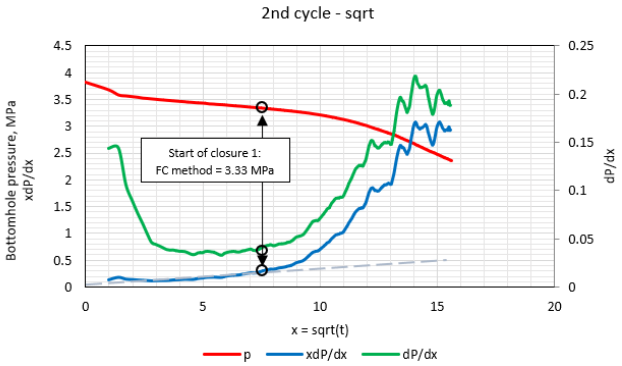

Figure A-2-a. Sqrt(t) plot for the 2nd DFIT cycle at 171 m depth

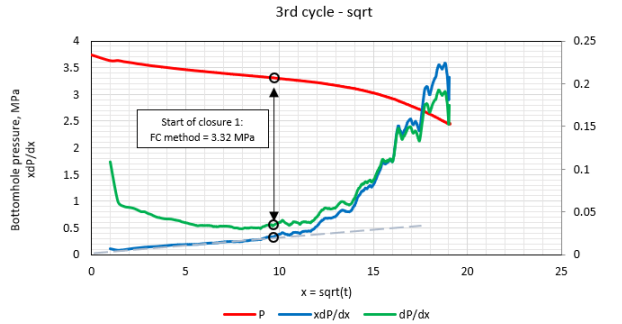

Figure A-2-a. Sqrt(t) plot for the 3rd DFIT cycle at 171 m depth

Log-log method:

Horner plot:

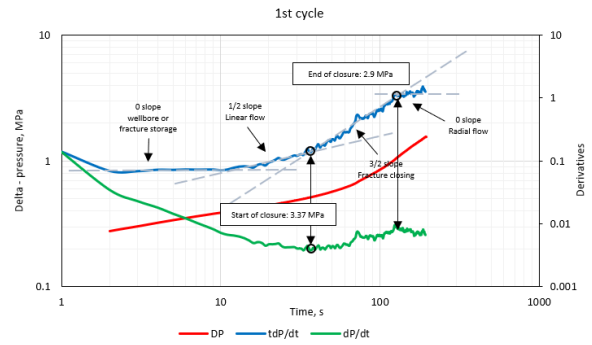

Figure A-3-a. Log-log derivative plot for the 1st DFIT cycle at 171 m depth

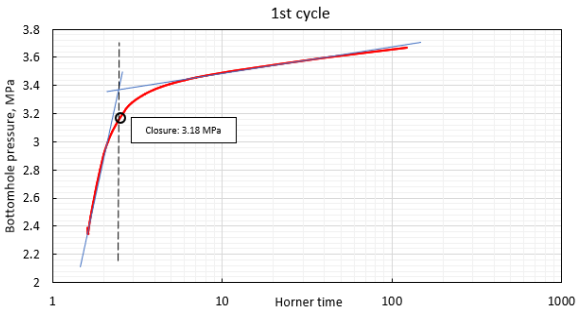

Figure A-4-a. Horner plot for the 1st DFIT cycle at 171 m depth

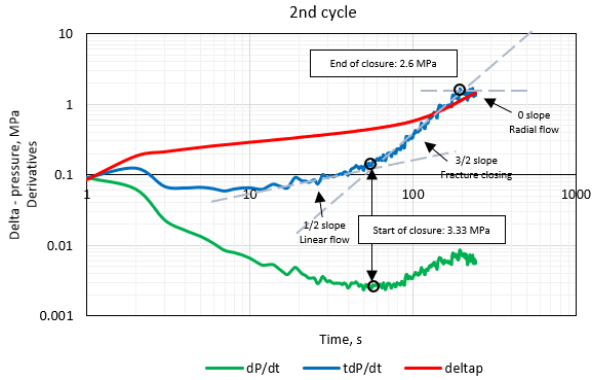

Figure A-3-b. Log-log derivative plot for the 2nd DFIT cycle at 171 m depth

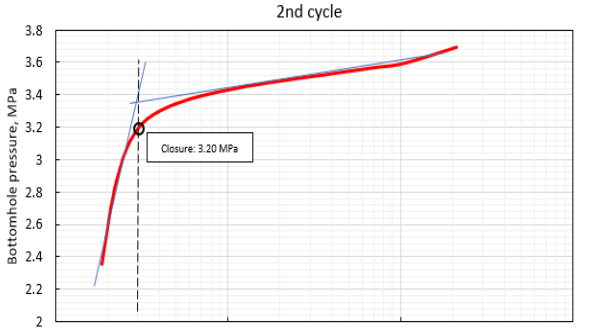

Figure A-4-b. Horner plot for the 2nd DFIT cycle at 171 m depth

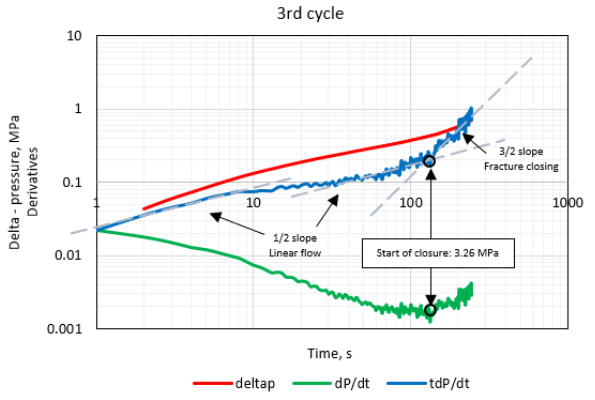

Figure A-3-c. Log-log derivative plot for the 3rd DFIT cycle at 171 m depth

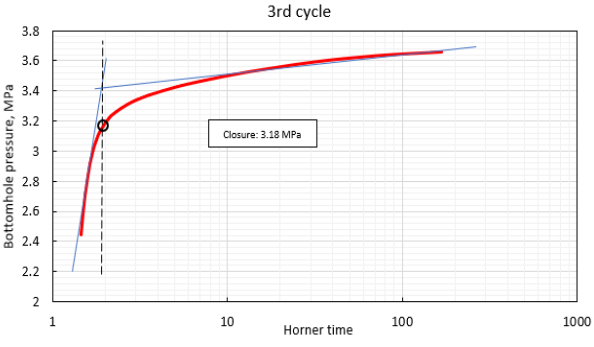

Figure A-4-c. Horner plot for the 3rd DFIT cycle at 171 m depth

Bachman's method:

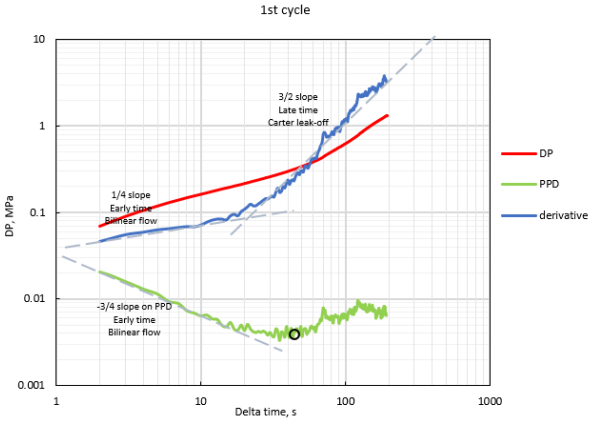

Figure A-5-1-a. Bourdet derivative plot for the 1st DFIT cycle at 171 m depth

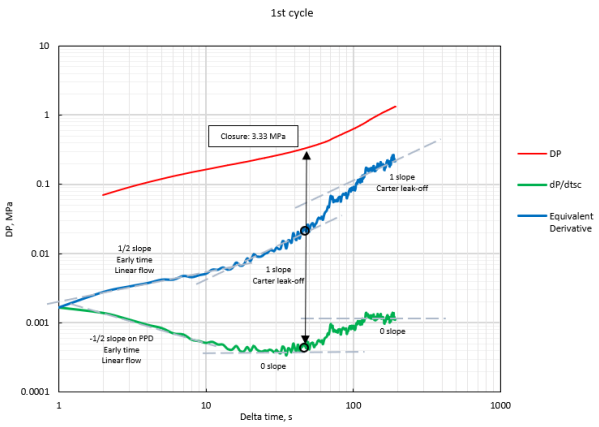

Figure A-5-1-b. Equivalent Carter leak-off plot for the 1st DFIT cycle at 171 m depth

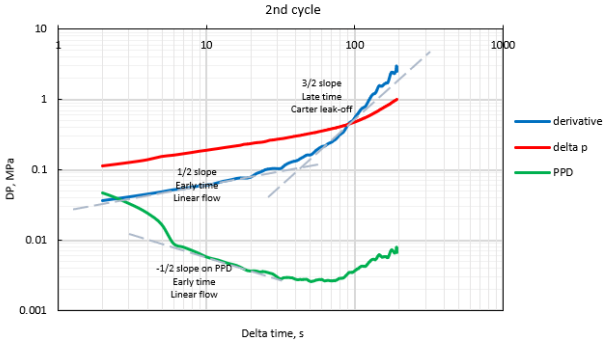

Figure A-5-1-a. Bourdet derivative plot for the 2nd DFIT cycle at 171 m depth

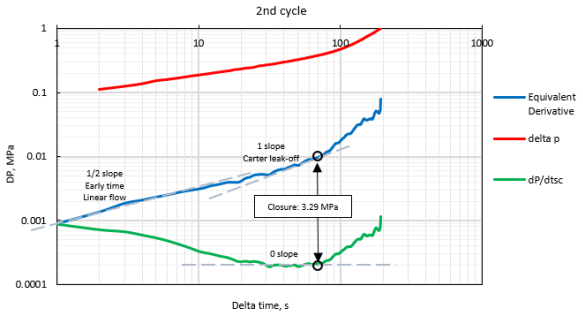

Figure A-5-2-b. Equivalent Carter leak-off plot for the 2nd DFIT cycle at 171 m depth

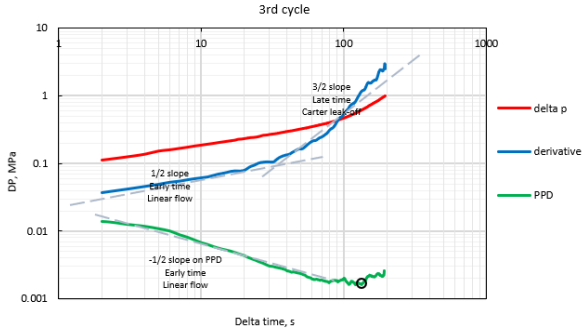

Figure A-5-3-a. Bourdet derivative plot for the 3rd DFIT cycle at 171 m depth

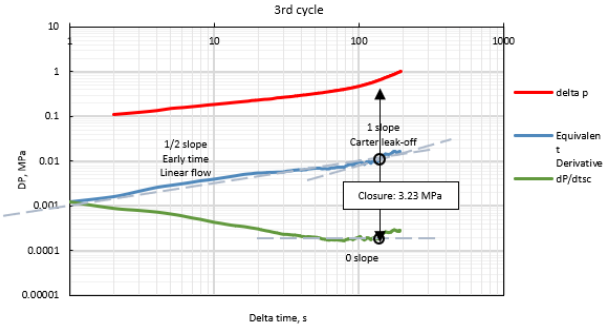

Figure A-5-3-b. Equivalent Carter leak-off plot for the 3rd DFIT cycle at 171 m depth

Pressure decay rate:

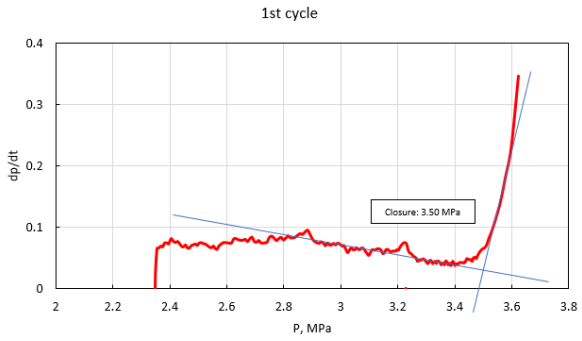

Figure A-6-a. Pressure decay rate plot for the 1st DFIT cycle at 171 m depth

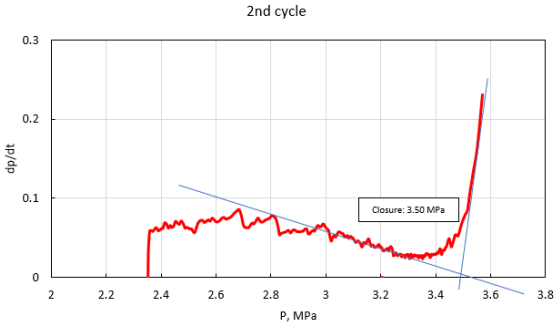

Figure A-6-b. Pressure decay rate plot for the 2nd DFIT cycle at 171 m depth

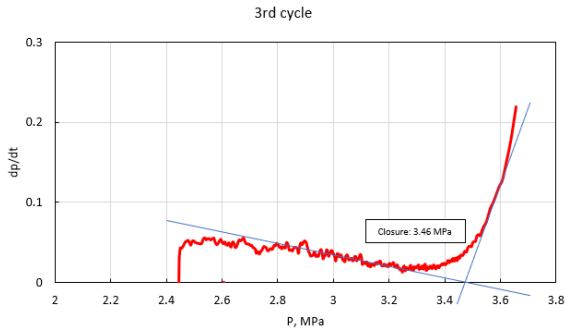

Figure A-6-c. Pressure decay rate plot for the 3rd DFIT cycle at 171 m depth

Reopening test:

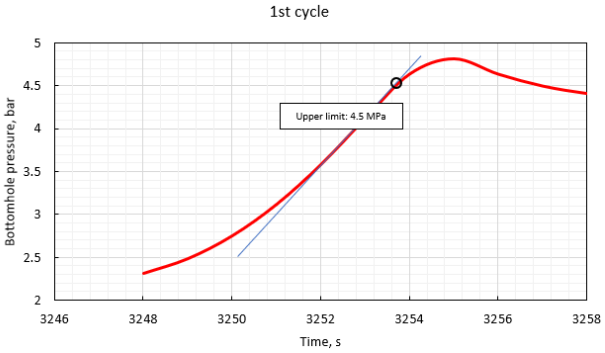

Figure A-7-a. Reopening plot for the 1st DFIT cycle at 171 m depth

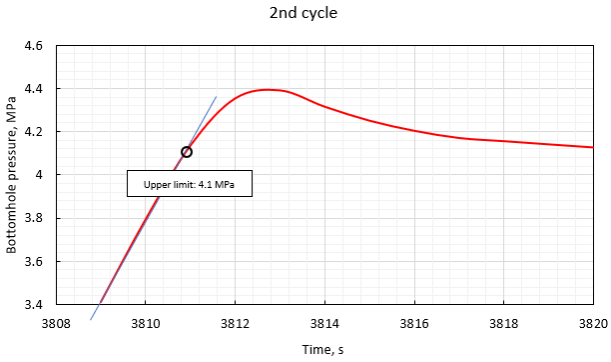

Figure A-7-b. Reopening plot for the 2nd DFIT cycle at 171 m depth

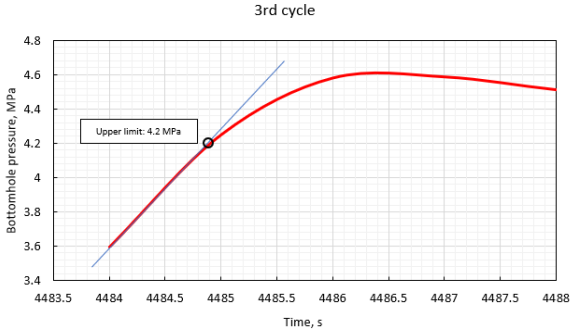

Figure A-7-c. Reopening plot for the 3rd DFIT cycle at 171 m depth

Appendix B - DFIT Interpretation at the depth of 207 m in well 8-29

G-function method:

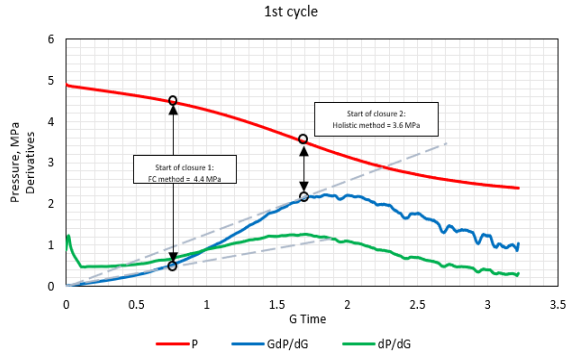

Figure A-7-a. G-function plot for the 1st DFIT cycle at 207 m depth

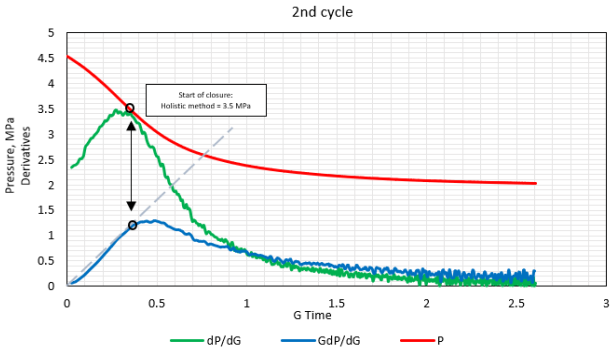

Figure A-7-b. G-function plot for the 2nd DFIT cycle at 207 m depth

Square root of time method:

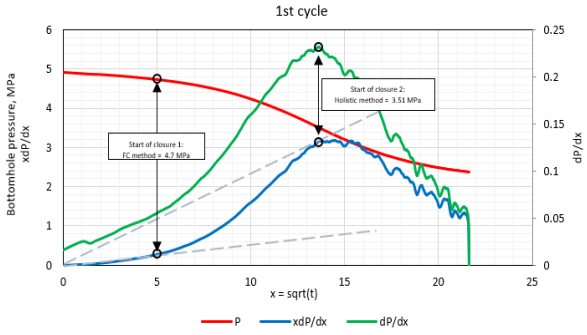

Figure A-8-a. Sqrt plot for the 1st DFIT cycle at 207 m depth

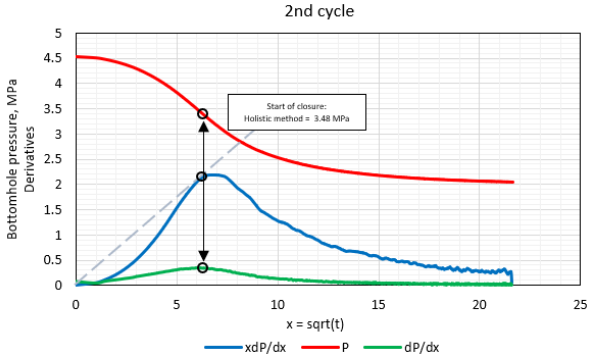

Figure A-8-b. Sqrt plot for the 2nd DFIT cycle at 207 m depth

Log-log method:

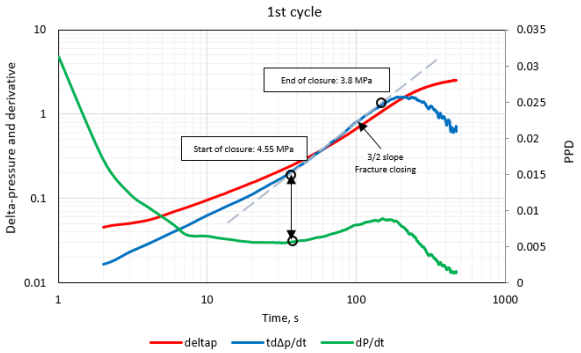

Figure A-9-a. Log-log plot for the 1st DFIT cycle at 207 m depth

Bachman's method:

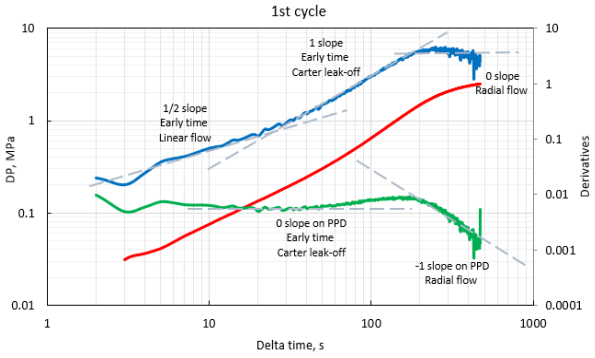

Figure A-10-1-a. Bourdet derivative plot for the 1st DFIT cycle at 207 m depth

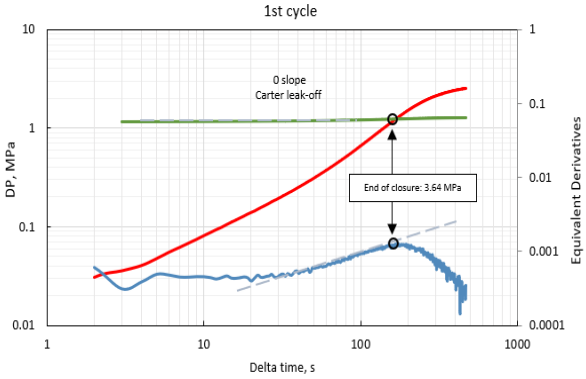

Figure A-10-1-b. Equivalent Carter leak-off plot for the 1st DFIT cycle at 207 m depth

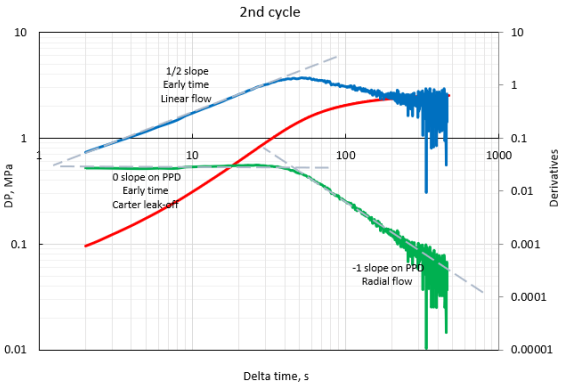

Figure A-10-2-a. Bourdet derivative plot for the 2nd DFIT cycle at 207 m depth

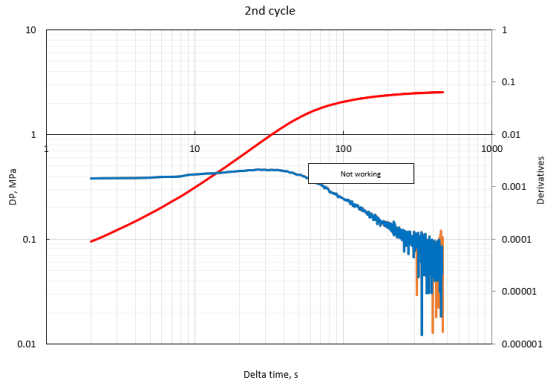

Figure A-10-2-b. Equivalent Carter leak-off plot for the 2nd DFIT cycle at 207 m depth

Horner plots:

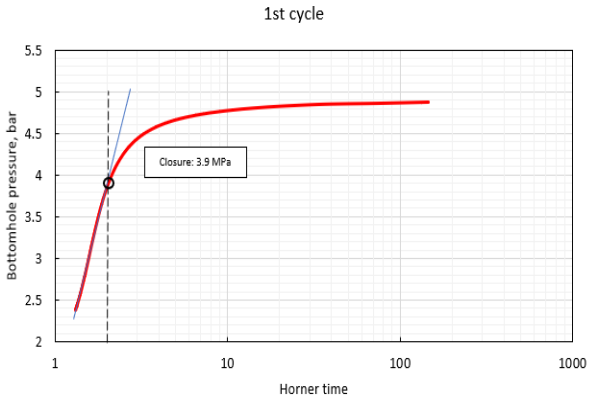

Figure A-11-a. Horner plot for the 1st DFIT cycle at 207 m depth

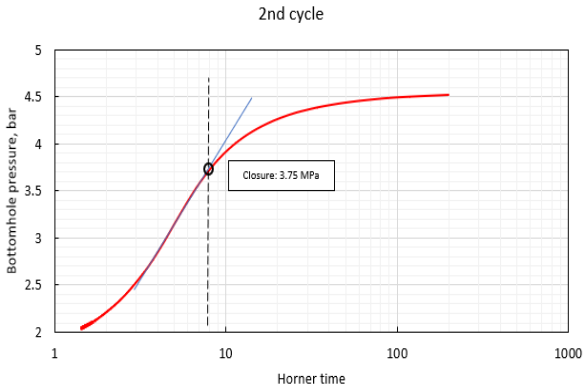

Figure A-11-b. Horner plot for the 2nd DFIT cycle at 207 m depth

Re-opening test:

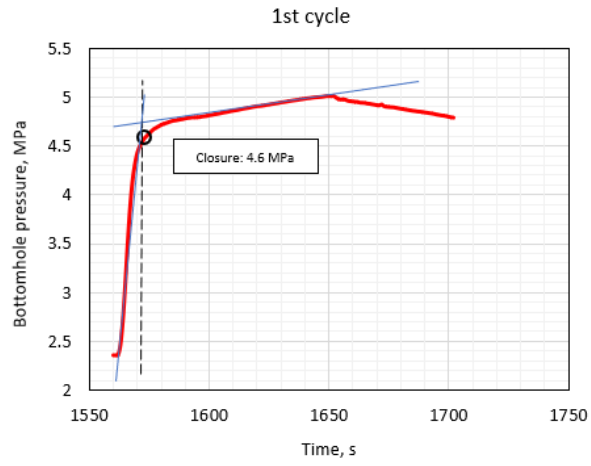

Figure A-12-a. Reopening plot for the 1st DFIT cycle at 207 m depth

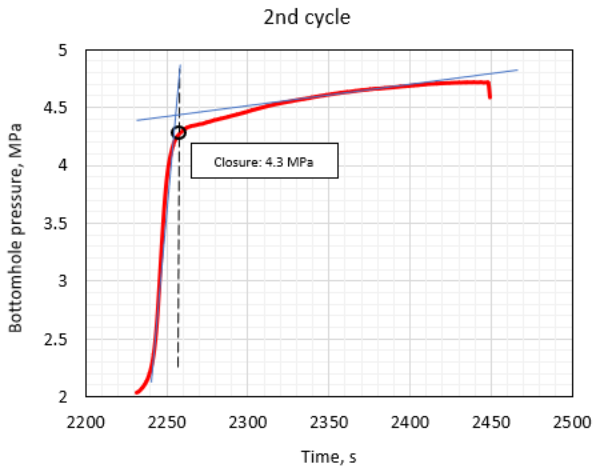

Figure A-12-b. Reopening plot for the 2nd DFIT cycle at 207 m depth

Appendix C - DFIT Interpretation at the depth of 232 m in well 8-29

G-function method:

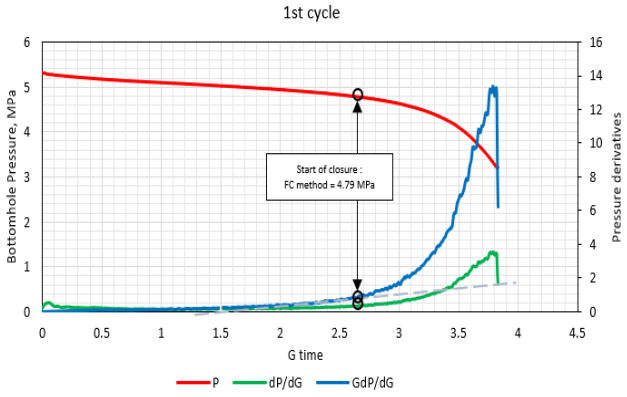

Figure A-13-a. G-function plot for the 1st DFIT cycle at 232 m depth

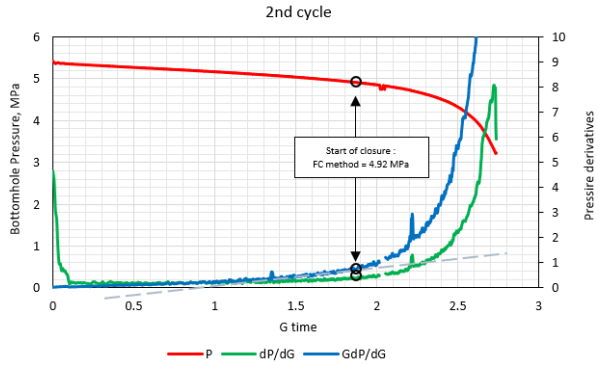

Figure A-13-b. G-function plot for the 2nd DFIT cycle at 232 m depth

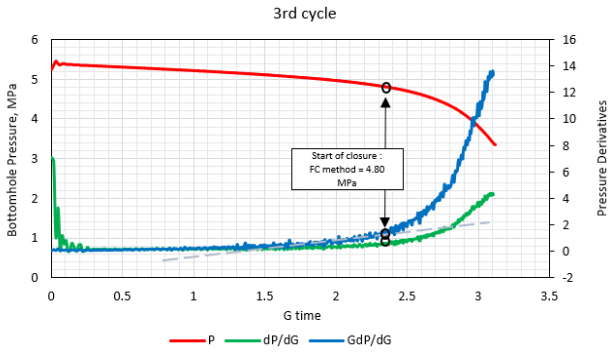

Figure A-13-c. G-function plot for the 3rd DFIT cycle at 232 m depth

Log-log method:

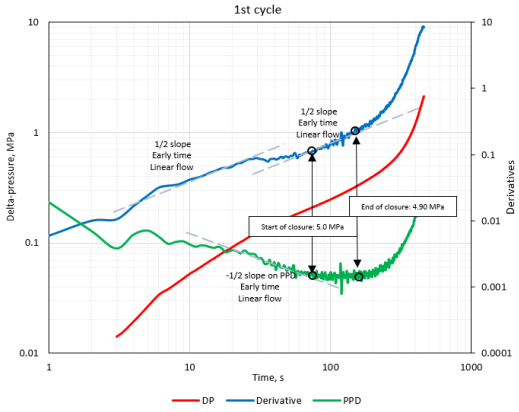

Figure A-14-a. Log-log plot for the 1st DFIT cycle at 232 m depth

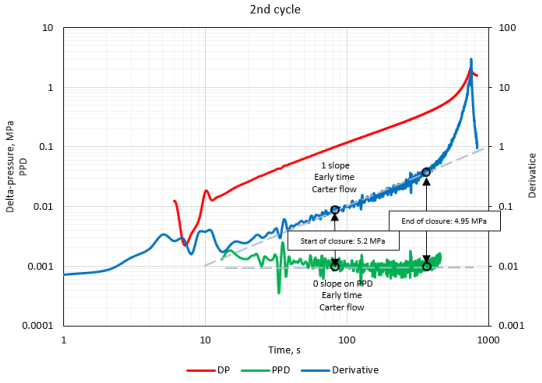

Figure A-14-a. Log-log plot for the 2nd DFIT cycle at 232 m depth

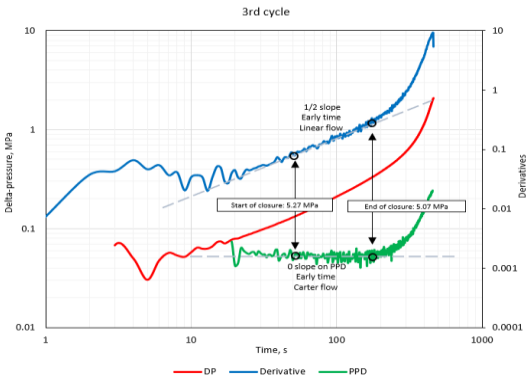

Figure A-14-a. Log-log plot for the 3rd DFIT cycle at 232 m depth

Bachman's method:

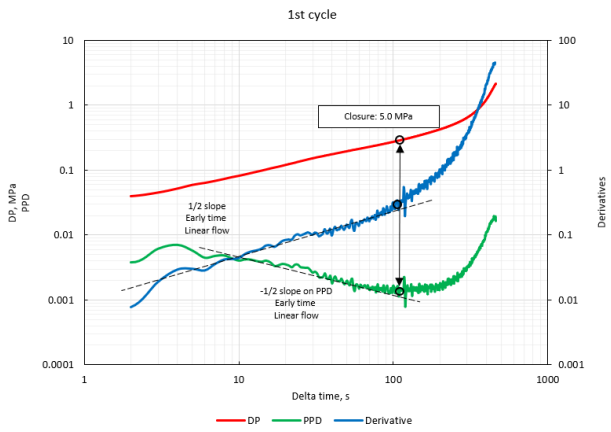

Figure A-13-a. G-function plot for the 1st DFIT cycle at 232 m depth

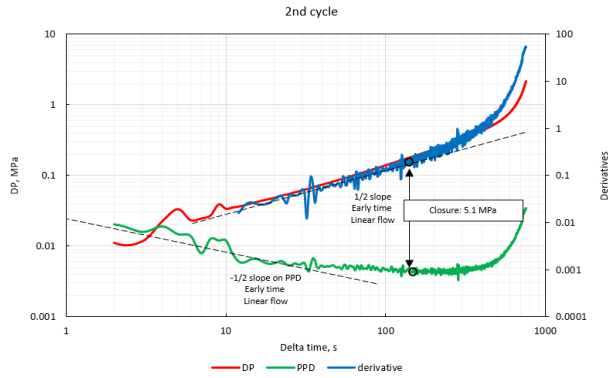

Figure A-13-b. G-function plot for the 2nd DFIT cycle at 232 m depth

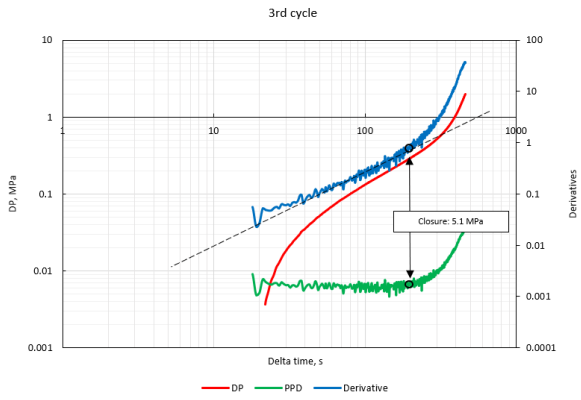

Figure A-13-c. G-function plot for the 3rd DFIT cycle at 232 m depth

Horner plot:

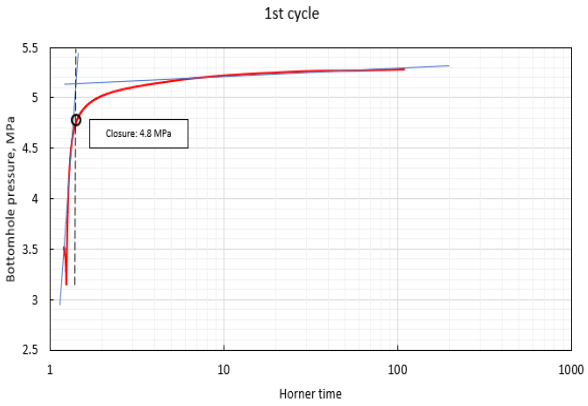

Figure A-14-a. Log-log plot for the 1st DFIT cycle at 232 m depth

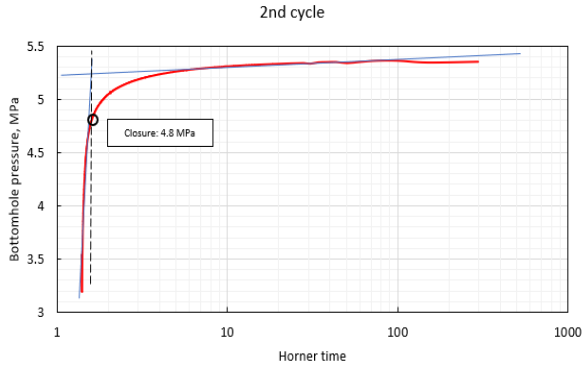

Figure A-14-a. Log-log plot for the 2nd DFIT cycle at 232 m depth

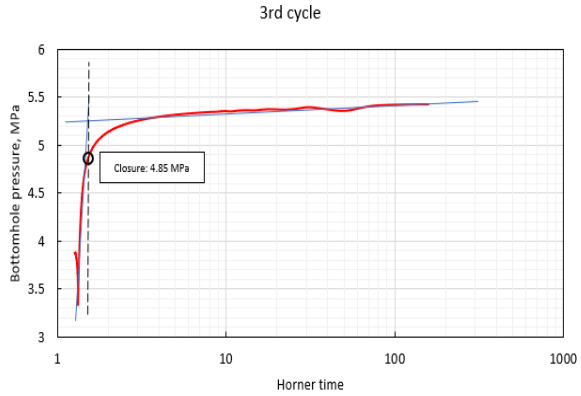

Figure A-14-a. Log-log plot for the 3rd DFIT cycle at 232 m depth

Pressure decay rate:

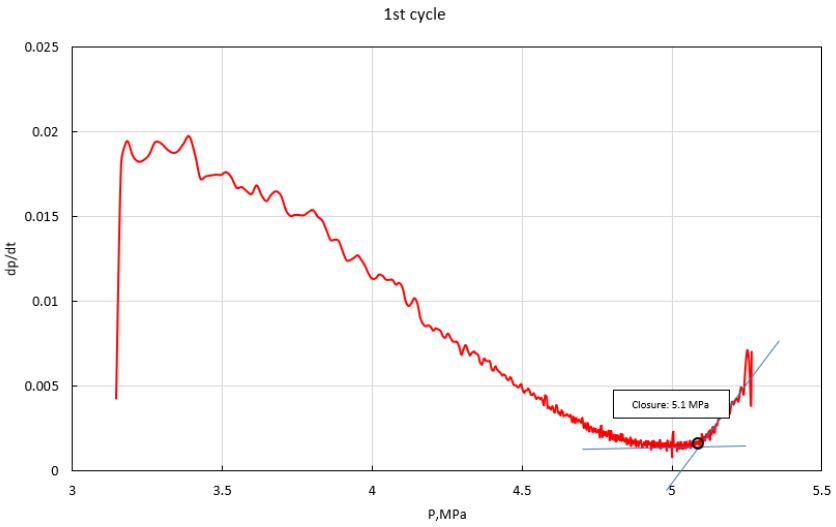

Figure A-14. Pressure decay rate plot for the 1st DFIT cycle at 232 m depth

Reopening test:

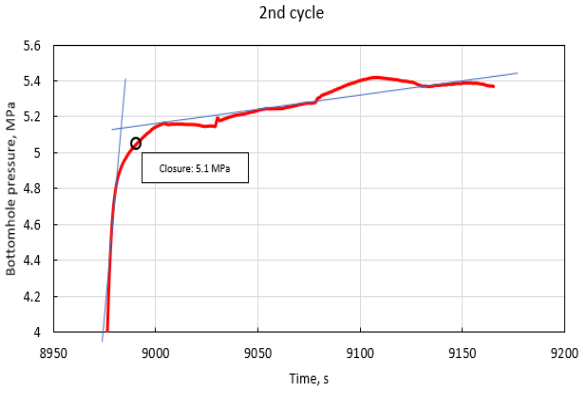

Figure A-15-a. Reopening test plot for the 2nd DFIT cycle at 232 m depth

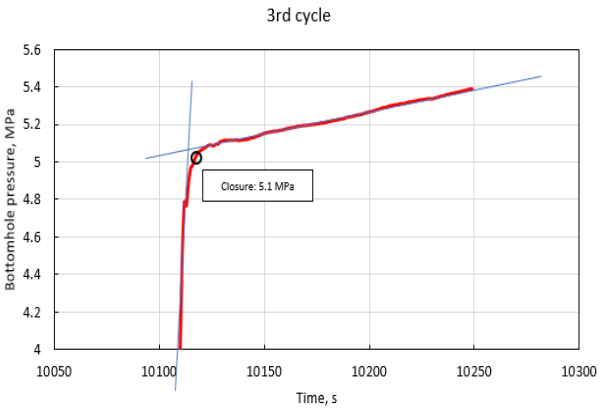

Figure A-15-b. Reopening test plot for the 3rd DFIT cycle at 232 m depth